Manganese Based Coordination Polymers: Synthesis, Characterization and Properties

A Dissertation Submitted

To

Sikkim University

In Partial Fulfilment of the Requirement for the

Degree of Master of Philosophy

By

Khanindram Baruah

Department of Chemistry

School of Physical Sciences

March, 2020

Manganese Based Coordination Polymers:

Synthesis, Characterization and Properties

A Dissertation Submitted

To

Sikkim University

In Partial Fulfilment of the Requirement for the

Degree of Master of Philosophy

Submitted By:

Khanindram Baruah
Roll No.- 18MPCH01
Reg. No.- 18/M.Phil/CMS/01
Department of Chemistry
School of Physical Sciences
Sikkim University

Under the Supervision of

Dr. Anand Pariyar
Assistant Professor
Department of Chemistry
School of Physical Sciences
Sikkim University

𝔇𝔢𝔠𝔩𝔞𝔯𝔞𝔱𝔦𝔬𝔫

It is hereby declared that the dissertation entitled "**Manganese Based Coordination Polymers: Synthesis, Characterization and Properties**" is prepared solely by me under the supervision of **Dr. Anand Pariyar**, Assistant Professor, Dept. of Chemistry, Sikkim University. Any or no part of this dissertation has not been submitted previously for any degree, diploma, associateship or fellowship.

Khanindram Baruah

Roll No: 18MPCH01
Reg. No: 18/M.Phil/CMS/01
Department of Chemistry
School of Physical Sciences
Sikkim University

We recommend that this dissertation be placed before the examiners for evaluation.

Supervisor   Head of the Department
(Dr. Anand Pariyar)   **(Dr. Somendra Nath Chakraborty)**

(Seal)   (Seal)

Dated: 06th March 2020

Certificate

This is to certify that the dissertation entitled "**Manganese Based Coordination Polymers: Synthesis, Characterization and Properties**" submitted to **Sikkim University** in partial fulfilment for the **Degree of Master of Philosophy in Chemistry** is a result of bonafide research work carried out by **Mr. Khanindram Baruah** under my supervision in the **Dept. of Chemistry, Sikkim University**. Any or no part of this dissertation has not been submitted previously for any degree, diploma, associateship, fellowship.

Dr. Anand Pariyar

(Seal)

Assistant Professor
Department of Chemistry
School of Physical Sciences
New Science Block
Sikkim University
Tadong, Gangtok
Sikkim, India - 737102

Dated: 06th March 2020

𝔓𝔩𝔞𝔤𝔦𝔞𝔯𝔦𝔰𝔪 ℭ𝔥𝔢𝔠𝔨 ℭ𝔢𝔯𝔱𝔦𝔣𝔦𝔠𝔞𝔱𝔢

This is to certify that plagiarism check has been carried out successfully for the following **M.Phil.** dissertation using **URKUND** Software and the results are within the permissible limit of the University.

Manganese Based Coordination Polymers: Synthesis, Characterization and Properties

Submitted by **Khanindram Baruah** under the supervision of **Dr. Anand Pariyar**, Assistant Professor, Dept. of Chemistry, School of Physical Sciences, Sikkim University.

Signature of the Candidate

Supervisor   **HOD**

Librarian

ACKNOWLEDGEMENT

Khanindram Baruah

Research Scholar
Department. of Chemistry
School of Physical Sciences
Sikkim University
Tadong, Gangtok
Sikkim- 737102

Table of Contents

Contents

List of Tables

List of Figures

iv

List of Abbreviations

CP	Coordination Polymer
MOF	Metal Organic Framework
1D/2D/3D	One/Two/Three Dimension
CUS	Coordinatively Unsaturated Sites
SKU	Sikkim University
CN	Coordination Network
MO	Metal Oxide
CV	Cyclic Voltammetry
MRI	Magnetic Resonance Imaging
CCD	Charge-Coupled Device
SEM	Scanning Electron Microscopy
XRD	X-ray Diffraction
P-XRD	Powder X-ray Diffraction
SC-XRD	Single Crystal X-ray Diffraction
BET	Brunauer-Emmett-Teller
DC	Direct Current
AC	Alternating Current
BJH	Barrett, Joyner and Halenda
AF	Antiferromagnetism
FC	Field Cooled
ZFC	Zero Field Cooled
RDE	Ring Disk Electrode

RRDE	Rotating Ring Disk Electrode
ORR	Oxygen Reduction Reaction
LSV	Linear Sweep Voltammetry
r.t.	Room Temperature
DOT	2,5-dihydroxyterephthalic acid
4,4'-BPY	4,4'-bipyridine
BDC	1,4-benzenedicarboxylic acid
BTC	1,3,5-benzenetricarboxylic acid
BTEC	1,2,4,6-benzenetetracarboxylic acid
TPA	Terephthalic acid
DMPDO	2,5-dimethylpyrazine-dioxide
NCS	Isothiocyanate
DCA	Dicyanamide
MeOH	Methanol
EtOH	Ethanol
DMF	Dimethyl Formamide
DEF	Diethyl Formamide
THF	Tetrahydrofuran
RPM (rpm)	Rotation Per Minute
R.H.E.	Reversible Hydrogen Electrode
GC	Glassy Carbon
LIBs	Lithium Ion Batteries
SEI	Solid Electrolyte Interphase
hcb	Honeycomb

Chapter I

Introduction and Literature Review

CHAPTER-I

INTRODUCTION AND LITERATURE REVIEW

1.1. Introduction:

1.1.1. Inorganic Materials:

In this modern era of science and technology, the priorities of inorganic materials in development of sustainable energies, pollution control, drugs and diverse physico-chemical applications caught the attention of the researchers. Inorganic materials include all the materials containing organic as well as non-organic species. These materials show high end properties depending upon the complexity of molecular architecture and routine synthetic process[1]. Inorganic materials are useful in different research field such as catalysis[2–5], gas adsorption[6–8], energy storage[9,10], magnetism[11–13], devices[14–16], agriculture[17,18], etc.

In the field of catalysis, molecular as well as electrocatalysis of various components results useful products. Currently C-H activation is one of the useful catalytic reaction especially for multimillion-dollar petrochemical industries. The abundant alkanes producing from petroleum and natural gas can be converted into alcohols which are most versatile chemical feedstock.[2–5] Another significant catalytic reaction is water splitting/water oxidation/oxygen reduction reactions where water gets converted into H_2 and O_2. The most efficient catalyst for water splitting till date is platinum. But due to high expenses in using Platinum, researchers are looking for alternative which shows similar efficiency and activity.[19,20]

In the field of optoelectronics, solar cells are the leading devices for using solar energy as an alternative for future fuel needs. But in recent days, researchers are trying to fabricate more advanced and efficient materials like nanomaterials, perovskite quantum dots, transition metal compounds, carbon materials, etc.[21,22] Perovskite quantum dots are one of the examples of inorganic materials which are now a days used in solar cells due to their interdisciplinary nature such as ion migration, defect tolerance, etc. But due to their low stability and poor life time, they are yet to be considered as efficient material

for solar cells. Many research groups are working on synthesizing perovskite QDs having high stability as well as longer lifetime.[23–25]

Inorganic materials are also used in the agriculture fields as fertilisers, pesticides and insecticides. Ammonium nitrate, potassium sulphate, copper sulphate, etc. are some of the examples of inorganic materials used in agriculture production.[17,18]

Another important application of inorganic materials is in gas adsorption. Materials like zeolites shows a very high surface area and are used in storing gases like H_2, CO_2, CH_4, etc. Zeolites are porous in nature and can store/adsorb gases under high pressure into their pore and those adsorbed gases can later be utilised by desorbing.[6–8]

The global resource for fossil fuels is on the verge of exhaustion owing to their extensive consumption.[26,27] Therefore, the world is now in search of alternate energy resources like solar energy, electricity, etc. Batteries are one of the trending fossil fuel alternatives which converts electrical energy into mechanical energy and are now a days used even on bikes, cars, etc. instead of petrol/diesel. Inorganic materials such as Lithium manganese oxide ($LiMn_2O_4$), Nickel oxyhydroxide (NiO_2H), Nickel-Cadmium (NiCd), Mercury oxide (HgO), etc. are used as electrode materials in batteries. In fuel cells and supercapacitor applications, M_xO_y (Metal oxide) (M= Transition Metals) nanoporous materials are widely used for their non-toxic nature, structural flexibility and exceptional chemical and physical stability. In electrocatalytic applications, the show bifunctional activity towards both oxygen evolution (OER) and oxygen reduction reactions (ORR) which has a potential output for replacing expensive Pt-electrodes.[28–31]. These materials are synthesized using different traditional methods from various molecular precursors. But, now a days, research is going on in CP/MOF derived M_xO_y and exploring the improved activities. Few examples are discussed in *section 1.2*.[32–34]

Apart from the advantages of using inorganic materials in different purposes, their disadvantages like poor lifetime, reusability, toxicity, stability, etc. opens up revenues for its development and creation of hybrid inorganic materials which surpasses these inhibiting factors. Researchers are giving continuous effort to make single versatile materials which addresses or minimizes the inhibiting factors.

1.1.2. Coordination Polymer:

With the growth of science and technology after World War II, the demand of new materials and development of interdisciplinary field of research became prominent. Scientists and researchers engaged themselves in developing new synthetic routes as well as design of new versatile inorganic materials. The inorganic chemistry research has grown to a sufficiently advanced level which has geared up the study of inorganic polymers. Inorganic polymers include the non-metallic and organometallic substances consisting of inorganic and organic moieties.

The chemistry of coordination polymers has advanced extensively in the past few years. In 1913, Nobel Prize recipient Swiss Chemist Alfred Werner laid the foundation of coordination polymers. In his work, he proposed the octahedral configuration of transition metal complexes and later many of the honoured materials were recognised as coordination polymers. Coordination Polymers are polymers forming infinite array of coordinating framework in 1D, 2D or 3D. The formation of the ultimate diversified frameworks depends on the building units and their compatibilities (*figure 1.1*). The interaction between the building blocks occurs through coordination interactions, hydrogen bonding, π-π stacking or Van der Waals interaction.[35] In 1964, J. C. Bailar for the first time published a review where he defined the term coordination polymer. He compared inorganic polymers with organic polymers and demarcated rules for the new species consisting of metal nodes and organic linkers.[36] According to Chen, coordinate polymers are infinite array of metal ions/clusters linked by coordinated organic ligands.[37]
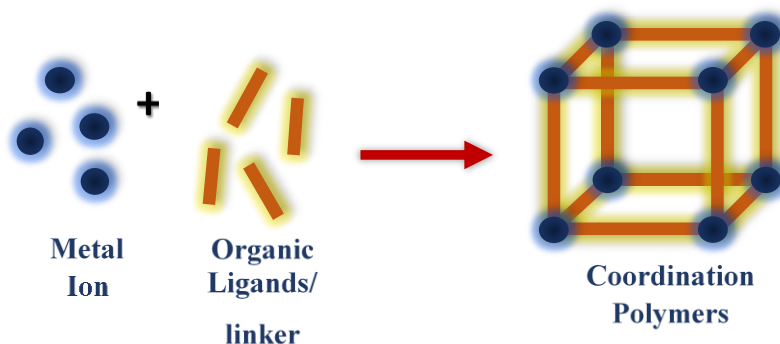
Figure 1.1: Formation of CPs

CPs are formed consisting of two main components- nodes and linkers. The number of binding sites of the linkers defines the morphology of the final building blocks. The

transition metal ions are versatile connectors/nodes used in the synthesis of coordination polymers. The variable oxidation states and coordination of metal ions give rise to geometries like tetragonal, square-pyramidal, octahedral, pentagonal-bipyramidal, and subsequent distorted shapes.[38] The main challenge of research in this field is to construct frameworks from different metal nodes and linkers and the determination and utilization of their inherent properties. With proper knowledge of possible topologies and functionalities of different multidentate ligands/linkers, one can develop or modify the synthetic efforts.[39] It is important to note that the diversity in CPs mainly depends on the organic ligands and their binding capabilities compared to the metal nodes (*figure 1.2*).[40]
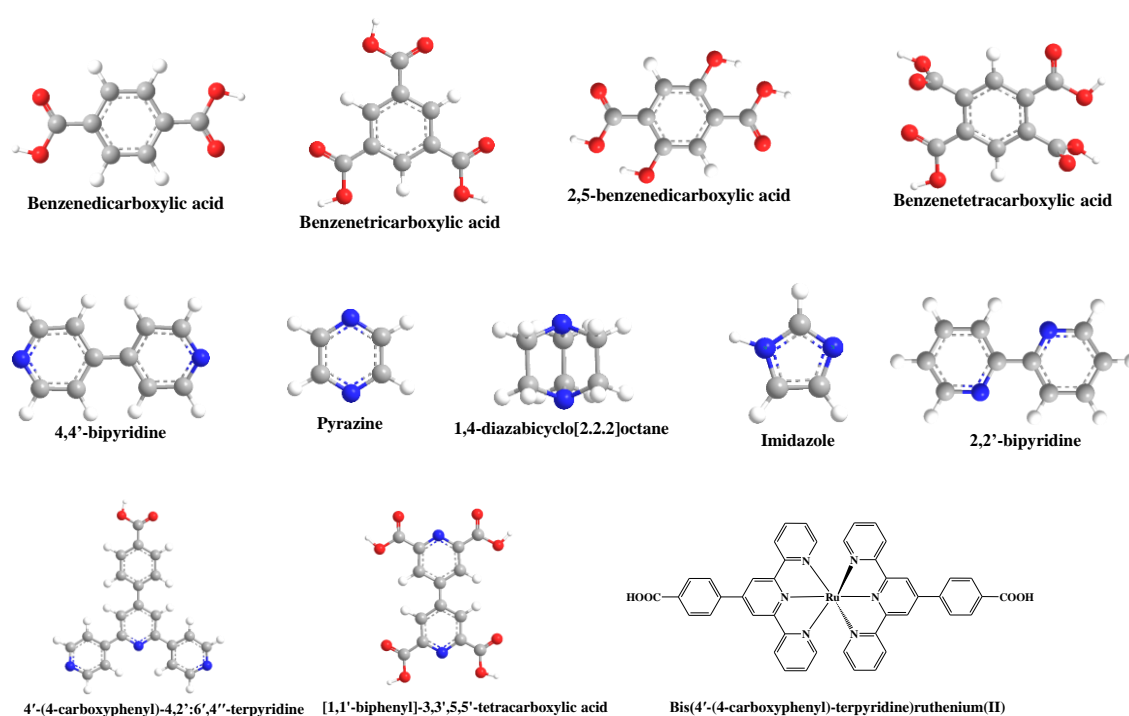
Figure 1.2: Examples of few simple multidenate ligands used for CP/MOF costruction.

The contribution of metal nodes is confined to limited accessible metal centres and coordination modes, whereas the boundless organic spacers opens the door to infinite range of frameworks. In many cases it happens to be serendipitous about the connectivity and arrangement in crystal lattice of these compounds which could be due to poor understanding of the role played by different reaction factors.[13] One peculiar arrangement of CPs are interpenetration networks present in the framework. Typically the presence of large voids, high flexibility and instability of frameworks results in merge of neighbouring network layers facilitating the formation of interpenetrating networks.[41–43]

Till date, researcher around the world has tried to explore the properties and application of CPs in the field of catalysis,[44–46] energy,[47] gas adsorption,[48,49] devices,[50] drug delivery,[51–53] storage,[54,55] magnetism,[56–58] contrasting agent,[59] electrode material,[60,61] memory,[62] sensing,[63,64] etc. However, still several areas of CP/MOF chemistry are yet to be explored concerning their potential applications.

1.1.3. Synthetic Methods:

The main objectives of establishing different synthetic techniques of CP is to obtain a standard procedure which can generate desired product without decomposing the precursors as well as to get high rate of crystal growth and nucleation. Reaction time is also one of the important factor taking in account of which all the synthetic methodologies are developed so far till date.

Slow Evaporation Method: This method involves the dissolving of the substrates in preferred solvent and leaving it to evaporate naturally. This method works without any external supply of energy but happens to be a time consuming process.[39,65]

Solvothermal/Hydrothermal Synthesis: In this method, reaction is done in a teflon lined stainless steel autoclave which can be heated up to very high temperature and generates autogenous pressure. In the vessel, solutions of metal salt and organic linkers in appropriate organic solvents are poured and kept in heating chamber depending upon the reaction condition.[66,67]

Microwave Assisted Synthesis: In microwave synthesis technique, electromagnetic waves directly interact with the reactant and solvent molecules. The interactions increase the frequent collision between molecules thereby increasing the temperature of the reaction system. MW technique allows precise control over the reaction conditions like temperature and pressure throughout the reaction. MW technique is mainly focused on crystallization, nanoscale products, purity and formation of selective polymorphs.[68]

Mechanochemical Synthesis: In this technique, mechanical cleavage of chemical bonds occurs simultaneously forming new chemical bonds facilitating the formation of CP/MOFs. One of the main advantaged of this technique is solvent free condition which is cost efficient as well as environment friendly technique. Secondly, a short time is required for completion of reaction obtaining quantitative products.[39]

Sonochemical Synthesis: In this technique, ultrasonic sonication is used for chemical transformation of precursors. When high energy ultrasound interacts with the solvent, an alternating pressure grows bubbles to a maximum size after which it collapses. During this processes, the solutes present in the solvent goes under chemical transformation *via* breakage and formation of new bonds finally forming desired products.[39]

1.1.4. Classification of CP:

There are various ways researchers classified CPs considering different factual point of view. Here, we followed the classification given by Seth *et.* al.[69] where they differentiated CPs and MOFs with a clear as shown below standpoint (*figure 1.3*). All the terminologies shown in the diagram comes under the subclass of coordination compounds out of which, three of them are of prime interest in our study- CP, CN and MOF. A very nominal structural dissimilarity were observed which divides them into different categories. IUPAC and other research groups defined that all the coordination compound formed *via* 1D/2D/3D polymeric chain interlinking metal ions by polydentate ligands are known as coordination polymers (CP)s. Whereas, coordination network (CN)s corresponds to the 2D/3D frameworks only which are crosslinked by 1D network polymers, i.e. 1D frameworks are excluded from CN category.
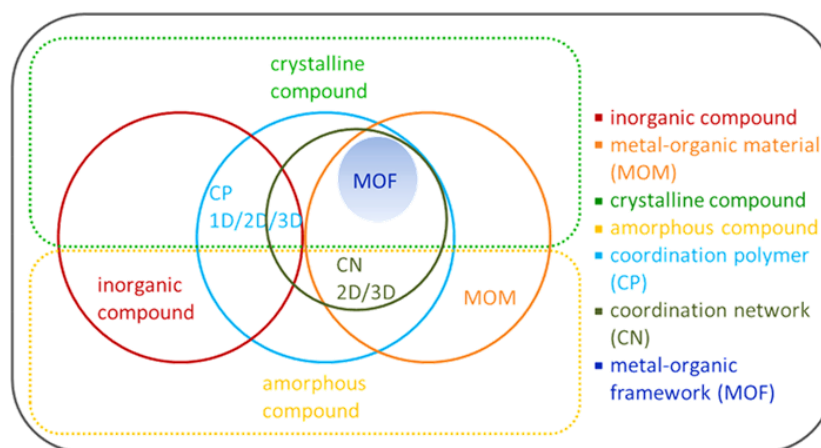
Figure 1.3: Venn diagram showing classification of CPs.[69]

Following the approaches given by Yaghi *et.* al.[70] and Biradha *et.* al.[71], metal organic frameworks (MOF)s were classified as highly robust framework with ordered 3D framework only excluding the 1D and 2D CPs. The venn diagram given above clearly distinguishes these three categories and thus made an acceptable understanding about the use of the terminologies in proper means.

1.1.5. Why Manganese?

Here in this study, we choose to work with Manganese metal salts for the synthesis of different CPs. The core reasons behind the making of this decision are:

a. It's the third most earth abundant transition element due to which it is highly cost efficient.

b. It shows variable oxidation state- +2, +3, +4, +6, +7 which will facilitate in obtaining diverse range of topologically varied frameworks.

c. It forms weakly complex and uncomplicated building units which helps researchers to predict newly discovered molecular structures.

d. It is nontoxic in nature and also essential for human, animal as well as for plants life.

e. It holds rich redox chemistry such as $Mn^{+2} \rightarrow Mn^{0}$, $Mn^{+3} \rightarrow Mn^{+4}$, $Mn^{+2} \rightarrow Mn^{0}$, $Mn^{+2} \rightarrow Mn^{0}$.

1.2.   Literature Review

In past few years, the roles of co-ordination polymers have been vastly studied. Considering the structural configurations and inherent characteristics of different Mn-based CPs which are constructed with the help of polydentate organic linkers, researcher around the world tried to utilize and explore their aspects in different field of chemistry. A brief literature review was made as per our research goals and scopes.

In **2005**,[72] Sun *et.* al. reported four different Mn-based coordination polymers [{Mn(NCS)$_2$-(2,5-DMPDO)$_{1.5}$(H$_2$O)$_2$}.0.5(2,5-DMPDO).H$_2$O]$_n$ (**1**), [Mn(N$_3$)$_2$-(2,5-DMPDO)(H$_2$O)$_2$]$_n$ (**2**), [Mn(DCA)$_2$(2,5-DMPDO)]$_n$ (**3**) and [Mn(DCA)$_2$(2,3-DMPDO).H$_2$O]$_n$ (**4**). using 2,5-dimethylpyrazine-dioxide (2,5-DMPDO) and 2,3-dimethylpyrazine-dioxide (2,3-DMPDO) as linkers. The results obtained by using different combination of anions such as NH$_4$NCS, NaN$_3$ and sodium dicyanamide [Na(DCA)] showed the major influence of anionic ligands compared to neutral ligands. All of the four frameworks retains antiferromagnetic interactions within neighbouring Mn metal centres with spin flop transitions below 7 K. Rosi *et.* al.[73] described the structure of Mn-MOF-73 [Mn$_3$(BDC)$_3$(DEF)$_2$]$_n$ constructed using 1,4-

benzenedicarboxylic acid (BDC) which possesses a *pcu* arrangement with coordinated diethylformamide (DEF) molecules with each Mn-centres. An apparent surface area of 181 m^2g^{-1} was obtained which was measure using gravimetric analysis method. Wang *et. al.*[74] reported a new Mn-based CP $[Mn(N_3)_2(BTR)_2]_n$ using 4,4′-bi-1,2,4-triazole (BTR) as linker. They investigated the coexistence of three different magnetic phenomena spin-canting, the metamagnetism, and the spin-flop phenomena in the obtained molecular system. DC magnetic susceptibility measurements showed an abrupt increase in χ_M with large negative Weiss constant (θ = -60.8 K) which was referred as strong intralayer AF coupling (where *J*= -3.26 cm^{-1} and -3.10 cm^{-1}).

In **2006**, Tang *et. al.*[75] reported a novel Mn-based 2D CP using a tetradentate ligand rac-(*R,S*)-2,2′-bipyridine-3,3′-dicarboxylic acid 1,1′-dioxide [(*R,S*)-H$_2$BDCD]. The structure contains two Mn-cores forming an edge-shared octahedra which facilitates the magnetic interactions. Variable temperature magnetic measurements first displayed a slow increase in χ_mT value till 50 K and then a sudden rise in χ_mT denotes the dominant ferromagnetic interaction between Mn-atoms. Moon *et. al.*[76] reported a 3D porous MOF $[Mn(NDC)(DEF)]_n$ (**1**) incorporating 2,6-naphthalenedicarboxylic acid (H$_2$NDC) ligand. Compound **1** was first prepared by solvothermal method which contains a coordinated DEF molecule. Later, the DEF molecule was desolvated and the resulting PXRD pattern of the obtained product $[Mn(NDC)(DEF)]_n$ (**2**) indicates the change in structural framework of **1**. Since the removal of DEF creates CUS on Mn^{II} atoms, it adsorbs water vapour as well as N_2, H_2, CO_2, and CH_4 gases with permanent porosity.

In **2007**, Yuan *et. al.*[77] reported two azide bridged Mn(III) CPs. In their work, they studied the effect of side group of Schiff base ligands on structure and magnetic behaviour of the complexes. The structure contains 1D chains combining [Mn^{III}(Ligand)] subunits excluding the side group of Schiff base ligand. These azide-bridged chains gets extended into 3D framework *via* the formation of H-bonding. In magnetic analysis, they found the presence of uncoupled spin-only Mn(III) ion with dominant AF character for **1** which was supported by AC magnetic susceptibilities and in-phase/out-of-phase measurements. Similarly, compound **2** also shows overall strong AF character along with weak ferromagnetic interactions. An important observation in this work is the effect of side group, i.e. in absence of side groups in salen, no significant phase change at low

temperature was observed whereas introducing side groups (Cl/Br/F/OCH$_3$) changes the structural configuration as well as the magnetic behaviour.

In **2008**, Taylor *et.* al.[78] prepared nanoparticles of two Mn-MOFs (NMOF)- Mn-BDC and Mn-BTC to study their activity as MRI contrasting agent. Mn-BTC was also prepared by coating with silica shell which stabilizes then during functionalization with Rhodamine-B. During study, the observed stronger MRI signals for human colon cancer (HT-29) cells incubated with rhodamine B-functionalized Mn-BTC nanoparticles. The obtained results revealed the targeted delivery on Mn^{2+} ions by surface functionalized nanoparticles of Mn-MOFs to cancer cells which facilitates in obtaining brighter MR images (*figure 1.4*).
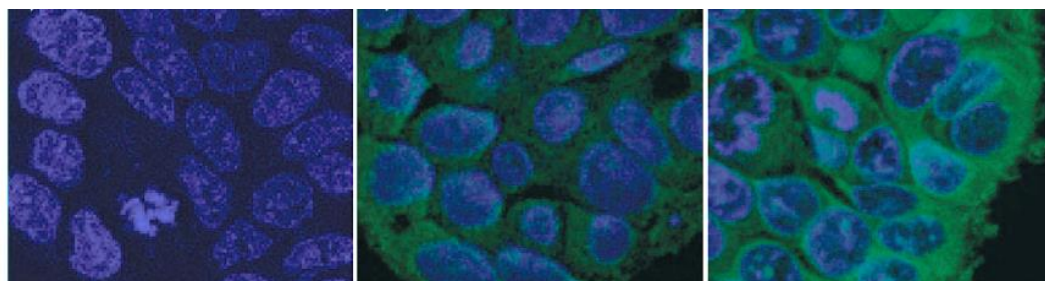
Figure 1.4: MR images of HT-29 cells incubated without Mn-BTC (left), thin silica shell coated Mn-BTC (middle) & cell-targeting peptide coated Mn-BTC (right).[78]

Horike *et.* al.[79] investigated the catalytic activity of Mn$_3$[(Mn$_4$Cl)$_3$(BTT)$_8$(CH$_3$OH)$_{10}$]$_2$ MOF which is constructed using 1,3,5-benzenetristetrazol-5-yl (H$_3$BTT) ligand. Firstly, they investigated they catalytic cyanosilylation of aromatic aldehydes and ketones (*figure 1.5*).
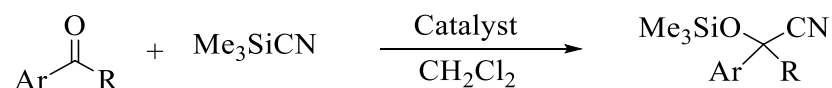
Figure 1.5: Scheme for the cyanosilylation aromatic aldehydes/ketone.[79]

The reaction for catalytic transformation of different carbonyl substrates showed a highest of 98 % conversion rate in 9 h which was greater than the previous reports. While a lesser conversion rate was observed in absence of the catalyst giving the evidence of heterogeneous catalysis supported by Mn-MOF. To establish the fact that these catalytic conversion of aromatic aldehydes requires the presence of Lewis acid sites, they implemented similar reaction conditions for Mukaiyama-aldol reaction of benzaldehyde

with methyltrimethylsilyldimethylketene acetal. The reaction resulted in a 63 % yield at r.t. after 99 h which was comparable to the previous report. In addition to this, the same reaction in presence DMF solvent resulted 51% yield indicating active Mn^{2+} sites even in presence of highly coordinating DMF molecules.

In **2009**, MOFs with ferroic or multiferroic properties are rarely reported till date. Combination of magnetic ordering of MOFs and guest molecules possibly result in ferroic and multiferroic properties. Jain *et.* al. studied the multiferroic behaviour associated with a Mn-based MOF $[\{(CH_3)_2NH_2\}Mn(HCOO)_3]_n$. PXRD patterns indicates the occurrence of phase change was expected to be due to dielectric anomaly. On measuring the dielectric constant, a clear hysteresis loop was observed which corresponds to phase change from paraelectric to antiferroelectric. Moreover, specific heat measurements made it clear that a transitions leading to electrical and magnetic ordering has occurred. An EPR spectra, however, clarifies the structural change along with magnetic transition. Zhang *et.* al.[80] reported a novel Mn-MOF $[Mn(bdpbp)_2(NO_3)_2]_n$ (where bdpbp= 4,4'-bis(dimethoxyphosphorylmethyl)biphenyl) and they observed an interpenetrating network forming overall 3D supramolecular structure. Mn(II) ions forms 2D grid linked *via* is four 'bdpbp' linkers and two such grids forms a 3d framework connecting *via* weak inter-layer C-H⋯O hydrogen bonding. The compound also show peaks in fluorescent spectra near 320 and 624 nm and an excitation peak at 288 nm which was recognised as ligand-to-1igand and ligand-to-metal charge transfer transitions.

In **2010**, Ladrak *et.* al.[81] prepared four Mn-based MOFs $[Mn_3(atpa)_2(Hatpa)_2]$ (**1**), $[Mn_3-(atpa)_3(dmf)_4]$ (**2**), $[Mn_3(tpa)_3(def)_2]$ (**3**) and $[Mn_2(tpa)_2(dmf)_2]$ (**4**). A small change in solvent and functionalized ligand ensued the formation of new frameworks. They examined the catalytic activity of all the four MOFs in cyanosilylation of acetaldehyde. Firstly, a reaction in 1:2 ratio of acetaldehyde and trimethylsilyl cyanide was performed using **1** as catalyst. The reaction yielded in 64 % of O-silylated lactonitrile in 24 h. However, the yield increased to 80 % in 3 h when the catalyst was recycled which was attributed as the effect removal of DEF molecules. Similarly, yield of 80-82 % was achieved using catalyst **2-3**. Li *et.* al.[82] reported five Mn-based MOFs with mono-, di-, tri-, tetra-nuclear atomic nodes using common ligand 4,4'-dicarboxybiphenyl sulfone (H_2sdba) and four different nitrogen based ligand. Among all the five CPs, one exhibits non-interpenetrated framework while four of them displays interpenetrated network

structures. Magnetic measurements unveiled similar antiferromagnetic characteristics in all the four interpenetrated CPs. Yang *et.* al.[83] reported 1D coordination polymer [MnTHPP·H_2O·(DMF)$_2$]$_n$ (where THPP= 5,10,15,20-tetra(4-hydroxyphenyl) porphyrin) exhibiting right-handed helical assembly analogous to helical structures present in various natural products (*figure 1.6*). They proposed a scheme where expulsion of Cl⁻ in the form of ammoniumchloride (NH_4Cl) finally generating the right-handed helices. To assess the opticity of this helical CP, circular dichroism (CD) spectra were recorded. A strong CD spectrum indicates the ability the compound to change the achiral starting blocks into chiral assembly of metalloporphyrins.
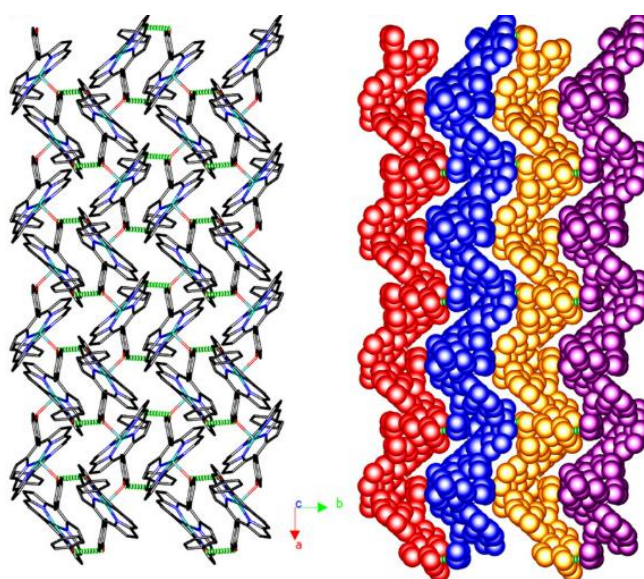
Figure 1.6: (a) H-bonding forms right handed helical structure & (b) space-filling architecture of the helical structure.[83]

In **2011**, Xie *et.* .al.[84] described a novel photochemical transition a newly reported Mn-CP converting into another cyclised framework. They first constructed a 2D framework [{$Mn_2L_2(H_2O)_2$}·$3H_2O$]$_n$ (**1**) using E-5-(2-(pyridin-4-yl)vinyl)isophthalic acid ligand. This 2D framework compound on exposure to Hg light irradiation for 24 h resulted in [2+2] cyclo addition of the ligand transforming the over 2D framework to a 3D framework [{$Mn_2L'_2(H_2O)_2$}·$3H_2O$]$_n$ (**2**). The newly formed product contains 5,5'-(3,4-diphenylcyclobutane-1,2-diyl)diisophthalic acid ligand. They also performed catalytic oxidation of phenyl methanol using both the materials as catalysts (*figure 1.7*). The results obtained showed a 64 % and 90 % yield of benzaldehyde after 18 h under ambient light in presence of **1** and **2** respectively. When the same reaction was performed in

absence of light, the yield of only 28 % benzaldehyde was achieved suggesting the ambient light supporting catalytic conversion of phenyl methanol.
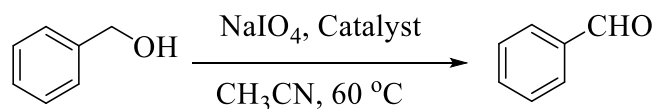
Figure 1.7: Scheme for oxidation of phenyl methanol.[84]

In **2012**, Liu *et. al.*[85] has synthesized Mn-based layered coordination polymer which showed a good magnetic and electrical properties. In their work, they have synthesized Manganese complexes using 2,3,5,6-tetrafluroterephthalic acid and 4,4'-bipyridine as linkers. The results obtained from CV analysis showed a discharge capacity of 1807 mA h g^{-1} on first discharge, but in the second discharge it decreased to 552 mA h g^{-1} which is a decent cycling stability of the electrode. After 50 cycles, discharge capacity decreses to 390 mAh/g. They have also performed magnetic measurements which revealed the weak antiferromagnetic interactions between the Mn(II) centres.

In **2014**, Zhao *et. al.*[86] prepared $[\{Mn_3(HCOO)_6\}DMF]_n$ MOF material and studied their adsorption properties. The compound possesses a BET surface area of 78.1 $m^2 g^{-1}$ with a N_2 uptake of 28.3 $cm^3 g^{-1}$ whereas 57 $cm^3 g^{-1}$ & 43 $cm^3 g^{-1}$ of CO_2 uptake at at 273 K & 298 K were observed. To check the CO_2/N_2 gas separation, adsorption selectivity were estimated using Henry's constants where an adsorption selectivity of 36.6 for CO_2 over N_2 at 273 K and 25.3 at 298 K were observed suggesting a noble material for CO_2 capture.

In **2015**, Lv *et. al.*[87] constructed two novel Mn-MOF $[Mn_3(BOABA)_2(phen)_2]_n$ (**1**) and $[\{Mn_2(BOABA)(OH)\}\cdot(H_2O)_2]_n$ (**2**) incorporating a newly 2,4-bis-oxyacetate-benzoic acid (H_3BOABA) ligand. To examine the photoluminescent property, emission spectra were recorded for both the materials. For **1**, emission peaks maximum at 450, 518 (λ_{ex}=357 nm) were observed whereas emission peaks maximum at 470 nm (λ_{ex}=326 nm) was observed for **2**. The red shift occurred compared to the ligand [420 nm (λex=325 nm)] was attributed to be the ligand-to-metal charge transfer effect. They also studied the interaction of **1** & **2** with calf thymus DNA (ct-DNA) using EB fluorescent probe (*figure 1*.8) and the final results shed light into the capability of compounds interacting with DNA which were significant than that of the ligand itself. Zhang *et. al.*[88] incorporated

carbon nanotubes (CNT) into Mn-MOF and observed a significant improvement in conductivity from 43.2 F g^{-1} for pure Mn-MOF to 203.1 F g^{-1} for CNTs@Mn-MOF
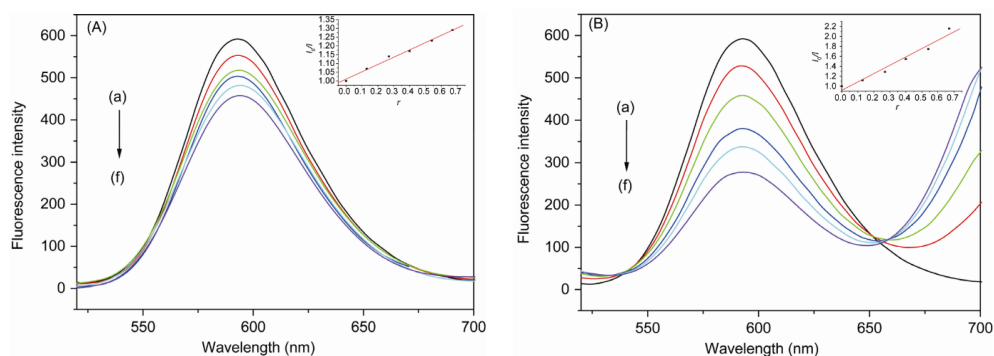
Figure 1.8: Emission spectra of EB-DNA system (A) in the absence and presence of H$_3$BOABA and (B) in presence of **1**.[87]

which are higher than previous reports. They suggested this high gap between the results causing due to poor conductivity shown by pristine MOF materials. Additionally, the CNT@MN-MOF materials showed an energy density of 6.9 W h kg^{-1} at a power density of 122.6 W kg^{-1} and an outstanding recyclability monitored up to 3000 cycles.

In **2016**, Li *et.* al.[89] investigated the electrochemical activity of two MOFs Mn-BTC (**1**) and Mn$_{1.7}$Co$_{0.3}$-BTC (**2**). Charge–discharge profiles of **2** at a current density of 100 mA g^{-1} showed a maximum capacity of 1642 mA h g^{-1} in first cycle which decreases to 901 mA h g^{-1} till 150th cycle whereas a very less capacity of 251.9 mA h g^{-1} after 100 cycles was observed in case of **1**. The capacity obtained for compound **2** is significantly higher than mostly reported MOF anode. Dey *et.* al.[90] synthesized a Mn-CP [{Mn(L)(pyz)}ClO$_4$.2(H$_2$O)]$_n$ incorporating a Schiff base ligand and pyrazine. In this work, they monitored the antibacterial activities of the Mn (II) CP in two pathogenic gram negative bacteria (Shigella flexneri and Proteus mirabilis) and two gram positive pathogenic bacteria (Bacillus cereus and Bacillus subtilis). From the results obtained, they observed decent antibacterial activity by the Mn-CP in three of the bacterial stains except Bacillus subtilis. Liposolubility greatly effects the control of antimicrobial activity and due to the presence of highly delocalized π-electrons throughout the CP framework, lipophilicity increases. This enhanced lipophilicity assists the restriction of further growth of the microorganisms. Hu *et.* al.[91] studied the electrochemical properties of Mn-BDC MOF. They tested the performance of Mn-1,4-BDC and activated Mn-BDC@200 (heated at 200 °C) coated electrode for LIBs. Two cathodic peaks at 0.67 V and 0.19 V

were observed which corresponds to irreversible reaction of SEI layer film and intercalation of Li^+ into organic moiety. An initial discharge and charge capacities of 1746 and 706.4 mA h g^{-1} were found for Mn-BDC@200 which is a bit higher than that found for Mn-BDC- 1548 and 575.2 mA h g^{-1}. Also, the reversible capacity of Mn-BDC@200 was found to be higher than that for Mn-BDC after 100th cycles- 974 mA h g^{-1} and 752 mA h g^{-1} respectively. Das *et.* al.[92] synthesized a 1D Mn-based CP [{$C_6H_4(O)CHN(CH_2)_2NCH(O)C_6H_4$}Mn(N_3)]_n suing a Schiff base ligand. Magnetic measurements indicated the presence of weak antiferromagnetic interaction between Mn-centres whereas CV data gave the evidence of reversible Mn^{3+}/Mn^{2+} redox system. Apart from these, the material showed interesting anti-mycobacterial activity over *M. tuberculosis* H37Rv ATCC 27294 and *M. tuberculosis* H37Ra ATCC 25177 strains. The synthesized CP showed satisfactory anti-mycobacterial activity with MICs of 51.38 µmol/L and MBC values in the range of 51.38-398.71 µmol/L. The obtained results for the Mn-CP were compared with two commercially available drugs- streptomisin and isoniazid which were found adequate. Paul *et.* al.[93] synthesized seven different Mn-based CPs out of which two of them exhibits photoluminescene (*figure 1.9 (a)*) and thus have potential application as contrasting agents and drug carrier. When UV/Vis was performed for [{$Mn(L)(H_2O)_2$}·2Nap]_n (**1**) and [{$Mn(L)(Flr)_2(H_2O)_2$}]_n (where L= 1,2- bis(4-pyridyl)ethylene), (**3**) an increase in optical density was observed with increasing concentration of the CPs. Also, after incorporating imaging agent and the drug molecule into the CPs, an intense green emission spectra was observed when excited in blue light of wavelength ~480 nm (*figure 1.9 (b)-(g)*). The quantum yield was also determined for both the materials to be 2.5 and 4.9%, respectively. The cytotoxicity results also ensured the biocompatibility of the materials. RAW 264.7 macrophage cells were incubated in an optimized interval of 15 min when maximum fluorescence intensity was observed. In addition to this, the ability of drug delivery using the corresponding CPs were tested by the anti-inflammatory response of both the CPs which were found similar to the NSAID.

In **2017**, Wu *et.* al.[94] performed catalytic studies of cycloaddition of CO_2 with epichlorohydrin (ECH) using Mn-BTC MOF. They performed the reactions varying the factors effecting reaction productivity to establish an optimal condition for obtaining maximum yield. They concluded the highest yield to be obtained was 94.14 % with a temperature of 105 °C for 9 h. The maximum amount of catalyst loading was determined to be 1.5 wt.% of ECH for optimal conditions. In addition to this, they also performed
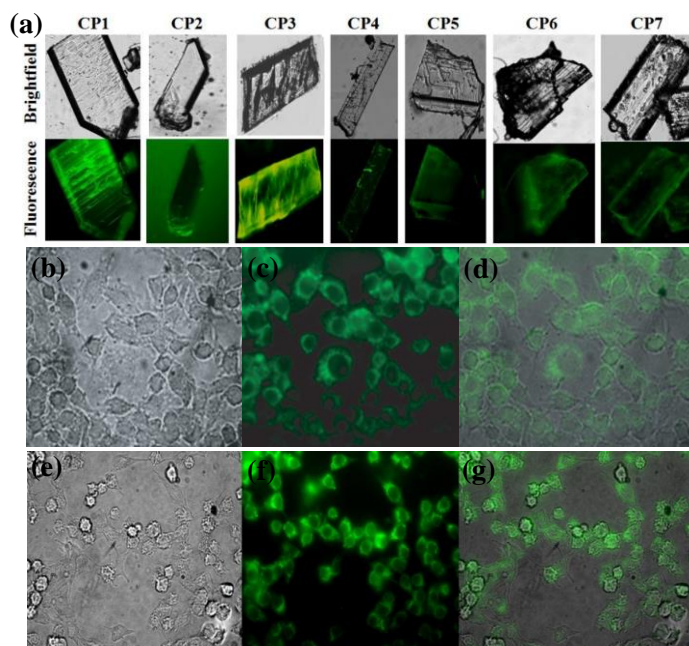
Figure 1.9: (a) Fluorescence and brightfield microscopic images of all seven CPs; Fluorescent microscopic images of RAW264.7 cells (b)-(d) incubated with **1** and (e)-(g) incubated with **3.**[93]

cycloaddition of CO_2 with other epoxides was also using Mn-BTC catalyst and the result obtained followed the order: Epichlorohydrin > Propene oxide >1,2-epoxybutane > Allyl glycidyl ether. Shi *et.* al.[95] used a a bitriazole ligand, 5′-(pyrazin-2-yl)-2H,4′H-3,3′-bi(1,2,4-triazole) (H2pzbtz) for the synthesis of CPs. The diverse coordinating modes of H2pzbtz ligand resulted in obtaining three new Mn-based CPs [{$Mn_3(pzbtz)_2(Cl)_2(H_2O)_2$}·$4H_2O$]n (**1**), [$Mn_2(pzbtz)(SO_4)(H_2O)_3$}·$3H_2O$]n (**2**) and [{$Mn_3(pzbtz)_3(H_2O)_3$}·$1.5DMA$·$2H_2O$]n (**3**). The results obtained from magnetic analysis disclosed the presence of antiferromagnetic interaction in all the three compounds while an additional spin canting behaviour was observed in case of compound **3**. In compound **3,** a sudden increase in magnetic susceptibility near 45 K was observed and they stated it to be uncompensated spin present along the structure which is attributed as spin canting. Also, compound **1** showed satisfactory selectivity towards CO_2 over CH_4 and N_2 with rare gate-opening phenomenon for CO_2 adsorption. Mahmoudi *et.* al.[96] synthesized two new Mn-based CPs [$Mn_2(\mu-L^1)_2(\mu-N_3)_2$]n (**1**) and [$Mn(\mu-HL^2)(SCN)_2$]n (**2**). They used HL^1 (2-acetylpyridine isonicotinoylhydrazone) and HL^2 (2-acetylpyridine nicotinoylhydrazone) linkers to construct the desired frameworks where **1** obtains a 2-D metal–organic layers and **2** obtains 1-D zigzag coordination chains.

Topological analysis classified the topologies to be uninodal 3-connected **hcb** layer in **1** and a uninodal 2-connected 2C1 chain in **2.** Moreover, the magnetic measurements confirmed the antiferromagnetic interactions present along the structures. Wang *et.* al.[97] synthesized a Mn-based layered CP ([Mn(tfbdc)(4,4'-bpy)(H$_2$O)$_2$] using 2,3,5,6-tetrafluoroterephthalic acid (H$_2$tfbdc) and 4,4'-bipyridine (4,4'-bpy) ligands and analysed the electrochemical properties. In CV curves, redox peaks around 0.3 and 0.46 V appeared which are originating from altering Mn-oxidation states. They stated the disappearance of oxidation peaks with increasing scan rate is due to diffusion controlled redox process might be changed to charge transfer controlled process. Charge-discharge profiles showed a high specific capacitance of 1098 F g^{-1} at a current density of 1 A g^{-1} while a persistence 92.6% of the initial specific capacitance were measured after 2000 cycles at a current density of 2 A g^{-1}. Du *et.* al.[98] afforded to synthesize [Mn$_3$(L)$_2$(OH)$_2$] CP using 2-carboxyethyl(phenyl)phosphinic acid (H$_2$L) ligand. A negative Weiss constant (θ= -34.0 K) indicates the dominant antiferromagnetic interaction between Mn(II) atoms while increase in χ_{mT} value below 18 K indicates the presence of uncompensating magnetic moment arising from spin frustrated/spin-competing interaction *via* μ_3-OH-bridged Mn$_3$ units. Chen *et.* al.[99] synthesized a new MOF [Mn$_3$(MA)(H$_2$O)$_2$(ipa)$_3$]$_n$ where they used isophthalic acid (H$_2$ipa) and Melamine (MA) as linkers. From the crystal structure, it's observed that an adjacent 2D layers were formed which gets extended into a 3D framework linked *via* MA and ipa^{2-}. These materials were later pyrolyzed at 500 & 600 °C and the product obtained were mixture of Mn$_3$O$_4$ & Mn$_2$O$_3$ and phase pure Mn$_2$O$_3$ respectively. As mentioned earlier, CP/MOF derived Mn$_x$O$_y$ materials are proved to be excellent electrode/superconductor materials as the obtained product retains the morphology of the parent material. GCD measurements displayed a specific capacitance of 75.6 to 18 F g^{-1} with charge–discharge current densities of 0.1 to 2.0 A g^{-1} for the product obtained at 500 °C whereas 13.3 F g^{-1} at the charge–discharge current densities of 0.1 A g^{-1} for the material obtained at 600 °C. They also stated that the capacitance properties observed in their work are superior to the previous reports. Ming *et.* al.[100] in their work reported two new Mn-MOFs [{Mn(L-Cl)(DMA)}(H$_2$O)]$_n$ (**1**) and [Mn(L-CH3)(DMA)]$_n$ (**2**) using 2,2'-dichloro-4,4'-azodibenzoic acid (H$_2$L-Cl) and 2,2'-dimethyl-4,4'-azodibenzoic acid (H$_2$L-CH$_3$) *via* solvothermal condition. Both the materials obtains a similar 3D framework with *Pcca* space group. They first examined the probable sensing of Hg^{2+} ions and interestingly,
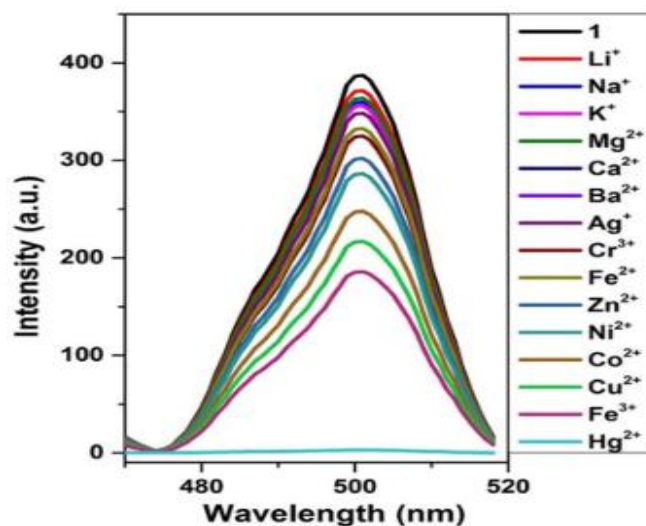
Figure 1.10: Emission spectra of **1** in presence of different metal ions.[100]

compound **1** shows significant emission quenching for Hg^{2+} upon exciting at 365 nm while for compound **2**, no such quenching was observed (*figure 1.10*). Further, they monitored sensing for other metal ions for **1** also where the highest quenching percentage observed was for Hg^{2+} ion only. Further, luminescence titration using Hg^{2+} supported these facts by showing decreasing emission intensities with increasing Hg^{2+} concentration. Also, recovery of fluorescence by emerging **1**@Hg^{2+} species on saturated $Mn(NO_3)_2$ solution suggests that Hg^{2+} can easily be removed in presence of $Mn(NO_3)_2$. Chen *et.* al.[101] reported phosphonate containing MOF [$Mn_3L_2(solvent)_2$]n (where L= (S or R)-3,3′-di-tert-butyl-5,5′-dicarboxyphenyl-6,6′-dimethylbiphenyl-2,2′-diylhydrogen phosphate) and performed heterogeneous catalysis of phenyl methyl sulphide with 2 mol% catalyst loading and afforded to obtain 93 % isolated yield of (R)-sulfoxide after 4 h (*figure 1.11*). An increase in reaction rate on increasing the
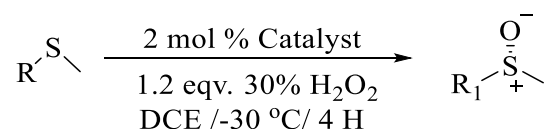
Figure 1.11: Scheme for oxidation of sulphide.[101]

oxidant amount was observed but no significant enantioselectivity was observed. Their study also includes catalysis using different substituents where 55 to 93% enantioselectivities were obtained. Raupp *et.* al.[46] has reported aerobic oxidation of α-pinene catalysed by Mn containing MOF. In their work, they have studied the different the conversion of α-pinene using Mn(III) acetate(as homogeneous catalyst) and Mn

containing MOF as catalyst (as heterogeneous catalyst), in different solvent and temperature environment (*figure 1.12*). They observed an increase in yield of α-pinene by increasing the reaction temperature from 100 ^{0}C to 130 ^{0}C and by increasing the air flow. But after a certain amount of air flow, there were no changes in the conversion rate which suggest an upper limit for the impact of oxygen. After comparing the results obtained, they found a similar conversion rate and selectivity of pinene oxide, verbenone and verbenol for both
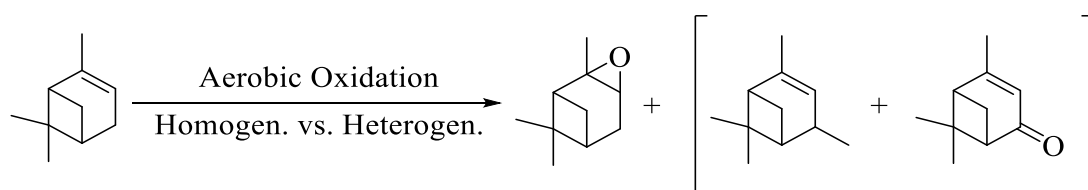
Figure 1.12: Scheme for aerobic oxidation of α-pinene.[46]

different catalytic environments. The Turn Over Number (TON) was higher compared to the homogeneous catalyst. The Mn-containing MOF showed a constant catalytic activity even after 5th catalytic cycle. Thus, they concluded that the use of heterogeneous catalysis for the oxidation of α-pinene is more advantageous than the homogenous catalysis as the catalyst is easily recoverable from the reaction medium and prevents the wastage.

In **2018**, Pal *et.* al.[102] reported a new Mn based CP [Mn$_6$(Ipa)$_6$(ad)·6H$_2$O] where they used isophthalate (Ipa) and adenine (ad) as linkers. They performed Henry Nitroaldol reaction using the compound as a heterogeneous catalyst and propped a possible meachanism. (*figure 1.13 (i)-(ii)*). Initially, they performed the reaction using 4-nitrobenzaldehyde
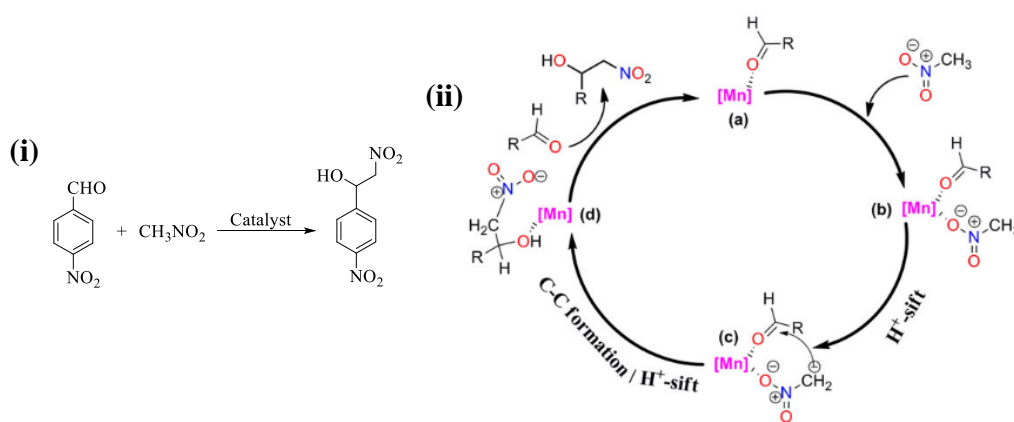
Figure 1.13: (i) Scheme for Henry's nitroaldol reaction & (ii) proposed meachanism.[102]

and nitromethane loading 1 mol% of the catalyst at 70 °C for 18 h which showed 80 % conversion of 4-nitrobenzaldehyde. Later, they further studied the effects of catalyst loading, solvent, temperature and reaction time. Conversion rate increases on increasing the catalyst loading from 1 to 5 mol% while a decrease in conversion rate was observed on further increasing the catalyst amount. The highest activity was observed when they used methanol as a solvent at 70 °C for 18h. Adpakpang *et. al.*[103] studied the liquid-phase water/ethanol separation using Mn-BDC MOF. Firstly, they screened the water stability of the materials by collecting XRD data before and after immerging in water. Activation processes facilitates the removal of the coordinated DMF molecules creating one accessible coordinatively unsaturated site (CUS). Vapour adsorption isotherms at 298 K using water & ethanol mixture disclosed strong evidence for the preferential adsorption of water. TGA results also supports greater adsorption of water than the available sites in Mn(II)-CUS providing an insight into the selective adsorption of water from a water/ethanol mixture. Demakov *et. al.*[104] reported Mn-CP [$Mn_3(chdc)_3$-$(NMP)_2(DMF)_2$] using Trans-1,4-cyclohexanedicarboxylate ($chdc^{2-}$) and *N*-methylpyrrolidone (NMP) linkers. It is the first example of CP using Mn(II) and 1,4-cyclohexanedicarboxylate anions without any additional aromatic rings which crystallizes in monoclinic crystal system with *P*21/*n* space group. Davarci *et. al.*[105] reported a Mn-CP [{$Mn(L)(Cl)_2(H_2O)$}.$(CH_3)_2CO$]$_n$ using dispiro-dipyridyloxy-cyclotriphosphazene (L) ligand. The 3D framework of the compound was constructed linking through classical hydrogen bonds (O-H···O and O-H···Cl interactions) and nonclassical weak C-H···O and C-H···Cl interactions. A significant effect of central metal atom was observed as same reaction condition and M/L ratio leads to form different coordinating environments. In addition to this, UV spectra of the ligand as well as the Mn-CP exhibited single absorption spectra near 260 nm where the M-L complex gives stronger absorption peak which corresponds to additional electronic transition due to presence of metal centre. Bikas *et. al.*[106] reported three Mn-based CPs [$Mn(H_2L)(NO_3)_2(CH_3OH)$]·CH_3OH]$_n$ (**1**), [$Mn(HL)(NO_3)(CH_3OH)$]$_n$ (**2**) and [$Mn(HL)(N_3)(CH_3OH)$]$_n$ (**3**) using biologically active coumarin-hydrazone ligand (*E*)-3-hydroxy-*N'*-(1-(2-oxo-2H-chromen-3-yl)ethylidene)-2-naphthohydrazide (H_2L). They first synthesized H_2L ligand by using 3-acetylcourmarin as precursor. Later, compound **1-3** were prepared where H_2L acts as the organic linker. Solving the crystal structure, the found the rare coordination mode of the H_2L ligand where it coordinates both chelating as well as in bridging mode. Fang *et. al.*[107]

utilized bithiophene-functionalized dicarboxylate ligand to synthesized a novel Mn-based CP [Mn(DMTDC)(DMF)] (**1**) where DMTDC (3,4-dimethylthieno[2,3-b]thiophene-2,5-dicarboxylic acid) is the dicarboxylate ligand. The framework exhibits a permanent porosity on removal of coordinated DMF by activation. Photocatalytic studies reveal that the pristine material (**1**) as well as the activated one (**1a**) can exceptionally degrade methyl orange (MO) and methylene blue (MB) which are among pollutant organic dyes (*figure 1.14*).
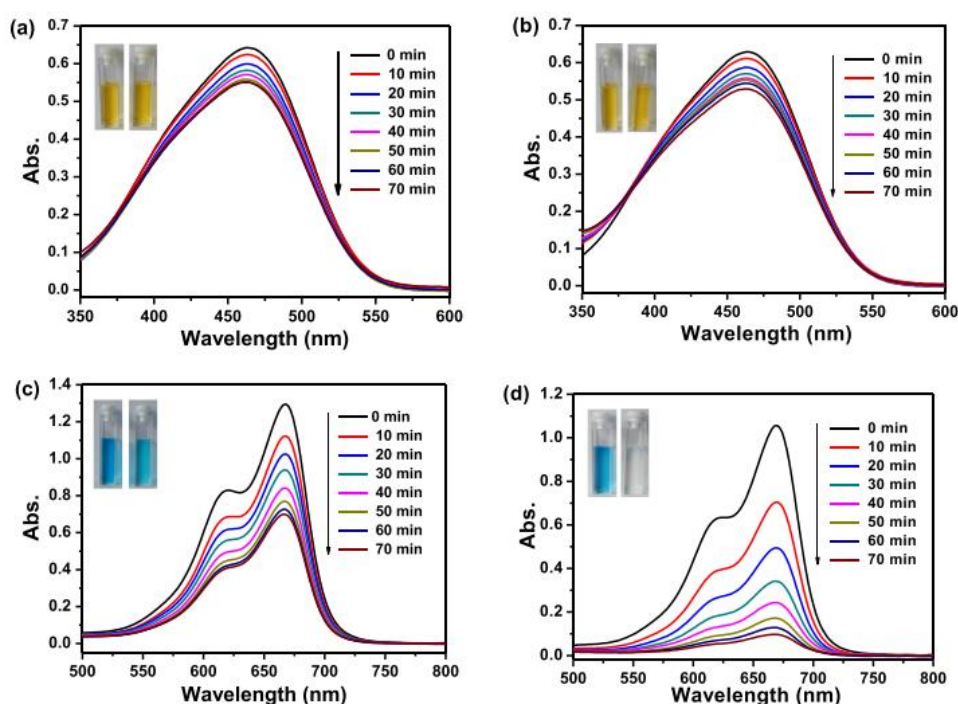
Figure 1.14: UV–Vis absorption spectra of the degradation of (a) 1 in MO; (b) 1a in MO; (c) 1 in MB; (d) 1a in MB.[107]

Kang *et.* al.[108] also reported two Mn-CPs {[Mn$_3$(Pfca)$_6$(Phen)$_2$]·2DMF}$_n$ (**I**) and [Mn(Pfca)$_2$(Phen)(H$_2$O)]$_n$ (**II**). Magnetic studies of both the materials indicated the presence of weak antiferromagnetism. Spirkl *et.* al.[109] reported a new Mn-CP named Mn-CFA-6 where they used 4,4'-Bipyrazolate (BPZ) ligand and bridging hydroxyl groups. The compound crystallizes in monoclinic crystal system with space group *C*2/*m*. From the single crystal structure, it's observed that both the two different Mn(III)-centres possesses unique identity which was supported with the UV/vis/NIR spectroscopy data where peaks at ~15600 cm^{-1} and ~22500 cm^{-1} represents two different manganese centres. Again, distinct bands near 15000 and 25000 cm^{-1} in UV/vis/NIR spectra are attributed to two different types of Manganese(III) centres while peaks above 30000 cm^{-1} tends to

$\pi \rightarrow \pi^*$ transitions of the ligand. During magnetic analysis, a sharp increase in susceptibility and a clear hysteresis loop was observed which was like ferromagnets. But a negative Weiss constant and linear variation of magnetization even at high magnetic field indicates the overall canted antiferromagnetic nature of the material.

In **2019**, Zou *et.* al.[110] studied the a newly synthesized Mn-based CP [Mn(TDC) (5,5′-dmbpy)(H$_2$O)]$_n$ where they used Thiophene-2,5-dicarboxylic acid (H$_2$TDC), 5,5′-dimethyl-2,2′-dipyridyl (5,5′-dmbpy) organic ligands. Here the building units are extended in one dimension forming zigzag chain arrangement. The 1D chain later forms a 3D supramolecular framework by assembling through π–π stacking and two types of H-bonding (O-H···O & weak C-H···O). However, magnetic studies revealed the existence of weak antiferromagnetic interactions among Mn(II) centres. Yaman *et.* at.[111] reported two Mn(II) CPs [Mn$_2$(μ_4-DMG)-(μ_4-DMG)(μ-BIPY)]$_n$ (**1**), and [Mn$_2$(μ_4-DMG)(μ_4-DMG)(μ-DPETEN)]$_n$ (**2**). Here compound **1** crystallizes in 3D framework whereas **2** crystallizes in 2-fold 3D-3D interpenetrating structure. The occurrence of interpenetration in **2** by two identical frameworks results in smaller pore size in the structure. Moreover, they observed two novel coordinating modes of 2,2-dimethylglutarate (DMG) ligand. Sundriyal *et.* al.[112] tested the supercapacitor application of electrodes modified with Mn-BDC MOF. In CV curve, the sharp redox peaks were observed at a scan rate of 20 mV/s which is imminent due to presence redox active Mn ions. They obtained a highest specific capacitance of 166.4 F/g at a scan rate of 1 mV/s which decreases gradually with increasing scan rates. Galvanostatic charge discharge (GCD) measurements also showed highest specific capacitance of 177.9 F/g at a current density of 0.5 A/g with non-linear curves which is due to pseudocapacitive nature of Mn-BDC. The charge-discharge cyclic analysis showed 98 % stability of the material after 2000 cycles which proved the high electrochemical stability of Mn-BDC MOF. Lan *et.* al.[113] synthesized four bimetallic MOFs by assembling *mer*-tricyanoiron(III) complex {(Ph$_4$P)[Fe(QXCP)(CN)$_3$]·0.5H$_2$O; (QXCP$^-$ = 8-(2-quinoxaline-2-carboxamido)quinoline anion)} and a Manganese(III) Schiff base compound as molecular precursor. Magnetic measurements revealed the presence of antiferromagnetic and ferromagnetic interaction between Fe(III) and Mn(III) centres present along the structure. From Magneto–Structural Correlation studies, they concluded the occurrence of magnetic interaction is mainly due to the t$_{2g}$^{5}e$_g$^{0} electronic arrangement of low-spin Fe^{III} ion and bending of the Mn–N≡C bridge. Li *et.* al.[114] reported

[Mn$_2$Cl$_2$(cptpy)$_2$(phdat)H$_2$O]$_n$ CP using 4'-(4-carboxyphenyl)-2,2':6',2''-terpyridine (Hcptpy) and 2,4-diamino-6-phenyltriazine (phdat) as linkers. The structure contains two different coordinating modes of carboxylic groups resulting in two different kinds of 1D chains. All the 1D chains extends into 3D stacking by π…π stacking and hydrogen bonding interactions. Here as well, weak antiferromagnetic behaviour among the Mn-centres were observed during magnetism analysis. Ge *et. al.*[115] synthesized and characterized Mn-MOF [Mn(HL)(C$_2$H$_5$OH)]$_n$ using a multifunctional ligand 2-(5-bromo-pyridin-3-yl)-1H-imidazole-4,5-dicarboxylic acid (H$_3$L). They used NaOH to deprotonate the carboxylic acids present in the H$_3$L linkers. Structural analysis provides an indication about the antiferromagnetic interaction based on previous reports. Thus, they performed magnetic susceptibility analysis which also confirms the existence of weak antiferromagnetic interaction with spin-coupling constant of –0.71 cm^{-1}. Meng *et. al.*[116] reported a herringbone like Mn-CP where 1-(2-hydroxy-benzamido)-2-(2-hydroxy-5-nitrobenzylideneamino)-ethane (**H$_3$L**) linkers forming the overall framework.
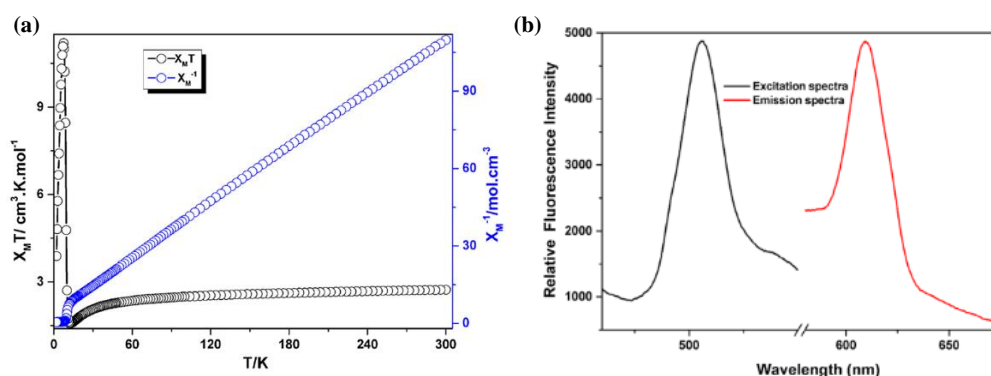
Figure 1.15: (a) Magnetism curves & (b) Excitation spectrum of [MnL]n CP.[116]

While performing temperature dependent magnetic susceptibility measurements, they observed a sudden increase in magnetization near 7.5 K which on further analysing with ZFC and FC measurements validates the spin canting behaviour (*figure 1.15 (a)*). This kind of behaviour is commonly observed in compounds containing Mn(III) centres having molecular chains elongated in tetragonal environment with short basal bonds. As the crystal structure contains long range of conjugation, a red emission shift with broadband near 580-650 nm was observed compared to the emission spectrum of the bare ligand (*figure 1.15 (b)*). The emission lifetime τ of [MnL]$_n$ was also measured to be 0.28 ms and longer than that of free ligand H$_3$L (undetectable for the H$_3$L under the same conditions). Meng *et. al.*[117] solvothermally synthesized a 3D CP

[{Mn$_{1.5}$(H$_3$L)(bibp)$_{0.5}$(H$_2$O)$_2$}·3H$_2$O]$_n$ where they used 1,3,5-triazine-2,4,6-triaminehexaa-aoetic acid (H$_3$L^{3-}) and 1,4-bis((4-imidazol-1-yl)benzyl)piperazine) (bibp) as linkers. Thoroughly analysing the single crystal structure, they observed five H$_2$O molecules in the structure- 3 uncoordinated and 2 coordinated. The Mn(II) centres coordinated with H$_3$L^{3-} forms an 1D chain which forms a 2D layer through bibp ligands and these 2D layers stack together forming a 3D framework. Morales *et.* al.[118] synthesized a Mn-CP [Mn(H$_2$O)(mal)(5dmb)·H$_2$O}$_n$] incorporating maleic acid (mal) and 5,5′-dimethyl-2,2′-bipyridine (5dmb) ligands. They explained the crystal geometry of the obtained framework which crystallizes in orthorhombic geometry with Pna2$_1$ space group and forms a 1D CP. The metal centre is coordinated to four oxygen atoms- three O-atoms from two different mal ligands and one O-atom of water molecule; and two nitrogen atoms from one 5dmb ligand. Moreover, the uncoordinated O-atoms of the mal ligands forms hydrogen bonding the water molecules present in the framework. Sharma *et.* al.[119] synthesized MOF-1 [{Mn(TCPP)$_{0.5}$(H$_2$O)$_2$}.2H$_2$O]$_n$ using 5,10,15,20-Tetrakis(4-benzoate)porphyrinato-Mn(II) (Mn-TCPP) as linkers. The framework crystallizes in monoclinic crystal system with C2/m space group and has a 2D network. BET N$_2$ adsorption isotherm data resulted in a surface area of 10.1 m^{2}g^{-1} whereas a surface area of 42.5 m^{2}g^{-1} was observed for CO$_2$ adsorption. They studied the catalytic activity of visible-light-assisted MOF-1 which showed significant increase in reactivity during cycloaddition of CO$_2$ with epichlorohydrin (*figure 1.16*) and an increase in conversion rate of 53.5 % (in absence of visible light) to 100 % (in visible light
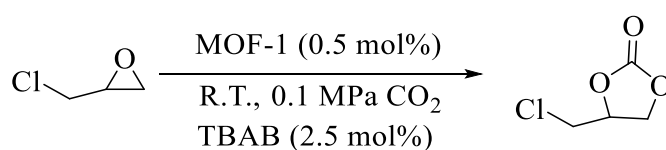
Figure 1.16: Scheme for cycloaddition of CO$_2$ with epichlorohydrin.[119]

irradiation) suggesting the critical role of photosensitization of the catalyst. A comparison of catalytic activity of visible-light-irradiated MOF-1 with reported MOFs also showed the superior activity of MOF-1 than others. Recyclability test showed no significant change in catalytic activity of the catalyst till five cycles proving the catalytic efficiency of MOF-1. Xiao *et.* al.[120] reported two Mn(II) CPs, NCST-3 [Mn(NDC)(L)(H$_2$O)]$_n$ and NCST-4 [{Mn$_2$(HBTC)$_2$(L)$_2$(H$_2$O)$_2$]·2H$_2$O}]$_n$ using 1,4-bis(5,6-dimethylbenzimidazole)butane (L), 1,4-naphthalene dicarboxylic acid (1,4-

H_2NDC), and 1,3,5-benzenetricarboxylic acid (H_3BTC) ligands. They evaluated the bandgap of both materials which were found to be 3.37 eV and 3.92 eV respectively. To analyse the photocatalytic activities, they degraded four organic dyes including methylene blue (MB), Rhodamine B (RhB), methyl violet (MV) and methyl orange (MO) under the UV irradiation. After 2-2.5 h observation, efficiencies of NCST-3 were found to be 98.13% (for MB), 98.24% (for RhB), 88.55% (for MV) and 69.74% (for MO). Whereas, efficiencies of NCST-4 were found to be 89.93%, 97.70%, 82.95%, and 21.13% for MB, RhB, MV and MO, respectively. Fluorescence spectra revealed the red shift of NCST-3 (Δ= 64 nm) and NCST-4 (Δ= 81 nm) from the maximum emission intensity observed for the ligand (λ= 279 nm). This phenomenon was attributed to the ligand-to-metal charge-transfer transition. Furthermore, the effect of solvent on the fluorescent activity of the materials was studied and found that different solvents boosts the quenching of fluorescent activity. Apart from these, they also experimentally analysed the ion sensing activity of the compounds. In NCST-3, different fluorescence quenching effect was observed for different ions except that Al^{3+} slightly enhances the emission intensity while the intensity of NCST-4 sharply decreased on addition of Ag^+. Xu *et. al.*[121] synthesized Mn-MOF using 1,3,5-benzenetricarboxylic acids linkers. They performed CV measurements to analyse the electrochemical performance of the material. CV curves establishes pseudocapacitive feature of the Mn-MOF and diffusion-controlled kinetics of electrolyte ions. Furthermore, galvanostatic charge-discharge study revealed the double-layer charge storage process and the pseudocapacitive nature. They calculated the maximum specific capacitance to be 89 F g^{-1} at current density 0.5 A g^{-1} and energy density of 31.6 Wh kg^{-1} which was much higher than the previous reports. Also, the material retains good recyclability of about 91.8% of the initial capacitance after 10,000 cycles indicating excellent life cycle and electrochemical reversibility.

In **2020**, Dutta *et. al.*[122] synthesized 1D Mn-based CP [M(adc)(4-spy)$_2$(H$_2$O)$_2$]$_n$ where they incorporated acetylenedicarboxylic acid (H$_2$adc) and 4-styrylpyridine (4-spy) as organic linkers after seven days of reaction time. Intermolecular hydrogen bonding between coordinated aqua molecules were found and presence of bridged carboxylate ligands in the crystal structure giving an inkling of antiferromagnetic interaction among the metal centres which has been confirmed by performing variable temperature magnetic susceptibility measurements. Weiss constant was calculated which was found to be negative (θ= -8.8 K) and additionally, the absence of hysteresis loop in isothermal

magnetization measurements further gives evidence for existence of antiferromagnetic properties.

Taking in account of this above survey, we fixed our goal to work with manganese salts and various carboxylate based ligands to synthesize CPs. Our main aim and objectives of this study are:

i. To construct novel porous coordinate polymers based on manganese with various carboxylate organic ligands.

ii. Characterization of the materials and ligands using conventional spectroscopic techniques and analytical tools.

iii. To explore the properties of synthesized material for various applications.

Reference:

(1)   Garcia, Y.; Su, B. L. No Inorganic Materials, No Progress. *Eur. J. Inorg. Chem.* **2019**, *2019*, 3123–3125.

(2)   Osadchii, D. Y.; Olivos-Suarez, A. I.; Szécsényi, Á.; Li, G.; Nasalevich, M. A.; Dugulan, I. A.; Crespo, P. S.; Hensen, E. J. M.; Veber, S. L.; Fedin, M. V.; et al. Isolated Fe Sites in Metal Organic Frameworks Catalyze the Direct Conversion of Methane to Methanol. *ACS Catal.* **2018**, *8*, 5542–5548.

(3)   Periono, R. A.; Taube, D. J.; Gamble, S.; Taube, H.; Satoh, T.; Fujii, H.; Vlcek A., J. Platinum Catalysts for the High-Yield Oxidation of Methane to a Methanol Derivative. *Chemtracts* **1999**, *12*, 130–134.

(4)   Kim, R. S.; Surendranath, Y. Electrochemical Reoxidation Enables Continuous Methane-to-Methanol Catalysis with Aqueous Pt Salts. *ACS Cent. Sci.* **2019**, *5*, 1179–1186.

(5)   Periana, R. A.; Bhalla, G.; Tenn, W. J.; Young, K. J. H.; Liu, X. Y.; Mironov, O.; Jones, C. J.; Ziatdinov, V. R. Perspectives on Some Challenges and Approaches for Developing the next Generation of Selective, Low Temperature, Oxidation Catalysts for Alkane Hydroxylation Based on the CH Activation Reaction. *J. Mol. Catal. A Chem.* **2004**, *220*, 7–25.

(6)   Mofarahi, M.; Gholipour, F. Gas Adsorption Separation of CO_2/CH_4 System Using Zeolite 5A. *Microporous Mesoporous Mater.* **2014**, *200*, 1–10.

(7)   Xue, C. L.; Cheng, W. P.; Hao, W. M.; Ma, J. H.; Li, R. F. CH 4 /N 2 Adsorptive Separation on Zeolite X/AC Composites. *J. Chem.* **2019**, *2019*, 1–9.

(8)   Hauchhum, L.; Mahanta, P. Carbon Dioxide Adsorption on Zeolites and Activated Carbon by Pressure Swing Adsorption in a Fixed Bed. *Int. J. Energy Environ. Eng.* **2014**, *5*, 349–356.

(9)   Arora, Y.; Seth, C.; Khushalani, D. Crafting Inorganic Materials for Use in Energy Capture and Storage. *Langmuir* **2019**, *35*, 9101–9114.

(10)   Ponrouch, A.; Monti, D.; Boschin, A.; Steen, B.; Johansson, P.; Palacín, M. R. Non-Aqueous Electrolytes for Sodium-Ion Batteries. *J. Mater. Chem. A* **2015**, *3*,

22–42.

(11)   Ouahab, L. Coordination Complexes in Conducting and Magnetic Molecular Materials. *Coord. Chem. Rev.* **1998**, *178–180* (PART 2), 1501–1531.

(12)   Tamaki, H.; Matsumoto, N.; Koikawa, M.; Achiwa, N.; Okawa, H.; Zhong, Z. J.; Kida, S.; Hashimoto, Y. Design of Metal-Complex Magnets. Syntheses and Magnetic Properties of Mixed-Metal Assemblies {NBu4[MCr(Ox)3]}x (NBu4+ = Tetra(n-Butyl)Ammonium Ion; Ox2- = Oxalate Ion; M = Mn2+, Fe2+, Co2+, Ni2+, Cu2+, Zn2+). *J. Am. Chem. Soc.* **1992**, *114*, 6974–6979.

(13)   Leong, W. L.; Vittal, J. J. One-Demensional Coordination Polymers: Complexity and Diversity in Structures, Properties, and Applications. *Chem. Rev.* **2011**, *111*, 688–764.

(14)   Jin, H.; Li, J.; Iocozzia, J.; Zeng, X.; Wei, P.-C.; Yang, C.; Li, N.; Liu, Z.; He, J. H.; Zhu, T.; et al. Hybrid Organic-Inorganic Thermoelectric Materials and Devices. *Angew. Chemie Int. Ed.* **2019**, *58*, 15206–15226.

(15)   Yu, K. J.; Yan, Z.; Han, M.; Rogers, J. A. Inorganic Semiconducting Materials for Flexible and Stretchable Electronics. *npj Flex. Electron.* **2017**, *1*, 1–14.

(16)   Kim, T. W.; Yang, Y.; Li, F.; Kwan, W. L. Electrical Memory Devices Based on Inorganic/Organic Nanocomposites. *NPG Asia Mater.* **2012**, *4* , 1–12.

(17)   Silva, J. *Inorganic Fertilizer Materials*; **2000**.

(18)   Opala, P. A.; Okalebo, J. R.; Othieno, C. O. Effects of Organic and Inorganic Materials on Soil Acidity and Phosphorus Availability in a Soil Incubation Study. *ISRN Agron.* **2012**, *2012*, 1–10.

(19)   Yan, Y.; He, T.; Zhao, B.; Qi, K.; Liu, H.; Xia, B. Y. Metal/Covalent-Organic Frameworks-Based Electrocatalysts for Water Splitting. *J. Mater. Chem. A* **2018**, *6*, 15905–15926.

(20)   Cardenas-Morcoso, D.; Ifraemov, R.; García-Tecedor, M.; Liberman, I.; Gimenez, S.; Hod, I. A Metal-Organic Framework Converted Catalyst That Boosts Photo-Electrochemical Water Splitting. *J. Mater. Chem. A* **2019**, *7*, 11143–11149.

(21)　Yun, S.; Hagfeldt, A.; Ma, T. Pt-Free Counter Electrode for Dye-Sensitized Solar Cells with High Efficiency. *Adv. Mater.* **2014**, *26*, 6210–6237.

(22)　Ahmad, S.; Yum, J.-H.; Butt, H.-J.; Nazeeruddin, M. K.; Grätzel, M. Efficient Platinum-Free Counter Electrodes for Dye-Sensitized Solar Cell Applications. *ChemPhysChem* **2010**, *11*, 2814–2819.

(23)　Jena, A. K.; Kulkarni, A.; Miyasaka, T. Halide Perovskite Photovoltaics: Background, Status, and Future Prospects. *Chem. Rev.* **2019**, *119* , 3036–3103.

(24)　Tai, Q.; Tang, K. C.; Yan, F. Recent Progress of Inorganic Perovskite Solar Cells. *Energy Environ. Sci.* **2019**, *12*, 2375–2405.

(25)　Thapa, S.; Bhardwaj, K.; Basel, S.; Pradhan, S.; Eling, C. J.; Adawi, A. M.; Bouillard, J. S. G.; Stasiuk, G. J.; Reiss, P.; Pariyar, A.; et al. Long-Term Ambient Air-Stable Cubic CsPbBr3 Perovskite Quantum Dots Using Molecular Bromine. *Nanoscale Adv.* **2019**, *1*, 3388–3391.

(26)　Abas, N.; Kalair, A.; Khan, N. Review of Fossil Fuels and Future Energy Technologies. *Futures* **2015**, *69*, 31–49.

(27)　Kåberger, T. Progress of Renewable Electricity Replacing Fossil Fuels. *Glob. Energy Interconnect.* **2018**, *1*, 48–52.

(28)　Son, Y. H.; Bui, P. T. M.; Lee, H. R.; Akhtar, M. S.; Shah, D. K.; Yang, O. B. A Rapid Synthesis of Mesoporous Mn2O3 Nanoparticles for Supercapacitor Applications. *Coatings* **2019**, *9*, 1-11.

(29)　Hazarika, K. K.; Goswami, C.; Saikia, H.; Borah, B. J.; Bharali, P. Cubic Mn_2O_3 Nanoparticles on Carbon as Bifunctional Electrocatalyst for Oxygen Reduction and Oxygen Evolution Reactions. *Mol. Catal.* **2018**, *451*, 153–160.

(30)　Jahan, M.; Tominaka, S.; Henzie, J. Phase Pure α-Mn 2 O 3 Prisms and Their Bifunctional Electrocatalytic Activity in Oxygen Evolution and Reduction Reactions. *Dalt. Trans.* **2016**, *45*, 18494–18501.

(31)　Xia, W.; Mahmood, A.; Liang, Z.; Zou, R.; Guo, S. Earth-Abundant Nanomaterials for Oxygen Reduction. *Angew. Chemie Int. Ed.* **2016**, *55*, 2650–2676.

(32) Salunkhe, R. R.; Kaneti, Y. V.; Yamauchi, Y. Metal-Organic Framework-Derived Nanoporous Metal Oxides toward Supercapacitor Applications: Progress and Prospects. *ACS Nano* **2017**, *11*, 5293–5308.

(33) Xie, Z.; Xu, W.; Cui, X.; Wang, Y. Recent Progress in Metal–Organic Frameworks and Their Derived Nanostructures for Energy and Environmental Applications. *ChemSusChem* **2017**, *10*, 1645–1663.

(34) Mai, H. D.; Rafiq, K.; Yoo, H. Nano Metal-Organic Framework-Derived Inorganic Hybrid Nanomaterials: Synthetic Strategies and Applications. *Chem. - A Eur. J.* **2017**, *23*, 5631–5651.

(35) Robin, A. Y.; Fromm, K. M. Coordination Polymer Networks with O- and N-Donors: What They Are, Why and How They Are Made. *Coord. Chem. Rev.* **2006**, *250*, 2127–2157.

(36) Archer, R. D. Preparative Inorganic Reactions. Volume. *J. Am. Chem. Soc.* **1965**, *87*, 1151–1152.

(37) Chen, X.-M. Assembly Chemistry of Coordination Polymers. In *Modern Inorganic Synthetic Chemistry*; Elsevier, **2011**; 207–225.

(38) Kitagawa, S.; Kitaura, R.; Noro, S. I. Functional Porous Coordination Polymers. *Angew. Chemie - Int. Ed.* **2004**, *43*, 2334–2375.

(39) Stock, N.; Biswas, S. Synthesis of Metal-Organic Frameworks (MOFs): Routes to Various MOF Topologies, Morphologies, and Composites. *Chem. Rev.* **2012**, *112*, 933–969.

(40) Li, N.; Feng, R.; Zhu, J.; Chang, Z.; Bu, X. H. Conformation Versatility of Ligands in Coordination Polymers: From Structural Diversity to Properties and Applications. *Coord. Chem. Rev.* **2018**, *375*, 558–586.

(41) Jiang, H. L.; Makal, T. A.; Zhou, H. C. Interpenetration Control in Metal-Organic Frameworks for Functional Applications. *Coord. Chem. Rev.* **2013**, *257*, 2232–2249.

(42) Gong, Y. N.; Zhong, D. C.; Lu, T. B. Interpenetrating Metal-Organic Frameworks. *CrystEngComm* **2016**, *18*, 2596–2606.

(43)   Verma, G.; Butikofer, S.; Kumar, S.; Ma, S. Regulation of the Degree of Interpenetration in Metal–Organic Frameworks. *Top. Curr. Chem.* **2020**, *378*, 1–45.

(44)   Cui, W. G.; Zhang, G. Y.; Hu, T. L.; Bu, X. H. Metal-Organic Framework-Based Heterogeneous Catalysts for the Conversion of C1 Chemistry: CO, CO 2 and CH 4. *Coord. Chem. Rev.* **2019**, *387*, 79–120.

(45)   Zhu, L.; Liu, X. Q.; Jiang, H. L.; Sun, L. B. Metal-Organic Frameworks for Heterogeneous Basic Catalysis. *Chem. Rev.* **2017**, *117*, 8129–8176.

(46)   Raupp, Y. S.; Yildiz, C.; Kleist, W.; Meier, M. A. R. Aerobic Oxidation of α-Pinene Catalyzed by Homogeneous and MOF-Based Mn Catalysts. *Appl. Catal. A Gen.* **2017**, *546*, 1–6.

(47)   Tu, T. N.; Nguyen, M. V.; Nguyen, H. L.; Yuliarto, B.; Cordova, K. E.; Demir, S. Designing Bipyridine-Functionalized Zirconium Metal–Organic Frameworks as a Platform for Clean Energy and Other Emerging Applications. *Coord. Chem. Rev.* **2018**, *364*, 33–50.

(48)   Agarwal, R. A.; Gupta, N. K. CO2 Sorption Behavior of Imidazole, Benzimidazole and Benzoic Acid Based Coordination Polymers. *Coord. Chem. Rev.* **2017**, *332*, 100–121.

(49)   Dincă, M.; Long, J. R. Hydrogen Storage in Microporous Metal-Organic Frameworks with Exposed Metal Sites. *Angew. Chemie - Int. Ed.* **2008**, *47*, 6766–6779.

(50)   Lustig, W. P.; Li, J. Luminescent Metal–Organic Frameworks and Coordination Polymers as Alternative Phosphors for Energy Efficient Lighting Devices. *Coord. Chem. Rev.* **2018**, *373*, 116–147.

(51)   An, H.; Li, M.; Gao, J.; Zhang, Z.; Ma, S.; Chen, Y. Incorporation of Biomolecules in Metal-Organic Frameworks for Advanced Applications. *Coord. Chem. Rev.* **2019**, *384*, 90–106.

(52)   Lim, E. K.; Kim, T.; Paik, S.; Haam, S.; Huh, Y. M.; Lee, K. Nanomaterials for Theranostics: Recent Advances and Future Challenges. *Chem. Rev.* **2015**, *115*,

327–394.

(53)   Horcajada, P.; Chalati, T.; Serre, C.; Gillet, B.; Sebrie, C.; Baati, T.; Eubank, J. F.; Heurtaux, D.; Clayette, P.; Kreuz, C.; et al. Porous Metal-Organic-Framework Nanoscale Carriers as a Potential Platform for Drug Deliveryand Imaging. *Nat. Mater.* **2010**, *9*, 172–178.

(54)   He, Y.; Chen, F.; Li, B.; Qian, G.; Zhou, W.; Chen, B. Porous Metal–Organic Frameworks for Fuel Storage. *Coord. Chem. Rev.* **2018**, *373*, 167–198.

(55)   Xu, G.; Nie, P.; Dou, H.; Ding, B.; Li, L.; Zhang, X. Exploring Metal Organic Frameworks for Energy Storage in Batteries and Supercapacitors. *Mater. Today* **2017**, *20*, 191–209.

(56)   Yue, Q.; Gao, E. Q. Azide and Carboxylate as Simultaneous Coupler for Magnetic Coordination Polymers. *Coord. Chem. Rev.* **2019**, *382*, 1–31.

(57)   Son, K.; Kim, J. Y.; Schütz, G.; Kang, S. G.; Moon, H. R.; Oh, H. Coordinated Molecule-Modulated Magnetic Phase with Metamagnetism in Metal-Organic Frameworks. *Inorg. Chem.* **2019**, *58*, 8895–8899.

(58)   Jiang, X.; Liu, C. M.; Kou, H. Z. Porous Coordination Polymers Based on {Mn6} Single-Molecule Magnets. *Inorg. Chem.* **2016**, *55*, 5880–5885.

(59)   Suárez-García, S.; Arias-Ramos, N.; Frias, C.; Candiota, A. P.; Arús, C.; Lorenzo, J.; Ruiz-Molina, D.; Novio, F. Dual T1/ T2 Nanoscale Coordination Polymers as Novel Contrast Agents for MRI: A Preclinical Study for Brain Tumor. *ACS Appl. Mater. Interfaces* **2018**, *10*, 38819–38832.

(60)   Xu, Y.; Li, Q.; Xue, H.; Pang, H. Metal-Organic Frameworks for Direct Electrochemical Applications. *Coord. Chem. Rev.* **2018**, *376*, 292–318.

(61)   Lou, X.; Ning, Y.; Li, C.; Shen, M.; Hu, B.; Hu, X.; Hu, B. Exploring the Capacity Limit: A Layered Hexacarboxylate-Based Metal-Organic Framework for Advanced Lithium Storage. *Inorg. Chem.* **2018**, *57*, 3126–3132.

(62)   Worrall, S. D.; Bissett, M. A.; Hirunpinyopas, W.; Attfield, M. P.; Dryfe, R. A. W. Facile Fabrication of Metal-Organic Framework HKUST-1-Based Rewritable Data Storage Devices. *J. Mater. Chem. C* **2016**, *4*, 8687–8695.

(63)   Huang, Y.; Zhang, J.; Yue, D.; Cui, Y.; Yang, Y.; Li, B.; Qian, G. Solvent-Triggered Reversible Phase Changes in Two Manganese-Based Metal–Organic Frameworks and Associated Sensing Events. *Chem. - A Eur. J.* **2018**, *24*, 13231–13237.

(64)   Wang, M. Q.; Ye, C.; Bao, S. J.; Zhang, Y.; Yu, Y. N.; Xu, M. W. Carbon Nanotubes Implanted Manganese-Based MOFs for Simultaneous Detection of Biomolecules in Body Fluids. *Analyst* **2016**, *141*, 1279–1285.

(65)   Remya, V. R.; Kurian, M. Synthesis and Catalytic Applications of Metal–Organic Frameworks: A Review on Recent Literature. *Int. Nano Lett.* **2019**, *9*, 17–29.

(66)   Feng, S.-H.; Li, G.-H. Hydrothermal and Solvothermal Syntheses. In *Modern Inorganic Synthetic Chemistry, Second Edition*; Elsevier, **2017**; 73–104.

(67)   Loera-Serna, S.; Ortiz, E. Catalytic Applications of Metal-Organic Frameworks. In *Advanced Catalytic Materials - Photocatalysis and Other Current Trends*; Norena, L. E., Wang, J.-A., Eds.; InTech, **2016**; 95–122.

(68)   Klinowski, J.; Almeida Paz, F. A.; Silva, P.; Rocha, J. Microwave-Assisted Synthesis of Metal-Organic Frameworks. *Dalt. Trans.* **2011**, *40*, 321–330.

(69)   Seth, S.; Matzger, A. J. Metal−Organic Frameworks: Examples, Counterexamples, and an Actionable Definition. *Cryst. Growth Des.* **2017**, *17*, 4043–4048.

(70)   Rowsell, J. L. C.; Yaghi, O. M. Metal–Organic Frameworks: A New Class of Porous Materials. *Microporous Mesoporous Mater.* **2004**, *73*, 3–14.

(71)   Biradha, K.; Ramanan, A.; Vittal, J. J. Coordination Polymers Versus Metal−Organic Frameworks. *Cryst. Growth Des.* **2009**, *9*, 2969–2970.

(72)   Sun, H. L.; Gao, S.; Ma, B. Q.; Su, G.; Batten, S. R. Structures and Magnetism of a Series Mn(II) Coordination Polymers Containing Pyrazine-Dioxide Derivatives and Different Anions. *Cryst. Growth Des.* **2005**, *5*, 269–277.

(73)   Rosi, N. L.; Kim, J.; Eddaoudi, M.; Chen, B.; O'Keeffe, M.; Yaghi, O. M. Rod Packings and Metal-Organic Frameworks Constructed from Rod-Shaped Secondary Building Units. *J. Am. Chem. Soc.* **2005**, *127*, 1504–1518.

(74)   Wang, X. Y.; Wang, L.; Wang, Z. M.; Su, G.; Gao, S. Coexistence of Spin-Canting, Metamagnetism, and Spin-Flop in a (4,4) Layered Manganese Azide Polymer. *Chem. Mater.* **2005**, *17*, 6369–6380.

(75)   Tang, Y. Z.; Wang, X. Sen; Zhou, T.; Xiong, R. G. A Novel 2D Manganese(II) Coordination Polymer Exhibiting Ferromagnetic Interaction. *Cryst. Growth Des.* **2006**, *6*, 11–13.

(76)   Hoi, R. M.; Kobayashi, N.; Myunghyun, P. S. Porous Metal-Organic Framework with Coordinatively Unsaturated Mn II Sites:Sorption Properties for Various Gases. *Inorg. Chem.* **2006**, *45*, 8672–8676.

(77)   Yuan, M.; Zhao, F.; Zhang, W.; Wang, Z. M.; Gao, S. Azide-Bridged One-Dimensional MnIII Polymers: Effects of Side Group of Schiff Base Ligands on Structure and Magnetism. *Inorg. Chem.* **2007**, *46*, 11235–11242.

(78)   Taylor, K. M. L.; Rieter, W. J.; Lin, W. Manganese-Based Nanoscale Metal-Organic Frameworks for Magnetic Resonance Imaging. *J. Am. Chem. Soc.* **2008**, *130*, 14358–14359.

(79)   Horike, S.; Dincă, M.; Tamaki, K.; Long, J. R. Size-Selective Lewis Acid Catalysis in a Microporous Metal-Organic Framework with Exposed Mn2+ Coordination Sites. *J. Am. Chem. Soc.* **2008**, *130*, 5854–5855.

(80)   Zhang, X.; Ge, C.; Yin, J.; Zhao, Y.; He, C. Interpenetrating 2D Manganese(II) Coordination Polymer Supported by 4,4'-Bis(Dimethoxyphosphorylmethyl)-Biphenyl Ligands. *Chinese J. Chem.* **2009**, *27*, 1195–1198.

(81)   Ladrak, T.; Smulders, S.; Roubeau, O.; Teat, S. J.; Gamez, P.; Reedijk, J. Manganese-Based Metal-Organic Frameworks as Heterogeneous Catalysts for the Cyanosilylation of Acetaldehyde. *Eur. J. Inorg. Chem.* **2010**, *2010*, 3804–3812.

(82)   Li, N.; Chen, L.; Lian, F.; Jiang, F.; Hong, M. Manganese(II) Complexes with V-Shaped Sulfonyldibenzoate: The 3D Structures with Interpenetrated Threefold or Tetra-Nuclear Manganese(II) Units. *Inorganica Chim. Acta* **2010**, *363*, 3291–3301.

(83)   Yang, J. W.; Zhang, J.; Yan, Y.; Huang, X. C.; Tong, S. L. A Coordination Polymer of Manganese (III) Porphyrinate with Right-Handed Helicity and Opticity. *Solid State Sci.* **2010**, *12*, 1242–1247.

(84)   Xie, M. H.; Yang, X. L.; Wu, C. De. From 2D to 3D: A Single-Crystal-to-Single-Crystal Photochemical Framework Transformation and Phenylmethanol Oxidation Catalytic Activity. *Chem. - A Eur. J.* **2011**, *17*, 11424–11427.

(85)   Liu, Q.; Yu, L.; Wang, Y.; Ji, Y.; Horvat, J.; Cheng, M. L.; Jia, X.; Wang, G. Manganese-Based Layered Coordination Polymer: Synthesis, Structural Characterization, Magnetic Property, and Electrochemical Performance in Lithium-Ion Batteries. *Inorg. Chem.* **2013**, *52*, 2817–2822.

(86)   Zhao, Y. P.; Yang, H.; Wang, F.; Du, Z. Y. A Microporous Manganese-Based Metal-Organic Framework for Gas Sorption and Separation. *J. Mol. Struct.* **2014**, *1074*, 19–21.

(87)   Lv, Y.; Shi, P.; Shen, W.; Chen, X.; Zhao, G. A Series of Novel Zn(II) and Mn(II) Metal-Organic Frameworks Constructed by 2,4-Bis-Oxyacetate-Benzoic Acid: Syntheses, Structures and Photoluminescence. *Sci. China Chem.* **2015**, *58*, 448–456.

(88)   Zhang, Y.; Lin, B.; Sun, Y.; Zhang, X.; Yang, H.; Wang, J. Carbon Nanotubes@metal–Organic Frameworks as Mn-Based Symmetrical Supercapacitor Electrodes for Enhanced Charge Storage. *RSC Adv.* **2015**, *5*, 58100–58106.

(89)   Li, T.; Li, C.; Hu, X.; Lou, X.; Hu, H.; Pan, L.; Chen, Q.; Shen, M.; Hu, B. Reversible Lithium Storage in Manganese and Cobalt 1,2,4,5-Benzenetetracarboxylate Metal-Organic Framework with High Capacity. *RSC Adv.* **2016**, *6*, 61319–61324.

(90)   Dey, S. K.; Hazra, M.; Thompson, L. K.; Patra, A. Manganese(II) Coordination Polymer Having Pyrazine and µ-Phenolato Bridging: Structure, Magnetism and Biological Studies. *Inorganica Chim. Acta* **2016**, *443*, 224–229.

(91)   Hu, H.; Lou, X.; Li, C.; Hu, X.; Li, T.; Chen, Q.; Shen, M.; Hu, B. A Thermally

Activated Manganese 1,4-Benzenedicarboxylate Metal Organic Framework with High Anodic Capability for Li-Ion Batteries. *New J. Chem.* **2016**, *40*, 9746–9752.

(92) Das, K.; Datta, A.; Beyene, B. B.; Massera, C.; Garribba, E.; Sinha, C.; Akitsu, T.; Tanka, S. A Zig-Zag End-to-End Azido Bridged MnIII 1-D Coordination Polymer: Spectral Elucidation, Magnetism, Redox Study and Biological Activity. *Polyhedron* **2017**, *127*, 315–322.

(93) Paul, M.; Dastidar, P. Coordination Polymers Derived from Non-Steroidal Anti-Inflammatory Drugs for Cell Imaging and Drug Delivery. *Chem. - A Eur. J.* **2016**, *22*, 988–998.

(94) Wu, Y.; Song, X.; Li, S.; Zhang, J.; Yang, X.; Shen, P.; Gao, L.; Wei, R.; Zhang, J.; Xiao, G. 3D-Monoclinic M–BTC MOF (M = Mn, Co, Ni) as Highly Efficient Catalysts for Chemical Fixation of CO2 into Cyclic Carbonates. *J. Ind. Eng. Chem.* **2018**, *58*, 296–303.

(95) Shi, W. J.; Du, L. Y.; Yang, H. Y.; Zhang, K.; Hou, L.; Wang, Y. Y. Ligand Configuration-Induced Manganese(II) Coordination Polymers: Syntheses, Crystal Structures, Sorption, and Magnetic Properties. *Inorg. Chem.* **2017**, *56*, 10090–10098.

(96) Mahmoudi, G.; Chowdhury, H.; Lofland, S. E.; Ghosh, B. K.; Kirillov, A. M. Two Manganese(II) Coordination Polymers Driven by (Iso)Nicotinoyl-Hydrazone Blocks and Pseudohalide Ancillary Ligands: Syntheses, Structural Features, and Magnetic Properties. *J. Coord. Chem.* **2017**, *70*, 1973–1983.

(97) Wang, X.; Liu, X.; Rong, H.; Song, Y.; Wen, H.; Liu, Q. Layered Manganese-Based Metal–Organic Framework as a High Capacity Electrode Material for Supercapacitors. *RSC Adv.* **2017**, *7*, 29611–29617.

(98) Du, Z. Y.; Zhang, L.; Wang, B. Y.; Liu, S. J.; Huang, B.; Liu, C. M.; Zhang, W. X. Two Magnetic Δ-Chain-Based Mn(Ii) and Co(Ii) Coordination Polymers with Mixed Carboxylate-Phosphinate and M3-OH- Bridges. *CrystEngComm* **2017**, *19*, 1052–1057.

(99) Chen, L. D.; Zheng, Y. Q.; Zhu, H. L. Manganese Oxides Derived from Mn(II)-

Based Metal–Organic Framework as Supercapacitor Electrode Materials. *J. Mater. Sci.* **2018**, *53*, 1346–1355.

(100) Ming, M.; Bai, N. A Rare 3D Chloro-Laced Mn(II) Metal-Organic Framework to Show Sensitive Probing Effect to Hg2+. *J. Solid State Chem.* **2017**, *254*, 9–13.

(101) Chen, X.; Peng, Y.; Han, X.; Liu, Y.; Lin, X.; Cui, Y. Sixteen Isostructural Phosphonate Metal-Organic Frameworks with Controlled Lewis Acidity and Chemical Stability for Asymmetric Catalysis. *Nat. Commun.* **2017**, *8*, 1–9.

(102) Pal, S.; Maiti, S.; Nayek, H. P. A Three-Dimensional (3D) Manganese (II) Coordination Polymer: Synthesis, Structure and Catalytic Activities. *Appl. Organomet. Chem.* **2018**, *32*, 1–9.

(103) Adpakpang, K.; Pratanpornlerd, W.; Ponchai, P.; Tranganphaibul, W.; Thongratkaew, S.; Faungnawakij, K.; Horike, S.; Siritanon, T.; Rujiwatra, A.; Ogawa, M.; et al. Unsaturated Mn(II)-Centered [Mn(BDC)]n Metal-Organic Framework with Strong Water Binding Ability and Its Potential for Dehydration of an Ethanol/Water Mixture. *Inorg. Chem.* **2018**, *57*, 13075–13078.

(104) Demakov, P. A.; Sapchenko, S. A.; Samsonenko, D. G.; Dybtsev, D. N.; Fedin, V. P. Coordination Polymers Based on Zinc(Ii) and Manganese(Ii) with 1,4-Cyclohexanedicarboxylic Acid. *Russ. Chem. Bull.* **2018**, *67*, 490–496.

(105) Davarcı, D. Design and Construction of One-Dimensional Coordination Polymers Based on the Dispiro-Dipyridyloxy-Cyclotriphosphazene Ligand. *Polyhedron* **2018**, *146*, 99–107.

(106) Bikas, R.; Farzaneh-Bonab, H.; Noshiranzadeh, N.; Aygün, M.; Emami, M.; Lis, T. Coumarin-Naphthohydrazone Ligand with a Rare Coordination Mode to Form Mn(II) and Co(II) 1-D Coordination Polymers: Synthesis, Characterization, and Crystal Structure. *J. Coord. Chem.* **2018**, *71*, 1127–1146.

(107) Fang, X. D.; Yang, L. B.; Dou, A. N.; Liu, Y. E.; Yao, J.; Xu, Q. Q.; Zhu, A. X. Synthesis, Crystal Structure and Photocatalytic Properties of a Mn (II) Metal-Organic Framework Based on a Thiophene-Functionalized Dicarboxylate Ligand. *Inorg. Chem. Commun.* **2018**, *96*, 124–127.

(108) Kang, H. X.; Fu, Y. Q.; Ju, F. Y.; Li, G. L.; Li, X. L.; Liu, G. Z. Syntheses, Structures, and Magnetic Properties of Two Mn(II) Coordination Polymers Based on 4-Fluorocinnamic Acid and 1,10-Phenanthroline. *Russ. J. Coord. Chem. Khimiya* **2018**, *44*, 340–346.

(109) Spirkl, S.; Grzywa, M.; Volkmer, D. Synthesis and Characterization of a Flexible Metal Organic Framework Generated from MnIII and the 4,4′-Bipyrazolate-Ligand. *Dalt. Trans.* **2018**, *47*, 8779–8786.

(110) Zou, G. D.; Gong, L. K.; Liu, L.; Zhang, Q.; Zhao, X. H. Two Low-Dimensional Transition Metal Coordination Polymers Constructed from Thiophene-2,5-dicarboxylic Acid and N/O-Donor Ligands: Syntheses, Structures and Magnetic Property. *Inorg. Chem. Commun.* **2019**, *99*, 140–144.

(111) Köse Yaman, P.; Erer, H.; Yeşilel, O. Z. Three Dimensional Manganese(II) Coordination Polymers Constructed from 2,2-Dimethylglutarate and Bis(Pyridyl) Type Ligands. *Polyhedron* **2019**, *171*, 317–322.

(112) Sundriyal, S.; Mishra, S.; Deep, A. Study of Manganese-1,4-Benzenedicarboxylate Metal Organic Framework Electrodes Based Solid State Symmetrical Supercapacitor. *Energy Procedia* **2019**, *158*, 5817–5824.

(113) Lan, W.; Hao, X.; Dou, Y.; Zhou, Z.; Yang, L.; Liu, H.; Li, D.; Dong, Y.; Kong, L.; Zhang, D. Various Structural Types of Cyanide-Bridged FeIII-MnIII Bimetallic Coordination Polymers (CPs) and Polynuclear Clusters Based-on a New Mer-Tricyanoiron(III)Building Block: Synthesis, Crystal Structures, and Magnetic Properties. *Polymers (Basel).* **2019**, *11*, 1585.

(114) Li, X. F.; Wang, X.; Wu, Y. Y.; Zhao, X. W.; Li, H. Y.; Li, Y. M. Four Coordination Polymers Based on 4'-(4-Carboxyphenyl)-2,2':6',2''-Terpyridine: Syntheses, Structures and Properties. *J. Solid State Chem.* **2019**, *269*, 118–124.

(115) Ge, Y.; Li, G.; Fu, D.; Liu, L.; Wu, B. Manganese(II) and Zinc(II) Coordination Polymers Based on 2-(5-Bromo-Pyridin-3-Yl)-1H-Imidazole-4,5-Dicarboxylic Acid: Synthesis, Structure and Properties. *J. Coord. Chem.* **2019**, *72*, 1820–1832.

(116) Meng, H. H.; Xia, X. L.; Lin, Z. G.; Song, X. Q. A New One Dimensional Mn(III)

Coordination Polymer Constructed by a Salicylamide Imine Multidentate Ligand: Structure, Magnetic and Luminescent Properties. *J. Inorg. Organomet. Polym. Mater.* **2019**, *29*, 1995–2002.

(117) Meng, L.; Zhao, L.; Guo, G.; Liu, X.; Liang, Z.; Xiu, J.; Zhou, X. Syntheses, Structures, and Characteristics of Three Metal Complexes Constructed Using Hexacarboxylic Acid. *Molecules* **2019**, *24*, 1–12.

(118) Morales-Morales, N.; Rodríguez-Olivas, M.; Téllez-López, A.; Martínez-Otero, D.; Morales-Luckie, R. A.; Sánchez-Mendieta, V. Syntheses and Crystal Structures of Mn(II), Ni(II) and Cu(II) Coordination Compounds Assembled by Maleato and Dimethyl-2,2′-Bipyridines. *J. Chem. Crystallogr.* **2019**, *49*, 8–20.

(119) Sharma, N.; Dhankhar, S. S.; Nagaraja, C. M. A Mn(II)-Porphyrin Based Metal-Organic Framework (MOF) for Visible-Light-Assisted Cycloaddition of Carbon Dioxide with Epoxides. *Microporous Mesoporous Mater.* **2019**, *280*, 372–378.

(120) Xiao, Q. Q.; Liu, D.; Wei, Y. L.; Cui, G. H. Two New Ternary Mn(II) Coordination Polymers by Regulation of Aromatic Carboxylate Ligands: Synthesis, Structures, Photocatalytic and Selective Ion-Sensing Properties. *J. Solid State Chem.* **2019**, *273*, 67–74.

(121) Xu, J.; Yang, Y.; Wang, Y.; Cao, J.; Chen, Z. Enhanced Electrochemical Properties of Manganese-Based Metal Organic Framework Materials for Supercapacitors. *J. Appl. Electrochem.* **2019**, *49*, 1091–1102.

(122) Dutta, B.; Akhtaruzzaman; Sato, H.; Akitsu, T.; Slawin, A. M. Z.; Kar, U.; Sinha, C.; Mir, M. H. Two Acetylenedicarboxylato-Bridged 4-Styrylpyridine Appended 1D Coordination Polymers: Synthesis, Structural Characterization and Variable Temperature Magnetism. *J. Chem. Sci.* **2020**, *132*, 1–6.

Chapter-II

Materials & Methods

CHAPTER-II

Materials & Methods

2.1. Materials:

Here in this study, we used 2,5-dihydroxy terephthalic acid and 4,4'-bipyridine linkers which were purchased from Singma-Aldrich. $Mn(OAc)_2.4H_2O$ was purchased from Finar India. All the solvents used in this study are- THF, MeOH, EtOH, DMF and DEF. THF was obtained from Merck India, MeOH from Sigma-Aldrich, EtOH from Merck India, DMF and DEF from TCI India. Nafion used during electrochemical analysis was purchased from Sigma-Aldrich India. All the chemicals and solvents in this study are used directly as received without further purification. The distilled water used during experiments were obtained from the Double Distillation Unit available in the lab.
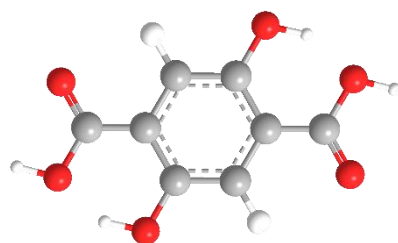
2,5-dihydroxyterephthalic acid

(DOT)
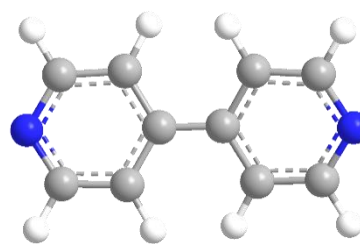
4,4'-bipyridine

(BPY)

2.2. Physical Methods:

2.2.1. Synthetic Methods: Among various commonly used synthetic methods like solvothermal synthesis, hydrothermal synthesis, sonochemical synthesis, microwave, etc. we have precisely focused on solvothermal synthetic method for constructing different coordination network.

2.2.1.1. Solvothermal method:

Solvothermal method is extensively used nowadays in synthesizing CPs and MOFs.[1] When only water is used as a solvent, it is called as hydrothermal method. The main advantage of solvothermal method is to enhance solubility and reactivity of reactants, faster crystallization and production of thermodynamically stable materials where other synthetic methods hardly does the same. In conventional reaction methods, crystal growth necessarily prefers higher solubility of reactants absence of which makes the crystallization process difficult. But in case of solvothermal synthesis, the diffusion takes place much faster compared to conventional method resulting in fast growing of crystals.[2] The popularly used reactor for solvothermal synthesis is Morey autoclave (ranges from 25-100 mL) (*figure 2.1*). Morey first designed this type of autoclave in 1913 where an autogenous pressure is created depending on the solvents, level of filling and temperature used.[3] In this method, solution of metal salt and organic linkers in appropriate organic solvents are transferred in autoclave. The autoclave must be capable to resist any acidic or alkali medium, high pressure and high temperature (>250 °C).[4,5] Depending upon the reaction condition, all the parameters such as temperature, reactant concentration and pH of solution can be varied resulting in formation of different coordination polymers. The reactions are done basically in a teflon lined stainless steel autoclave which can be heated up to very high temperature and generates autogenous pressure.[5] The volume occupied or the amount of fill have a high impact on the formation of the product. Laudise *et*. al. has described that when an autoclave is filled to 80 %, the solvent expands with the increasing temperature filling the volume up to 100 % before critical point leaving no space for formation of gaseous vapor which inhibits the autogenous pressure. He also described how the same phenomena disappears when an autoclave is filled 32-50 % only. Thus, it is always important to note that the volume fill should not preferably exceed 50 %.[6] However, for the external heating purpose, researcher uses different heating furnaces such as hot air oven, muffle furnace, etc.

Here in this study, we used a Nabertherm High Temperature Programmable Muffle Furnace (*figure 2.1(b)*) which is made of steel outer and insulted inner with high precision temperature controller. The rate of change of temperature can be set in terms of two functions- program 1 and program 2. In program 1, the temperature can be set to increase linearly with certain rate. Whereas in program 2, the temperature can be set which will remain constant for specific time.
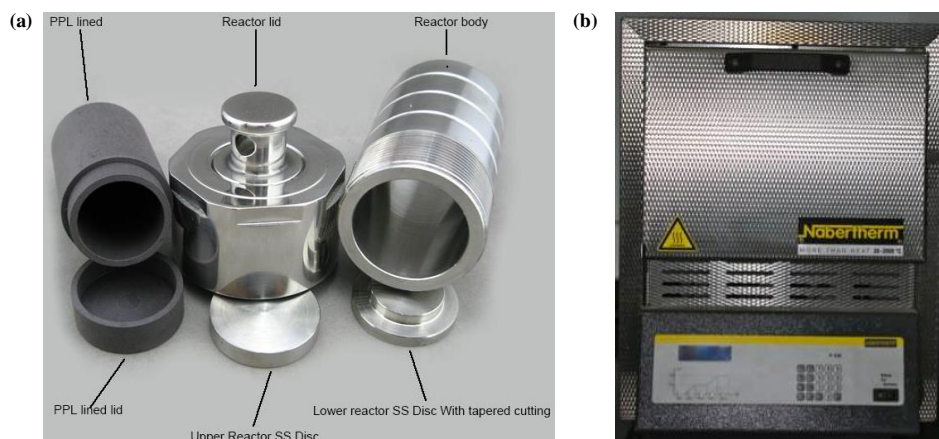
Figure 2.1: (a)Stainless Steel Autoclave with Teflon lined container & (b) Programmable muffle furnace.

2.2.2. Analytical Methods: For the analysis of the synthesized materials, we follow the different techniques as mentioned below:

2.2.2.1.   Single Crystal X-ray Diffraction (SC-XRD): It is the most powerful spectroscopic technique for characterizing molecules with simple as well as complex molecular structure. It gives complete insight of molecule from the bonding between atoms to the geometrical interactions. Each molecule contains periodic arrangement of atoms and each atom contains electrons which scatters X-rays at certain angles giving a well-defined diffraction pattern. The diffraction patterns are results of unique and inherent atomic arrangement in their respective crystal structure. Amorphous materials legs behind this race due to the absence of essential long-range atomic arrangement. The value of the order of diffraction patterns depends directly upon the ordered arrangement of the crystal. In other words, *more the degree of order, more ordered will be the diffraction and vice versa.*[7,8] Bragg's law describes the present crystal lattice parameters as given below[9]:

$$\lambda = 2\,d_{hkl}\sin\theta_{hkl}$$
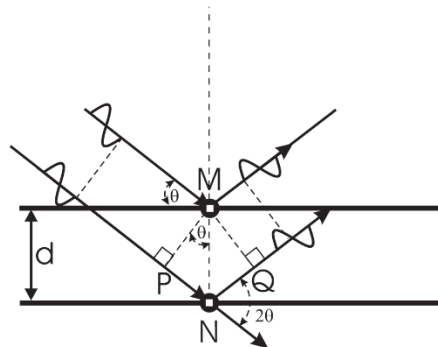
Figure 2.2: Diffraction pattern used for deriving Bragg's equation.

where λ is the wavelength of the incident X-ray beams, d_{hkl} is the interplanar distance between neighboring lattice planes with Miller indices *hkl* and θ_{hkl} is half the angle between the incident and diffracted beams. The interplanar distance d_{hkl} with the specific Miller indices for Monoclinic and Orthorhombic systems are calculated using the following equations:

Monoclinic:

$$\frac{1}{d_{hkl}} = \frac{1}{\sin^2\beta}\left(\frac{h^2}{a^2} + \frac{k^2\sin^2\beta}{b^2} + \frac{l^2}{c^2} - \frac{2hl\,\cos\beta}{ac}\right)$$

Orthorhombic:

$$\frac{1}{d_{hkl}} = \frac{h^2}{a^2} + \frac{k^2}{b^2} + \frac{l^2}{c^2}$$

where a, b, c are unit cell parameters.

As the incident X-rays are reflected by electrons present in atoms and the atoms of neighboring plans doesn't lie above each other, a more simplified Bragg's equation is necessary to obey the above-mentioned condition. A simplified form of Bragg's equation is given below[10]:

$$n\lambda = MN(\,2\sin\alpha\,\sin\theta\,)$$
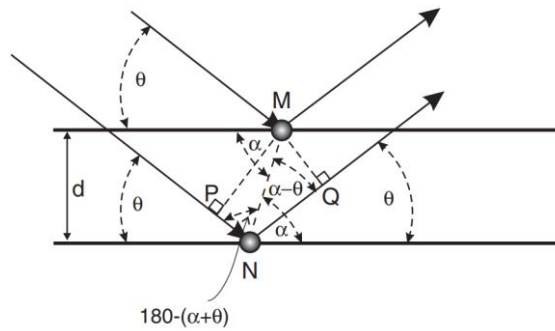
Figure 2.3: General case of position of atoms used for deriving Bragg's equation.

Apart from Bragg's law, structure factor (F) describes the scattering of X-ray by all the unit cells present throughout a whole crystal. The equation for deducing F for the jth atom with hkl^{th} reflection is:

$$F_{hkl} = \sum_{j=1}^{n} f_{j,\theta}\, exp[i2\pi(hx_j + ky_j + lz_j)]$$

Where $f_{j,\theta}$ is the atomic scattering factor.

For the determination of unit cell volume (V), the deduced equation for V is:

$$V = abc\, (1 - cos^2\alpha - cos^2\beta - cos^2\gamma + 2\cos\alpha\cos\beta\cos\gamma)^{1/2}$$

Here we use Rigaku SuperNova Single Crystal Diffractometer. The instrument consists of four components - a source to generate the incident X-ray beam, a goniometer for positioning the crystal, a detector for measuring the scattered beams and a controller for data refinement. The commonly used X-ray sources are Mo (Kα) and Cu (Kα) with wavelengths 0.71 Å and 1.56 Å respectively. Crystal data are recorded by loading the respective single crystal in a tame sample holder and placing it in the goniometer. The goniometer typically orients the crystals by moving in three different angles- χ, ϕ and ω for appropriate diffraction. The X-rays are scattered by the crystal sample and the detector CCD detects the diffracted beam producing some meaningful diffraction pattern.
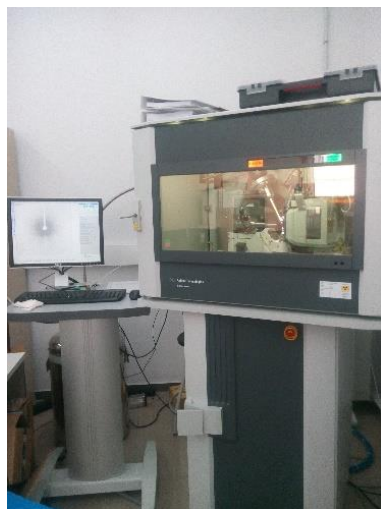
Figure 2.4: Image of Rigaku SuperNova SC-XRD instrument.

Finally, the data processing software CysAlis Pro concludes the results obtained starting from positioning of the crystals to the scattered beams, refining every minimal amount of data. Temperature factors makes a great difference in the data sets obtained from single crystal diffraction. In ambient temperature, the thermal motion of electrons prevents their scattering contribution resulting in diminishing the diffraction intensity. But to overcome that issue, one can collect the data at very low temperature using N_2 cryostat which minimizes the thermal motion of electrons resulting in better diffraction intensity.

2.2.2.2.   Powder X-ray Diffraction (P-XRD): This technique is based on the same theory as the SC-XRD. Here in this technique, phase identification, sample purity, crystallite size as well as morphology of bulk samples are determined corresponding to the data obtained from SC-XRD. The comparison of experimental XRD pattern with the pattern obtained after simulation or from different sources gives an idea regarding the phase and purity of the sample.[11,12] In this case, presence of extra peaks or difference in intensities must be addressed with clear justification of any changes in the patterns from the reference. But phase identification of several systems such Au and Ag nanoparticles becomes infuriating due to indistinguishable diffraction patterns.[11] In such cases, further confirmation is necessary by supporting with XAFS, HR-TEM, SAXS, etc.[11,12]

Figure 2.5: Image of Panalytical X'Pert Pro P-XRD instrument.

For PXRD analysis, we used Panalytical X'Pert Pro and Rigaku TTRX III X-ray diffractometers. The instruments were sourced with Cu Kα tube having wavelength of 1.56 Å.

2.2.2.3.   Fourier Transform Infrared Spectroscopy (FT-IR): FT-IR spectroscopy is used to determine the functional groups present in a molecule. It is a spectroscopic method where absorption of light causes molecular vibration. When a molecule is provided with a certain amount of energy which matches the vibrational frequency, it triggers the vibration of bonds present in the molecule. It is mainly based on the vibration of chemical bonds in mid infrared region (400 to 4000 cm^{-1}) only. This region is divided in two parts- fingerprint region which lies in 400-1600 cm^{-1} and the functional groups region which lies in 1600-4000 cm^{-1}. The vibrational spectra are determined using Hooke's equation[13–15]:

$$\bar{\upsilon} = \frac{1}{2\pi c}\sqrt{\frac{k}{\mu}} \ cm^{-1}$$

where $\bar{\upsilon}$ is wavenumber (cm^{-1}), c is speed of light (cm sec^{-1}), k is the force constant (dyne cm^{-1}) and μ is the reduced mass of atoms (g).

There are different types of vibrational modes are possible. Two commonly known vibrational modes are- stretching and bending. In stretching mode, the interatomic distance and bond length changes and in bending mode, the bond angle changes. Again, stretching mode is classified in two types- symmetric and anti-symmetric stretching. In symmetric stretching mode, the atoms move to a distance to or from the central atom. However, in anti-symmetric stretching mode, one of the atoms moves

towards the central atom and the other moves away from the central atom. In case of bending mode, it is classified into four types- rocking, scissoring, wagging and twisting. In rocking, the two atoms moves clockwise or anticlockwise; in scissoring, the two atoms moves towards or away from the central atom simultaneously; in wagging, the two atoms moves in V direction back and forth and in twisting, one of the atom moves backward where as another moves forward (*figure 2.6*).[16]
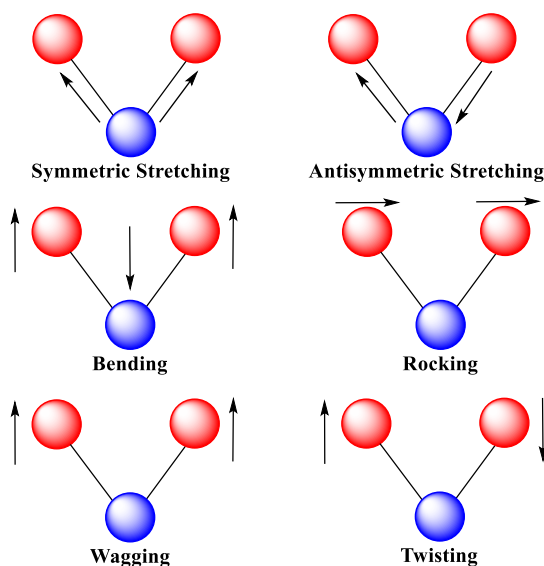
Figure 2.6: Different modes of vibration in IR spectroscopy.

In our lab, Bruker Alpha FT-IR Spectrophotometer (*figure 2.7*) is available capable of performing both liquid state as well as solid state sample measurement. The instrument consists of the following components- light source, monochromator, sample holder and the detector. The light source is basically a Nernst filament or a Globar filament which are red or white heated before analysis. The light produces are then passed further towards the sample with the help of silver layered mirror and passes through the monochromator producing desired frequency of light. The samples are held in metal sample holder (in case of solid samples) by preparing a thin film of KBr and the sample and the liquid samples are held in an ATR crystal surface. The detector then detects by sensing heating effect due to radiation or by photoconductivity.
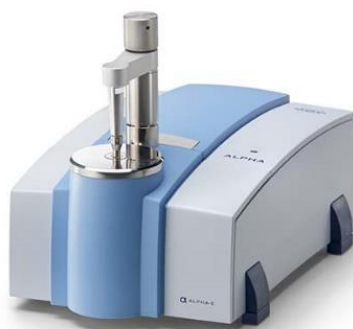
Figure 2.7: Bruker Alpha FT-IR Spectrophotometer.

2.2.2.4. **Thermogravimetric Analyser (TGA):** TGA is used to monitor the change in mass of a sample as a function of time or temperature *via* a controlled heating system. Any kind of changes such as decomposition, oxidation-reduction, dehydration, volatilisation or chemisorption involving change in weight are detectable using TGA. TGA is a combination of a microbalance, programmable temperature controller and a PC for data acquisition (*figure 2.8(a)*).[17–19] The balance is connected to sensor which detects the deviation from a null point and measures the change in mass. They are sensitive to an order of 10^{-6} g. Samples are placed in a pan (platinum/aluminium/ceramics) and suspended from the microbalance down to a furnace where a highly controlled heating environment is maintained. The balance mechanism present inside the instrument is protected from causing damage due to high temperature by using a baffle and flowing inert gas.
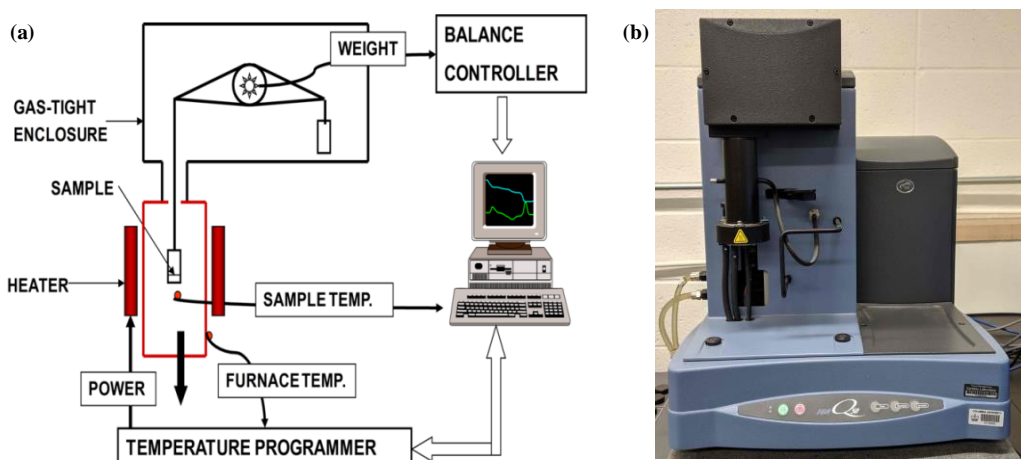
Figure 2.8: (a) Schematic diagram of a TGA analyser & (b) TA Instrument's Q50 TGA analyser.

The measurement data can generally be plotted in two ways- thermogravimetric (TG) curve or derivative thermogravimetric (DTG) curve. In the first one, the change in mass/weight *vs.* time or temperature is plotted and in the second one, the rate of change in mass/weight *vs.* time or temperature is plotted.[18,19] Here we used TA Instrument's Q50 TGA analyser (*figure 2.8(b)*) for TG measurements. During analysis, we programmed the system to heat at a rate of 20 °C min⁻¹ up to 600 °C. The N_2 gas flow was maintained at 60 mL min⁻¹ inside the heating furnace and 40 mL min⁻¹ inside the balance chamber. Two platinum pans were used- one as a reference and other one to place the sample. The final obtained results were plotted both as TG and DTG curve format.

2.2.2.5. **Surface Area Analyzer:** Surface area measurement is the most important physical property of porous materials. Therefore, accuracy in determining the exact surface is much needed. The surface area and pore size distribution can be analyzed using small angle X-ray and neutron scattering (SAXS and SANS), mercury porosimetry, electron microscopy (scanning and transmission), thermoporometry, adsorption isotherms and others. But due to certain limitations and cost efficiency in each of the above-mentioned techniques, calculation of surface area using adsorption isotherm is commonly being used by researchers.[20] The commonly used method for surface area analysis is BET method which is closely related to the Langmuir method. In Langmuir method, the formation of monolayer is considered where the adsorbate molecules form a layer over the surface binding closely to the solid surface. Whereas in BET method, the formation of multiple layers is considered where other layers get formed over the first adsorbate layer on solid surface. The multilayer adsorption takes place only when the temperature is below the critical temperature of the adsorbent.[21–23] The BET equation for multilayer adsorption is given as [22,24,25]:

$$\frac{P/P_0}{V(1 - P/P_0)} = \frac{1}{V_m C} + \frac{C - 1}{V_m C}(P/P_0)$$

where V= amount of gas adsorbed, V_m = monolayer capacity of adsorbate, P = pressure, P_0 = saturation pressure of adsorbate & C = BET constant.

For characterization and presentation of BET isotherms, IUPAC in 1985[26] recommended six different types of plots for physical adsorption. Later in 2015[27], IUPAC updated total eight different types of plots considering the physisorption isotherms and hysteresis loops associated with them. They are as follows:
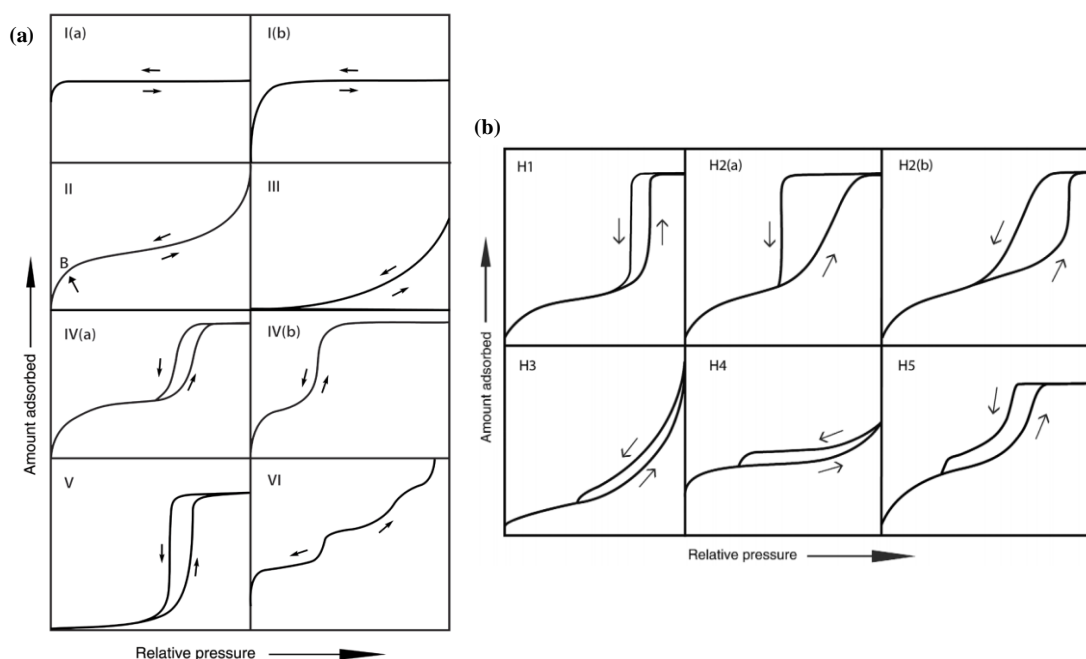
Figure 2.9: Classifications of (a) physisorption isotherms & (b) hysteresis loops.

i. Type-I: It is obtained typically for microporous materials with pore size with smaller external surface. Microporous materials with narrow micropores ($<\sim$ 1 nm) give type I(a) isotherms whereas materials with broad micropores and including narrow mesopores ($< \sim$ 2.5 nm) gives type I(b) isotherms.

ii. Type-II: This kind plots are obtained for nonporous or microporous materials. The point B on the curve (*figure 2.9(a)*) indicates the completion of monolayer formation and beginning of multilayer formation.

iii. Type-III: It is obtained when there is weak interaction between the adsorbent and adsorbate.

iv. Type-IV: These curves are obtained in case of mesoporous materials. Type IV(a) curve is obtained when pore width exceeds critical width and is accompanied with capillary condensation accompanied giving hysteresis loop. Again, type IV(b) occurs in presence of mesopores with smaller pore width.

v. Type-V: This shape is similar to type III at lower P/P_0 range and are obtained due to weak adsorbent–adsorbate interactions. At higher relative

pressure, hysteresis can be observed, and molecular clustering occurs simultaneously with pore filling.

vi.   Type VI: These isotherm curves are obtained for multilayer adsorption in materials having highly uniform nonporous surfaces. Depending on the material, gas and temperature, the curves take step-by-step increment.

Physisorption isotherms shows hysteresis loops during multilayer adsorption which causes due to occurrence of capillary condensation and takes different shapes as shown in *figure 2.9(b)*. These various shapes are associated with different factor affecting the isotherms are described below:

i.   Type H1: This kind of loops are observed when the materials exhibit narrow range of uniform mesopores.

ii.   Type H2: It is observed in materials having complex pore structure. H2(a) is observed when there is pore-blocking/percolation in narrow pore necks or cavitation-induced evaporation. However, H2(b) is observed when there is pore blocking with large neck width.

iii.   Type H3: These curves are obtained in presence of non-rigid aggregates particles and/or incomplete filling of macropores.

iv.   Type H4: These curves indicates the aggregation of crystals in materials such as zeolites, micro-mesoporous carbons, etc.

v.   Type H5: They are rarely seen in case of open and partially blocked mesopores.

Here in this study, we used Quantachrome NovaTouch LX Surface Area Analyzer (*figure 2.10*) to perform all adsorption-desorption isotherms. Prior to experiment, all the samples are degassed in Schlenk line 12 h and then further evacuation was performed in degassing chamber present in the instrument. The liquid N_2 used during analysis were purchased from Ninamma Industries, Singtam, Sikkim, India. All the analysis were performed in the P/P_0 range 0.001 to 0.99 spreading into 20 points.

Figure 2.10: Quantachrome NovaTouch surface area analyzer.

2.2.2.6. **Superconducting Quantum Interference Device (SQUID):** Among the different available techniques such as induction coils, flux gate magnetometers, magnetoresistive and Hall effect magnetometers, magneto-optical magnetometers, and optically pumped magnetometers, etc., SQUID magnetometer is used the most to measure any physical quantity that can be converted to a flux, for example, magnetic field, magnetic field gradient, current, voltage, displacement, and magnetic susceptibility. Magnetic properties of samples in absolute units. It can detect even very small magnetic fields present/induced in any sample.[28,29] It is based on the principle of Josephson effect where the SQUID loop is interrupted by one or more Josephson junctions.[30] The SQUID loop is constrained with inductance L, current (*figure 2.11*)
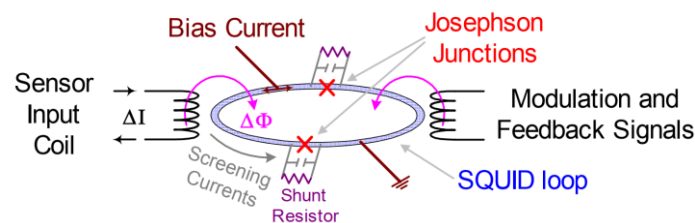
Figure 2.11: SQUID loop with Josephson's junctions.

and operating temperature. When the electric current density of the sample and superconductor goes through weak contact, a phase change (δ) takes place. The derivative of δ with time is correlated with voltage across those weak contacts using liquid helium. With the change in external magnetic flux, the voltage changes

periodically and the change in voltage helps in determining the magnetic flux in the SQUID loop.[31]

$$I = I_C \sin \delta$$

Where I= measuring current, I_c= critical current and δ= phase change of macroscopic wave functions.

The Inductive coupling of magnetic flux with the SQUID loop produces a screening current $I_{loop} = \Phi_{loop}/L_{loop}$ which effectively increase or decrease the critical current I_c, as per the direction of the induced flux.[28] One important point to note that SQUID can detect magnetic flux density B times the area A of the SQUID loop.[32]

$$\text{i.e. } \Phi = \int B . dA$$

Since a superconductor in used here, the instrument is maintained at a temperature below 4 K using liquid helium. There are two different SQUID operations are available- Radio Frequency (RF) SQUID and Direct Current (DC) SQUID. A RF SQUID is equipped with only one Josephson junction whereas DC SQUID is equipped with two Josephson junctions.[29,30,32] Here in this study, we performed DC SQUID using Quantum Design Evercool SQUID-VSM (*figure 2.12*) in temperature range of 2-300 K and 0 to ±70 kOe magnetic field. Both the ZFC and FC measurements were taken in the range 2-300 K. The results obtained were plotted as M *vs.* T and M *vs.* H which were later be converted/plotted in different units for convenience.

Figure 2.12: Quantum Design Evercool SQUID-VSM.

2.2.2.7. **Cyclic Voltammetry (CV):** This is a powerful electrochemical technique to measure and investigate the reduction and oxidation processes involving transfer of electrons.[33,34] The synthesis and characterization of many organic polymers and inorganic materials, metal-ligand interaction behavior, calculation of HOMO & LUMO of semiconductors, electroactivity of materials, etc. can be done with the help of CV measurements.[34] In cyclic voltammetry experiment, we use three electrodes-reference electrode, auxiliary/counter electrode and working electrode. The potential in the reference electrode remains constant due to which it can be taken as a standard whereas the auxiliary electrode serves a source of electrons to complete the circuit. However, the working electrode acts a surface where the electrochemical event takes place. All the three electrodes are dipped in an electrolyte solution for transfer of electrons throughout the cell *figure 2.13(a)*.
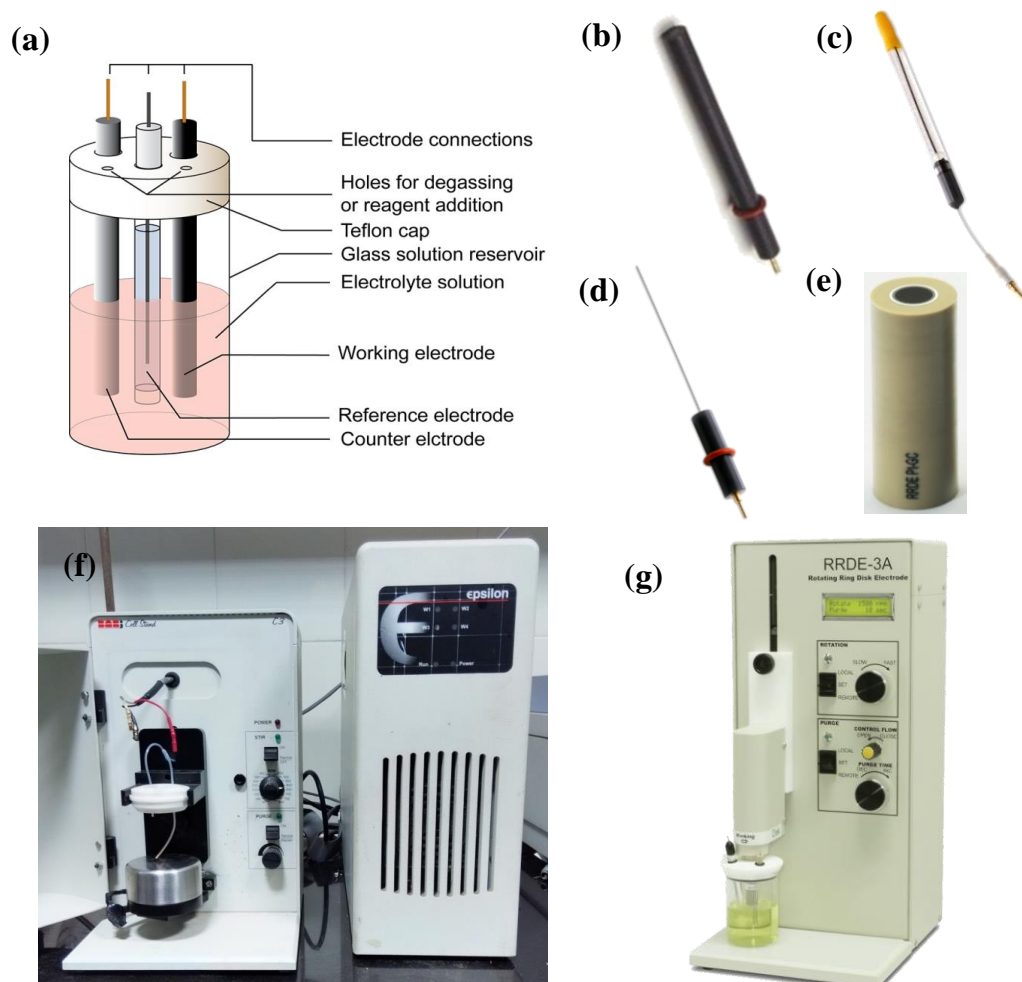
Figure 2.13: (a) Schematic diagram of an electrochemical cell, (b) GC electrode, (c) Ag/AgCl electrode, (d) Pt wire electrode, (e) ring disk electrode (GC disk + Pt ring), (f) BASi Epsilon Electrochemical Analyser & (g) RRDE-3A instrument.

When a potential is applied, the potential difference occurring between auxiliary and working electrodes drives the electron flow causing an oxidation or reduction of the electro active species:

$$A^+ + e^- \rightleftarrows B$$
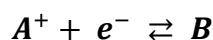
The relationship between the potential of electrochemical cell (E) and standard potential of electroactive species (E^0) is given by Nernst equation[34]:

$$E = E^0 + \frac{RT}{nF} \ln \frac{Oxd}{Red}$$

Or, $$E = E^0 + 2.3026 \frac{RT}{nF} \log_{10} \frac{Oxd}{Red}$$

where, F = Faraday's constant, R = Gas constant, n = no. of electrons & T = temperature.

When a cyclic voltammetry is performed, the obtained curve is called as cyclic voltammogram. It can be represented in two different conventions- US and IUPAC where the applied potential *vs.* resulting current is plotted (*figure 2.14(a)*). From *figure 2.14(b)*, we can have an idea about how the peak current (i_p) changes with changing potential. The peak current is also dependent on the scan rate which can be described with the help of Randles-Sevcik equation.[34]:

$$i_p = 0.446nFAC^0 \left(\frac{nFvD_o}{RT}\right)^{1/2}$$

where A = electrode surface area (cm^2), C^0= conc. of analyte in bulk (mol cm^{-3}), v= scan rate (V sec^{-1}) and D_o= diffusion coefficient of oxidised analyte (cm^2 sec^{-1}).
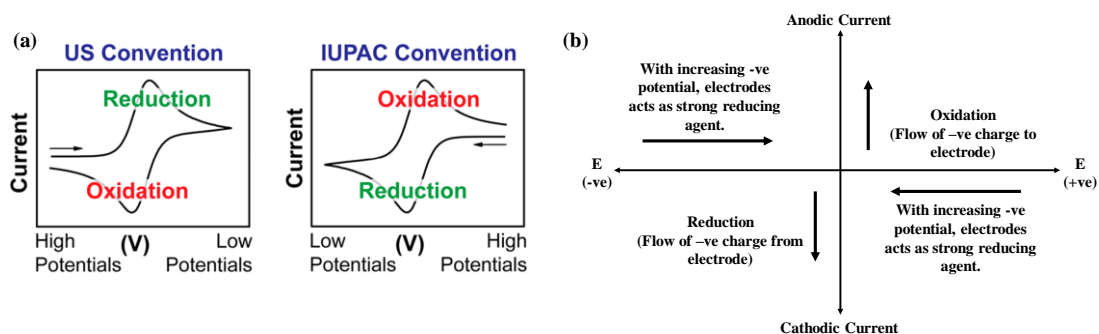
Figure 2.14: (a) US & IUPAC convention for CV curve & (b) current *vs.* potential diagram during CV analysis.

Apart from CV experiments, another important experimental tool is rotating ring disk electrode (RRDE) measurements. This technique is commonly used for the detection of intermediates formed during oxygen reduction reactions (ORR) such as H_2O_2. In RRDE, the electrodes used contains two portions: one is disk electrode present at the

centre and the other is a ring electrode surrounding the disk separated by a thin insulating barrier. The whole analysis is done under a controlled rotation rate of the electrode which drags the electrolyte solution towards the surface of electrode and increases the rate of diffusion. V. G. Levich on his book "*Physicochemical Hydrodynamics*" explained the effect of mass transport to the electrode surface. Later, V. G. Levich and Jaroslav Koutecký developed the famous Koutecký-Levich (K-L) equation which includes the contribution of mass transport to electrode surface and rate of electrochemical half-reaction[35–37].

$$\frac{1}{i_D} = \frac{1}{i_K} + \frac{1}{I_D}$$

Where i_D = disk current, i_K = kinetic current density (A cm^{-2}) & I_D = limiting current density of oxidant reduction (A cm^{-2}).

Here

$$i_K = i^0 exp\left(-\frac{(1-\alpha)nF(E-E^{eq})}{RT}\right)$$

$$I_D = 0.62nFD_0^{2/3}v^{-1/6}\omega^{1/2}C_O^0$$

Where i^0 = exchange current density (A cm^{-2}), α = electron transfer coefficient in rate determining step, E = electrode potential (V), E^{eq} = equilibrium electrode potential (V), R = gas constant (8.314 J mol^{-1} K^{-1}), T= absolute temperature (K), n = no. of electrons transferred, F = Faraday's constant (96487 A sec mol^{-1}), D_O = diffucion coefficient of oxidant (cm^2 sec^{-1}), v = kinetic viscosity of solution (cm^2 sec^{-1}), ω = angular rotation rate (rad sec^{-1}) and C_O^0 = bulk conc. Of oxidant (mol cm^{-3}).

In case of ω in rpm $\left(rad\ sec^{-1} = \frac{2\pi}{60}rpm\right)$,

$$I_{d,O} = 0.201nFD_0^{2/3}v^{-1/6}\omega^{1/2}C_O^0$$

Here in this study, we used BASi Epsilon Electrochemical Analyser (*figure 2.13(f)*) and RRDE-3A instrument (*figure 2.13(g)*) for performing CV and RRDE measurements. The CV was in different voltage window, firstly in N$_2$ saturated electrolyte solution and then again in O$_2$ saturated solution. The RRDE measurements performed by setting rotation speeds of 400, 625, 900, 1225, 1600, 2025 and 2500 rpm.

2.2.2.8. **Carbon, Hydrogen & Nitrogen (CHN) Analyzer:** CHN analyzer is commonly used to measure the amount of carbon, hydrogen & nitrogen in samples.

Some of the CHN instruments also measures the amount of oxygen and sulphur which are known as CHNS/O and CHNS analyzer. It is based on the principle of Pregl-Dumas method where the sample undergoes combustion (~1000 °C) in an oxygen-rich environment. The combustion process converts the carbon into CO_2, hydrogen to H_2O, nitrogen to N_2/nitrogen oxide and sulphur to SO_2 (*figure 2.15(a)*). The gases produced during combustion are carried out over heated high purity copper by an inert gas such as helium to convert oxides of nitrogen to N_2. Finally, the gases are diverted to the detection unit through an absorbent trap to trap CO_2, H_2O, N_2 and SO_2 only. For detection of the final products, typically GC or infrared and thermal conductivity cells are used[38]. Here in this study, we performed the CHN analysis using Eurovector EA 3000 CHN Analyser (*figure 2.15(b)*).
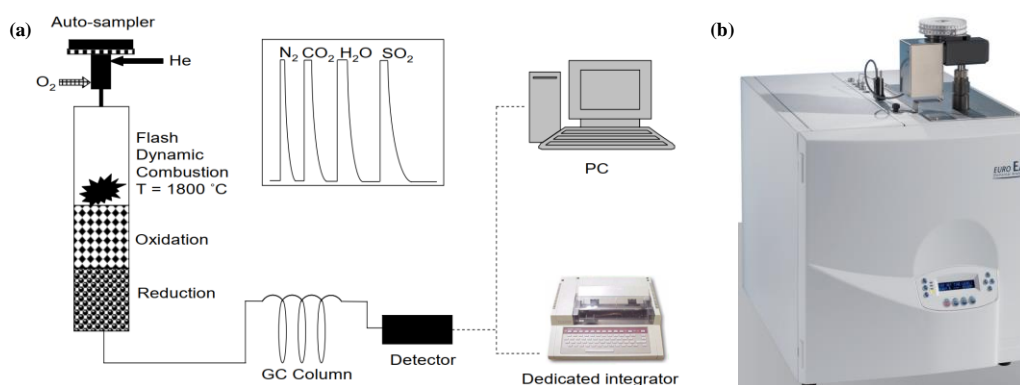
Figure 2.15: (a) Schematic diagram of CHN Analyser & (b) Eurovector EA 3000 CHN Analyser.

References:

(1) Zhao, Y.; Li, K.; Li, J. Solvothermal Synthesis of Multifunctional Coordination Polymers. *Zeitschrift für Naturforsch. B* **2010**, *65*, 976–998.

(2) Demazeau, G. Solvothermal Reactions: An Original Route for the Synthesis of Novel Materials. *J. Mater. Sci.* **2008**, *43*, 2104–2114.

(3) Morey, G. W.; Niggli, P. The Hydrothermal Formation of Silicates, A Review. *J. Am. Chem. Soc.* **1913**, *35*, 1086–1130.

(4) Feng, S.-H.; Li, G.-H. Hydrothermal and Solvothermal Syntheses. In *Modern Inorganic Synthetic Chemistry, Second Edition*; Elsevier, **2017**; 73–104.

(5) Loera-Serna, S.; Ortiz, E. Catalytic Applications of Metal-Organic Frameworks. In *Advanced Catalytic Materials - Photocatalysis and Other Current Trends*; Norena, L. E., Wang, J.-A., Eds.; InTech, **2016**; 95–122.

(6) Laudise, R. A. Hydrothermal Synthesis of Crystals. *Chem. Eng. News Eng. News* **1987**, *65*, 30–43.

(7) Bond, A. D. Single-Crystal X-Ray Diffraction. In *Analytical Techniques in the Pharmaceutical Sciences*; Mullertz, A., Perrie, Y., Rades, T., Eds.; Springer-Verlag New York, **2016**; 315–337.

(8) To, P. S. *Chapter 7 : Basics of X-Ray Diffraction*; **1999**.

(9) Dinnebier, R. E.; Billinge, S. J. L. Chapter 1. Principles of Powder Diffraction. In *Powder Diffraction: Theory and Practice*; Dinnebier, R. E., Billinge, S. J. L., Eds.; Royal Society of Chemistry: Cambridge, **2008**, *20*, 1–19.

(10) Bunaciu, A. A.; Udriştioiu, E. gabriela; Aboul-Enein, H. Y. X-Ray Diffraction: Instrumentation and Applications. *Crit. Rev. Anal. Chem.* **2015**, *45*, 289–299.

(11) Holder, C. F.; Schaak, R. E. Tutorial on Powder X-Ray Diffraction for Characterizing Nanoscale Materials. *ACS Nano.* **2019**, *13*, 7359–7365.

(12) Thakral, N. K.; Zanon, R. L.; Kelly, R. C.; Thakral, S. Applications of Powder X-Ray Diffraction in Small Molecule Pharmaceuticals: Achievements and Aspirations. *J. Pharm. Sci.* **2018**, *107*, 2969–2982.

(13)   J. Michael Hollas. *Modern Spectroscopy*; **2004**.

(14)   Nakamoto, K. Theory of Normal Vibrations. *Infrared Raman Spectra Inorg. Coord. Compd.* **2009**, 1–147.

(15)   Ismail, A. A.; van de Voort, F. R.; Sedman, J. Chapter 4 Fourier Transform Infrared Spectroscopy: Principles and Applications. *Tech. Instrum. Anal. Chem.* **1997**, *18*, 93–139.

(16)   Javadzadeh, Y.; Hamedeyaz, S. Floating Drug Delivery Systems for Eradication of Helicobacter Pylori in Treatment of Peptic Ulcer Disease. In *Trends in Helicobacter pylori Infection*; InTech, **2014**, *1*, 13.

(17)   Sharp, J. H.; Manley, T. R. Thermal Analysis. *Proc. Soc. Anal. Chem.* **1971**, *8*, 112.

(18)   Coats, A. W.; Redfern, J. P. Thermogravimetric Analysis. A Review. *Analyst* **1963**, *88*, 906–924.

(19)   Simon, J. *Introduction to Thermal Analysis Techniques and Applications*; Brown, M. E., Ed.; Kluwer Academic Publishers, **2001**, *1*.

(20)   Lowell, S.; Shields, J. E.; Thomas, M. A.; Thommes, M. *Characterization of Porous Solids and Powders: Surface Area, Pore Size and Density*; Professor Brian Scarlett, Ed.; Particle Technology Series; Springer Netherlands: Dordrecht, **2004**, *16*.

(21)   Sinha, P.; Datar, A.; Jeong, C.; Deng, X.; Chung, Y. G.; Lin, L.-C. Surface Area Determination of Porous Materials Using the Brunauer–Emmett–Teller (BET) Method: Limitations and Improvements. *J. Phys. Chem. C* **2019**, *123*, 20195–20209.

(22)   Ambroz, F.; Macdonald, T. J.; Martis, V.; Parkin, I. P. Evaluation of the BET Theory for the Characterization of Meso and Microporous MOFs. *Small Methods* **2018**, *2*, 1-17.

(23)   Walton, K. S.; Snurr, R. Q. Applicability of the BET Method for Determining Surface Areas of Microporous Metal-Organic Frameworks. *J. Am. Chem. Soc.* **2007**, *129*, 8552–8556.

(24) Brunauer, S.; Emmett, P. H.; Teller, E. Adsorption of Gases in Multimolecular Layers. *J. Am. Chem. Soc.* **1938**, *60*, 309–319.

(25) Dollimore, D.; Spooner, P.; Turner, A. The Bet Method of Analysis of Gas Adsorption Data and Its Relevance to the Calculation of Surface Areas. *Surf. Technol.* **1976**, *4*, 121–160.

(26) Sing, K. S. W.; Everett, D. H.; Haul, R. A. W.; Moscou, L.; Pierotti, R. A.; Rouquerol, J.; Seimieniewska, T. Reporting Physisorption Data For Gas/Solid Systems with Special Reference to the Determination of Surface Area and Porosity; *Pure & Appl. Chem.* **1985,** 57.

(27) Thommes, M.; Kaneko, K.; Neimark, A. V.; Olivier, J. P.; Rodriguez-Reinoso, F.; Rouquerol, J.; Sing, K. S. W. Physisorption of Gases, with Special Reference to the Evaluation of Surface Area and Pore Size Distribution (IUPAC Technical Report). *Pure Appl. Chem.* **2015**, *87*, 1051–1069.

(28) Fagaly, R. L. Superconducting Quantum Interference Device Instruments and Applications. *Rev. Sci. Instrum.* **2006**, *77*, 1–45.

(29) Clarke, J. Principles and Applications of SQUIDs. *Proc. IEEE* **1989**, *77*, 1208–1223.

(30) Clarke, J.; Braginski, A. I. *The SQUID Handbook: Fundamentals and Technology of SQUIDS and SQUID Systems*; Wiley-VCH Verlag Gmb & Co. KGaA, **2006**, 1.

(31) Fuller, M.; Goree, W. S.; Goodman, W. L. An Introduction to the Use of SQUID Magnetometers in Biomagnetism. In *Magnetite Biomineralization and Magnetoreception in Organisms*; Plenum Press, New York, **1985**, 103–151.

(32) Buchner, M.; Höfler, K.; Henne, B.; Ney, V.; Ney, A. Tutorial: Basic Principles, Limits of Detection, and Pitfalls of Highly Sensitive SQUID Magnetometry for Nanomagnetism and Spintronics. *J. Appl. Phys.* **2018**, *124* , 1–13.

(33) Chooto, P. Cyclic Voltammetry and Its Applications. In *Voltammetry*; IntechOpen, **2019**, 1–14.

(34) Elgrishi, N.; Rountree, K. J.; McCarthy, B. D.; Rountree, E. S.; Eisenhart, T. T.; Dempsey, J. L. A Practical Beginner's Guide to Cyclic Voltammetry. *J. Chem. Educ.* **2018**, *95*, 197–206.

(35) Jia, Z.; Yin, G.; Zhang, J. Rotating Ring-Disk Electrode Method. In *Rotating Electrode Methods and Oxygen Reduction Electrocatalysts*; Elsevier, **2014**, 199–229.

(36) Dalton, F. Historical Origins of the Rotating Ring-Disk Electrode. *Interface Mag.* **2016**, *25*, 50–59.

(37) Zhou, R.; Zheng, Y.; Jaroniec, M.; Qiao, S. Z. Determination of the Electron Transfer Number for the Oxygen Reduction Reaction: From Theory to Experiment. *ACS Catal.* **2016**, *6*, 4720–4728.

(38) Thompson, M. CHNS Elemental Analysers. *Anal. Methods Comm. Tech. Briefs* **2008**, 29.

Chapter III

Synthesis & Characterization

Chapter III

Synthesis & Characterization

3.1. Synthesis of Mn-based Coordination Polymers:

3.1.1. Synthesis of Mn$_2$(DOT)(H$_2$O)$_2$[Mn-SKU-1]:

General Reaction:

$$Mn(OAc)_2.4H_2O \ + \ \underset{\substack{\textbf{Dihydroxyterepthalic acid} \\ \textbf{(DOT)}}}{\text{[DOT structure]}} \ \xrightarrow[150\ ^oC,\ 38\ h]{THF:H_2O=\ 7:3} \ \underset{\textbf{Mn-SKU-1}}{C_8H_6Mn_2O_8}$$
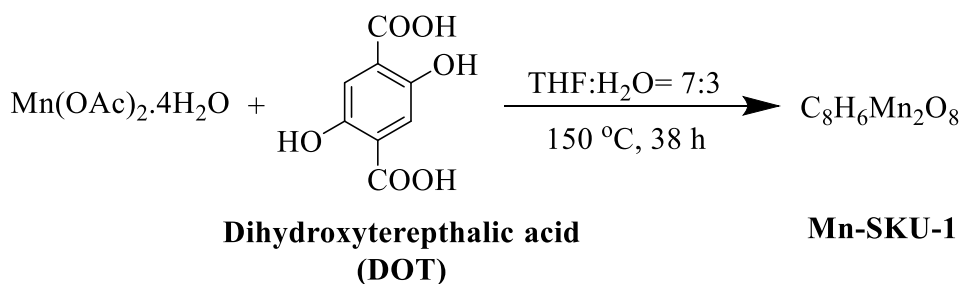
In a 15 mL vial, 0.244 g of Mn(NO$_3$)$_2$·4H$_2$O (1.0 mmol) was dissolved in 5 mL distilled water and in another vial, about 0.099 g 2,5-dihydroxyterephthalic acid (0.5 mmol) was dissolved in 10 mL THF. The solutions were sonicated for 2 minutes and then transferred to a 20 mL teflon-lined stainless-steel autoclave. The autoclave was then placed inside a programmable muffle furnace programmed to heat at 0.63 ^{o}C per min up to 150 ^{o}C (program "1") and then set to heat constantly at 150 ^{o}C for 34 h (program "2"). After completion of reaction, the autoclave was naturally cooled to room temperature. Fine brown colored octahedral shaped single crystals were obtained as the product. The obtained crystals were washed with THF, H$_2$O and ethanol several times. The product was then dried overnight in vacuum at 120 ^{o}C and stored for further analysis. Yield: 0.065 g. IR (KBr, cm^{-1}): 3400, 1650, 1386. XRD 2θ (°): 11.7, 15.07, 20, 25.88, 28.23, 32.81, 33.62. Anal. Calcd. for C$_8$H$_6$Mn$_2$O$_8$: C, 28.26; H, 1.78; Found: C, 28.67; H, 1.88.

3.1.2. Synthesis of Mn(H₂DOT)(BPY) [Mn-SKU-2]:

General Reaction:

$$Mn(OAc)_2 \cdot 4H_2O \ + \ \underset{\substack{\text{Dihydroxyterepthalic} \\ \text{acid (DOT)}}}{\text{DOT}} \ + \ \underset{\substack{\text{4,4' bipyridine} \\ \text{(BPY)}}}{\text{BPY}} \ \xrightarrow[150\,^oC,\,38\,h]{THF:H_2O=\ 7:3} \ \underset{\text{Mn-SKU-2}}{C_{18}H_{12}MnN_2O_6}$$
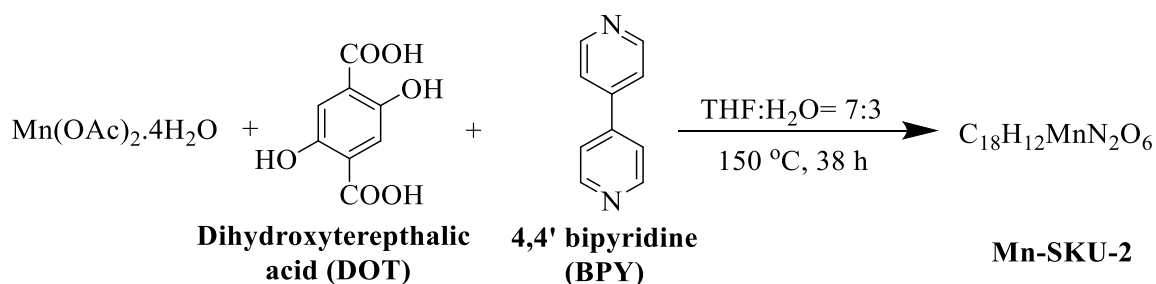
In a 15 mL vial, 0.244 g of Mn(NO₃)₂·4H₂O (1.0 mmol) was dissolved in 5 mL distilled water. In two separate vials, 0.099 g 2,5-dihydroxyterephthalic acid (0.5 mmol) and 0.078 g 4,4'-bipyridine (0.5 mmol) were dissolved in 5 mL THF each. All the solutions were sonicated for 2 min and then transferred to a 20 mL teflon-lined stainless-steel autoclave. The autoclave was then placed inside a programmable muffle furnace programmed to heat at 0.63 ^oC per min up to 150 ^oC (program "1") and then set to heat constantly at 150 ^oC for 34 h (program "2"). Then the autoclave was allowed to cool at room temperature. Fine brown colored octahedral shaped single crystals were obtained as the product. The obtained crystals were washed with THF, H₂O and ethanol several times. The product was then dried overnight in vacuum at 120 ^oC and stored for further analysis. Yield: 0.089 g. IR (KBr, cm^{-1}): 1590, 1486, 1290. XRD 2θ (°): 7.62, 10.30, 13.84, 18.13, 19.17, 22.98. Anal. Calcd. for C₁₈H₁₂MnN₂O₆: C, 53.09; H, 2.97; N, 6.88 Found: C, 52.99; H, 3.31, N, 6.30.

3.1.3. Synthesis of Mn-MOF-74:

General Reaction:

$$MnCl_2 \cdot 4H_2O \ + \ \underset{\substack{\text{Dihydroxyterepthalic} \\ \text{acid (DOT)}}}{\text{DOT}} \ \xrightarrow[120\,^oC,\,24\,h]{DMF} \ \underset{\text{Mn-MOF-74}}{C_8H_2O_6Mn_2}$$
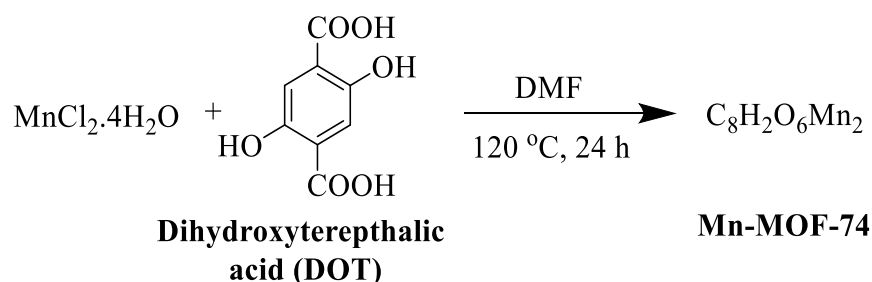
The compound was synthesized using previously reported method by Zhou *et.*al.[1] In two separate vials, 0.219 g $MnCl_2.4H_2O$ (1.11 mmol) and 0.066 g 2,5-dihydroxyterephthalic acid (0.336 mmol) were dissolved in a 15:1:1 mixture of DMF-ethanol-water. The reaction mixtures were sonicated for 5 min and then transferred to an autoclave. The autoclave was place inside pre-heated hot air oven at 120 °C for 24 h. The autoclave was then allowed to cool at room temperature and the obtained brown coloured crystals were washed with ethanol followed by water several times. The sample was then dried overnight and stored for further analysis. Yield: 0.118 g. IR (KBr, cm^{-1}): 1520. PXRD 2θ (°): 6.47, 11.55, 21.15, 24.09, 26.88, 30.90.

.

3.1.4. Synthesis of Mn-BDC:

General Reaction:
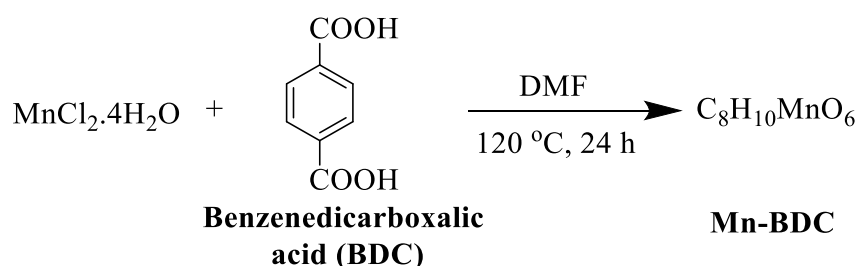
Mn-BDC was synthesized by following the method reported by Sundriyal *et.* al.[2] Here we prepared two separate solutions of 0.300 g $MnCl_2.4H_2O$ (1.52 mmol) and 0.205 g 1,4-benzenedicarboxylic acid (BDC) (1.23 mmol) in 30 mL DMF. After sonicating the resulting solution for 5 min, more 5 mL MeOH was added to the solution. The final solution was transferred into a 50 mL autoclave and kept in an oven at 120 °C for 24 h. After reaction time, the solution was cooled to room temperature and the colourless product obtained was washed thoroughly with DMF, methanol and water. The product was then stored for further analysis. Yield: 0.153 g. IR (KBr, cm^{-1}): 3500, 1570, 1394. PXRD 2θ (°): 9.17, 14.01, 18.68, 28.03, 29.34, 33.36.

.

3.1.5. Synthesis of Mn-TPA-DMF:

General Reaction:

$$MnCl_2.4H_2O \; + \quad \underset{\substack{\textbf{Benzenedicarboxalic}\\ \textbf{acid (BDC)}}}{\overset{COOH}{\underset{COOH}{\bigcirc}}} \quad \xrightarrow[\text{120 }^{\circ}\text{C, 24 h}]{\text{DMF}} \quad \underset{\textbf{Mn-TPA-DMF}}{C_{11}H_{11}NO_5Mn}$$
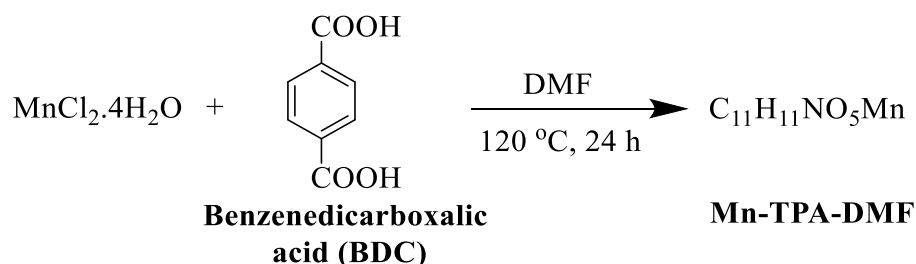
Mn-TPA-DMF was synthesized using a previously reported method by Ladrak *et.* al.[3] Here we dissolved 0.092 g Mn(NO₃).4H₂O (0.516 mmol) and 0.090 g TPA (0.547 mmol) in 10 mL of DMF. After sonicating for 10 min, the resulting solution was transferred into an autoclave and kept inside a hot air oven at 120 °C for 24 h. After cooling the reaction mixture to room temperature, a pale white coloured crystalline compound was obtained which washed with DMF, methanol and water for several times. The product obtained was dried at 130 °C under vacuum and stored for further analysis. Yield: 0.062 g. IR (KBr, cm^{-1}): 1570, 1420. PXRD 2θ (°): 9.49, 14.36, 18.35, 24.90, 28.76, 29.75, 33.77.

3.1.6. Synthesis of Mn-BTC:

General Reaction:

$$MnCl_2.4H_2O \; + \quad \underset{\substack{\textbf{Benzenetricarboxalic}\\ \textbf{acid (BTC)}}}{\overset{COOH}{\underset{HOOC \qquad COOH}{\bigcirc}}} \quad \xrightarrow[\text{120 }^{\circ}\text{C, 24 h}]{\text{DMF}} \quad \underset{\textbf{Mn-BTC}}{C_{18}H_{24}Mn_3O_{18}}$$
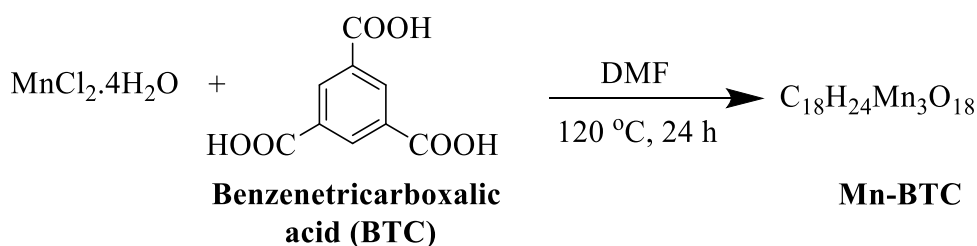
Mn-BTC was synthesized following the procedure reported by Lin *et.* al.[4] Here we prepare a solution containing 3.547 g MnCl₂.4H₂O (18 mmol) and BTC (1.261 g, 6 mmol) in 60 mL DMF:H₂O= 1:1 solvent by sonication for 10 min. The prepared solution was transferred into an autoclave and kept it into a hot air oven at 120 °C for 96 h. After reaction completion, the autoclave was allowed to cool at room temperature and the white coloured product obtained was washed several times with

distilled water and methanol. The product was then dried at 120 °C in vacuum and stored for further analysis. Yield: 1.012 g. IR (KBr, cm^{-1}): 1586, 3500. PXRD 2θ (°): 10.32, 20.65, 29.91, 42.45.

.

3.1.7. Synthesis of Mn-BTEC:

General Reaction:

$$MnCl_2.4H_2O \ + \ \text{Benzenetetracarboxalic acid (BTEC)} \ \xrightarrow[135\ ^oC,\ 24\ h]{DMF:\ MeOH} \ Mn\text{-}BTEC$$
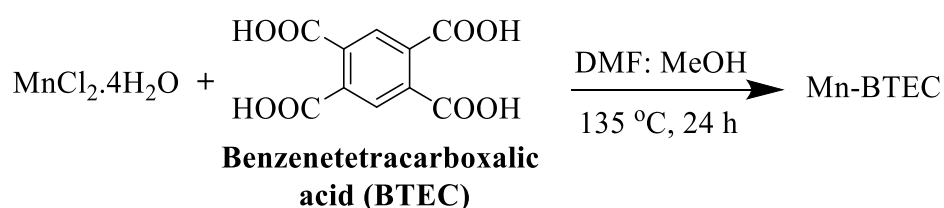
Mn-BTEC was synthesized using the previously reported method by Li *et al.*[5] Here we prepared a mixture of 0.330g MnCl$_2$.4H$_2$O (1.67 mmol) and 0.752 g BTEC (2.96 mmol) in 30 mL DMF:MeOH= 5:1 solvent. They were mixed well by sonicating for 5 min. After mixing, the well mixed solution was poured into a 50 mL autoclave and kept into a hot air oven. The temperature was set to be 135 °C for 24 h. After the reaction time, the autoclave was cooled to room temperature. A pale white coloured product was obtained and the obtained product was washed with DMF, water and methanol for several times. Later the product was dried at 110 °C in vacuum and stored for further analysis. Yield: 0.238 g, IR (KBr, cm^{-1}): 1600. PXRD 2θ (°): 9.83, 21.47, 23.36, 29.01, 40.53.

.

3.1.8. Synthesis of Mn-Co-BTEC:

General Reaction:

$$MnCl_2.4H_2O \ + \ Co(OAc)_2.4H_2O \ + \ \text{Benzenetetracarboxalic acid (BTEC)} \ \xrightarrow[135\ ^oC,\ 24\ h]{DMF:\ MeOH} \ \substack{C_{10}H_6O_8Mn_{1.7}Co_{0.3} \\ Mn_{1.7}Co_{0.3}BTEC}$$
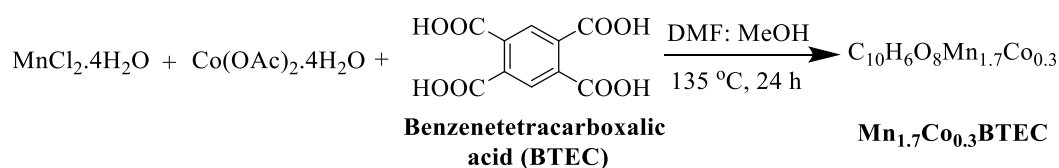
Mn-Co-BTEC was synthesized using the same technique used for Mn-BTEC by Li *et. al.*[5] Here we prepared a mixture of 0.755 g MnCl$_2$.4H$_2$O (3.81 mmol), 2.287 g BTEC

(8.99 mmol) and 0.873 g Co(NO$_3$)$_2$.6H$_2$O (3 mmol) in 60 mL DMF:MeOH= 5:1 solvent. They were mixed well by sonicating for 5 mins. After mixing, the solution was poured into a 100 mL Teflon lined stainless steel autoclave and kept into an oven. The temperature was set to be 135 ^{o}C for 24 h. After the reaction time, the autoclave was cooled to room temperature. A violet coloured product was obtained and the obtained product was washed with DMF and MeOH. Later the product was dried at 110 °C in vacuum and stored for further analysis. Yield: 0.186 g. IR (KBr, cm^{-1}): 1596. PXRD 2θ (°): 9.85, 21.48, 23.57, 29.43, 40.99.

3.2. Characterization of Mn-based Coordination Polymers:

All the Mn-based coordination polymers were characterized using conventional tools such as single crystal X-ray diffraction, powder X-ray diffraction, elemental analysis, FT-IR spectroscopy and thermogravimetric analysis.

3.2.1. Mn-SKU-1:

3.2.1.1.   Crystal Structure description:

Fine X-ray diffraction quality crystals were diffracted and from the refinement data, the crystal system was found to be monoclinic with P2$_1$/c space group. In each unit cells, the edge lengths are a= 7.5388, b= 9.4230, c= 6.3423 and the three angles between the edges are α= 90◦, β= 94.363◦ and γ= 90◦ (*table 3.1*). The asymmetric unit present here contains two Mn(II) atom having a distorted octahedral geometry (*figure 3.1 (a)*). Each Mn(II) metal center is coordinated with five O atoms from DOT molecule- four in equatorial position and one in axial position. However, the other axial position is occupied by a H$_2$O molecule (*figure 3.1 (b)*). The extended framework formed by the asymmetric units are given in *figure 3.2(a)-(b)*. The Mn-O bond length for the coordinated Mn with the O atoms from -COO$^-$ groups of DOT molecule ranges from 2.26 Å to 2.27 Å whereas the Mn-O bond length for the coordinated H$_2$O molecule is 2.26 Å. A Mn$_2$O$_2$ planar ring is formed where the Mn-O-Mn bond angle is 101.6 ^{o} and Mn···Mn distance is 3.48 Å. We have also determined the SBU for the framework which is given in *figure 3.4*. Here the SBU is an octanuclear unit where two of Mn atoms forms a binuclear polyhedra and four of such binuclear polyhedral units form the SBUs by getting extended through the corner

O-atoms. The SBUs later extends in 2D forming a 2Dlayer and finally results in a 3D framework by connecting to another 2D layers bridged by DOT linkers (*figure 3.3*). A comparison of the simulated XRD pattern and experimental PXRD pattern is given in *figure 3.5* that shows excellent match between the experimental and simulated pattern which confirms the phase purity of the bulk material. All the atomic parameters are mentioned in *table 3.1/3.3-3.5.*

Table 3.1: Crystal data of Mn-SKU-1

Compound Name	Mn-SKU-1
Empirical Formula	$C_8H_6Mn_2O_8$
Formula Weight	339.88
T/K	293(2)
Wavelength / Å	0.71073
Crystal system	Monoclinic
Space Group	P21/c
a/Å	7.5388(4)
b/Å	9.4230(5)
c/Å	6.3423(3)
α/ ^{O}	90
β / ^{O}	94.363
γ / ^{O}	90
V (Å^3)	449.23
Z	4
R factor	0.076
Goodness of Fit	1.03
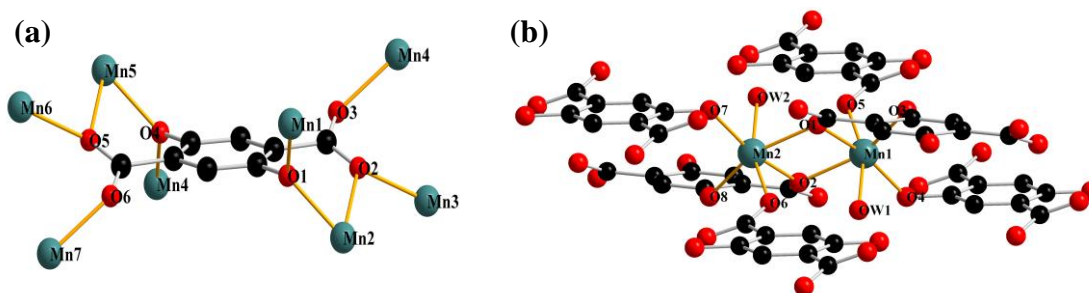
Figure 3.1: Crystal Structure of Mn-SKU-1.
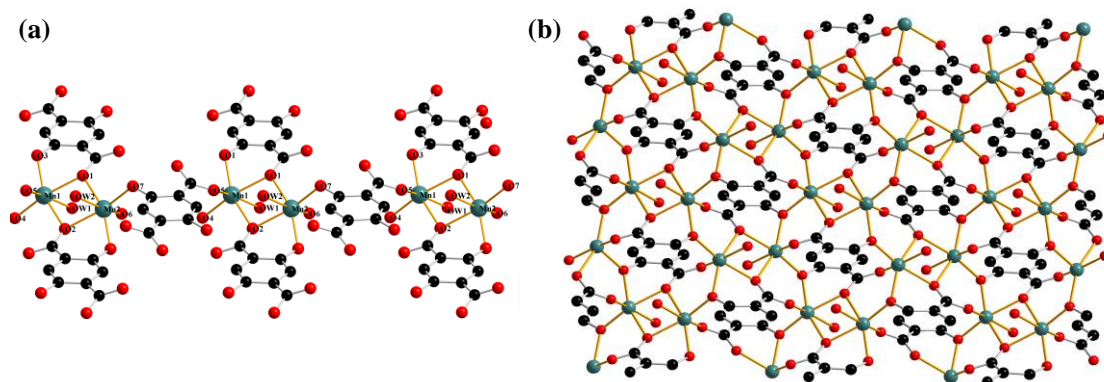
Figure 3.2: Extension of asymmetric unit throughout the framework of Mn-SKU-1.
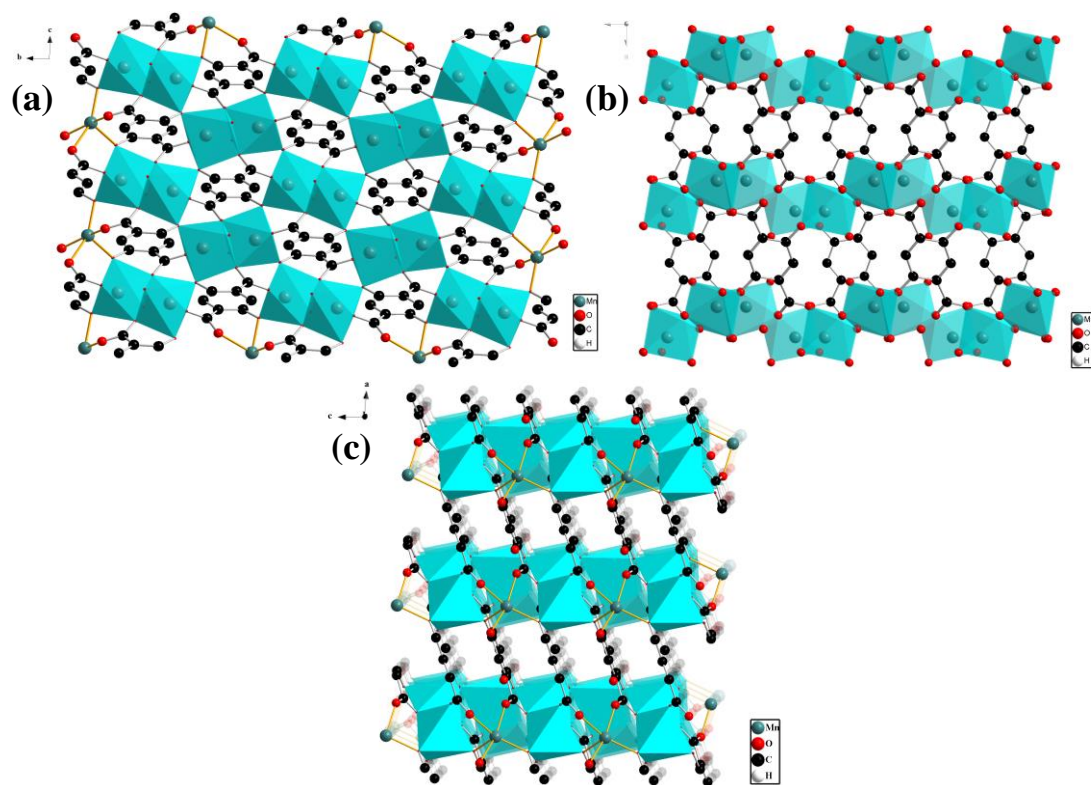
Figure 3.3: 3D network of Mn-SKU-1.
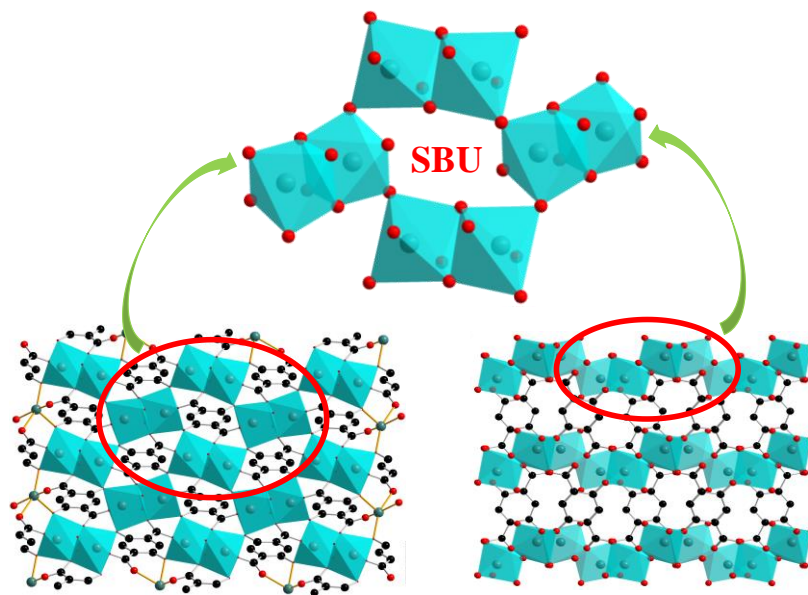
Figure 3.4: SBU of Mn-SKU-1.
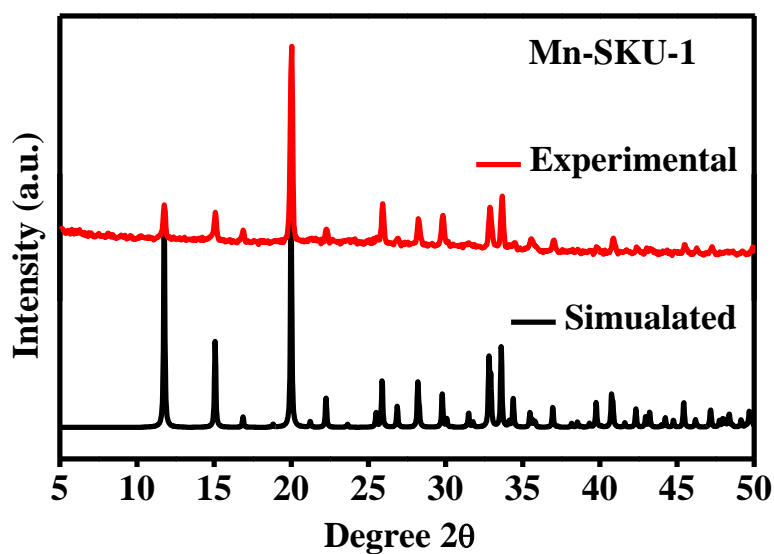
Figure 3.5: XRD patterns of Mn-SKU-1

Based on the refinement of crystal data, the empirical formula was predicted to be $C_8H_6Mn_2O_8$. Further to confirm the prediction of molecular formula, we have performed CHN analysis from which we confirm the molecular formula of the compound is $C_8H_6Mn_2O_8$. The calculated value of amount of C and H present and the analyzed value are given below (*table 3.2*):

Table 3.2: Predicted and experimental CHN analysis data.

CHN Analysis	Carbon (C)	Hydrogen (H)	Nitrogen (N)
Predicted	28.26	1.78	NA
Experimental	28.67	1.88	NA

Table 3.3: Atomic coordinates of selected atoms.

Sl. No.	Atom	X	Y	Z
1	Mn1	0.62077	0.84372	0.04222
2	O1	0.4470	0.5484	0.2925
3	O2	0.3729	0.7423	0.1057
4	O3	0.2614	0.3091	0.1495
5	O1W	0.8196	0.9978	-0.0785
6	C1	0.1360	0.4048	0.0767
7	C3	0.3409	0.6181	0.1635
8	C4	0.0317	0.6427	0.0054
9	C2	0.1667	0.5527	0.0834
10	H1	0.069	0.754	-0.001
11	O2	-0.3729	0.2577	-0.1057
12	O3	-0.2614	0.6909	-0.1495
13	C1	-0.1360	0.5952	-0.0767
14	C3	-0.3409	0.3819	-0.1635
15	C4	-0.0317	0.3573	-0.0054
16	C2	-0.1667	0.4473	-0.0834
17	H1	-0.069	0.246	0.001
18	O1	-0.4470	0.4516	-0.2925
19	Mn1	-0.62077	0.15628	-0.04222
20	O1W	-0.8196	0.0022	0.0785
21	Mn1	-0.37923	0.84372	0.04222
22	Mn1	-0.62077	0.34372	-0.54222
23	Mn1	0.37923	0.34372	0.45778
24	Mn1	0.37923	0.15628	-0.04222

25	Mn1	-0.37923	0.65628	-0.45778
26	Mn1	0.62077	0.65628	0.54222
27	O1	-0.4470	0.0484	0.2075
28	O1	0.5530	1.0484	0.2075
29	O1	-0.5530	-0.0484	-0.2075
30	O1	0.4470	0.9516	-0.2075
31	O3	-0.7386	0.3091	0.1495
32	O3	0.7386	0.8091	0.3505
33	O3	0.7386	0.6909	-0.1495
34	O3	-0.7386	0.1909	-0.3505

Table 3.4: Selected bond lengths (Å) of Mn-SKU-1.

Sl. No.	Atom1	Atom2	Length	Sl. No.	Atom1	Atom2	Length
1	Mn1	O1	2.272	9	O3	C1	1.362
2	Mn1	O1	2.223	10	C1	C2	1.413
3	Mn1	O2	2.164	11	C1	C4	1.403
4	Mn1	O3	2.11	12	C3	C2	1.504
5	Mn1	O3	2.123	13	C4	C2	1.387
6	Mn1	O1W	2.262	14	C4	H1	1.09
7	O1	C3	1.281	15	C4	C1	1.403
8	O2	C3	1.255				

Table 3.5: Selected bond angles (º) of Mn-SKU-1

Atom1	Atom2	Atom3	Angle	Atom1	Atom2	Atom3	Angle
O2	Mn1	O1W	161.9	C1	O3	Mn1	116.4
O2	Mn1	O1	93.5	C1	O3	Mn1	124.4
O2	Mn1	O1	82.2	Mn1	O3	Mn1	118.1
O2	Mn1	O3	93.9	O3	C1	C2	122.4
O2	Mn1	O3	102.2	O3	C1	C4	119.8
O1W	Mn1	O1	77.8	C2	C1	C4	117.8
O1W	Mn1	O1	80.5	O1	C3	O2	122.7
O1W	Mn1	O3	99.8	O1	C3	C2	119.5
O1W	Mn1	O3	85.7	O2	C3	C2	117.8
O1	Mn1	O1	78.4	C2	C4	H1	115

O1	Mn1	O3	78.3	C2	C4	C1	123.6
O1	Mn1	O3	163.5	H1	C4	C1	121
O1	Mn1	O3	156.1	C1	C2	C3	123.5
O1	Mn1	O3	98.7	C1	C2	C4	118.6
O3	Mn1	O3	105.1	C3	C2	C4	117.9
C3	O1	Mn1	125.3	C3	O2	Mn1	130.8
C3	O1	Mn1	121.7	C1	O3	Mn1	124.4
Mn1	O1	Mn1	101.6	C1	O3	Mn1	116.4
Mn1	O2	C3	130.8	Mn1	O3	Mn1	118.1

3.2.1.2.   Infrared Spectrum:

FT-IR spectroscopy data shows the binding pattern of DOT and the presence H_2O molecule in the framework. Peak at 3600-3200 cm^{-1} region corresponds to characteristic O-H stretching of coordinated H_2O molecule. The peaks at 1650 cm^{-1}& 1386 cm^{-1} shifted to 1650 cm^{-1}& 1386 cm^{-1} due to metalation of carboxylic groups and corresponds to O-C-O asymmetric and O-C-O symmetric stretching respectively (*figure 3.6*).[6]
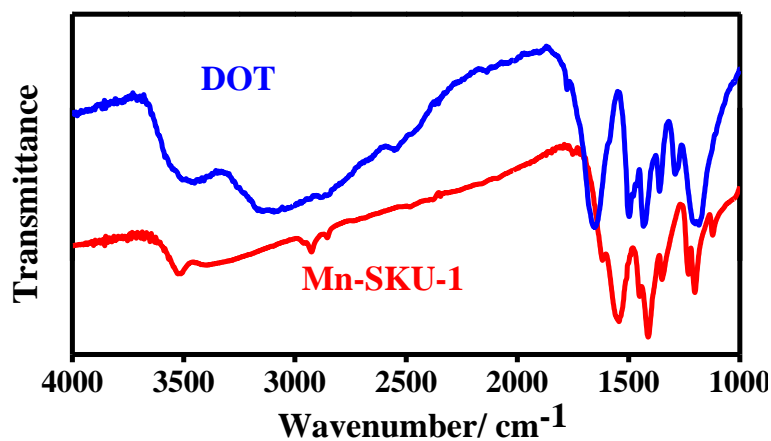
Figure 3.6: FT-IR spectra of Mn-SKU-1

3.2.1.3.   Thermogravimetric Analysis:

TGA analysis was carried out at 30 °C to 600 °C under 60 mL min^{-1} N$_2$ gas flow. The TGA results revealed that the compound is stable up to 300 °C. Weight loss of ~8.5 % at around 180-200 °C corresponds to two water molecules present in the framework. Again, overall weight loss of ~50 % at around 300 °C accounts for the loss of DOT molecule as well as the collapse of the framework (*figure 3.7*). PXRD was performed for the final product obtained after pyrolysis and patterns reveals that the product obtained is α-Mn$_2$O$_3$. The product was stored for further possible analysis.
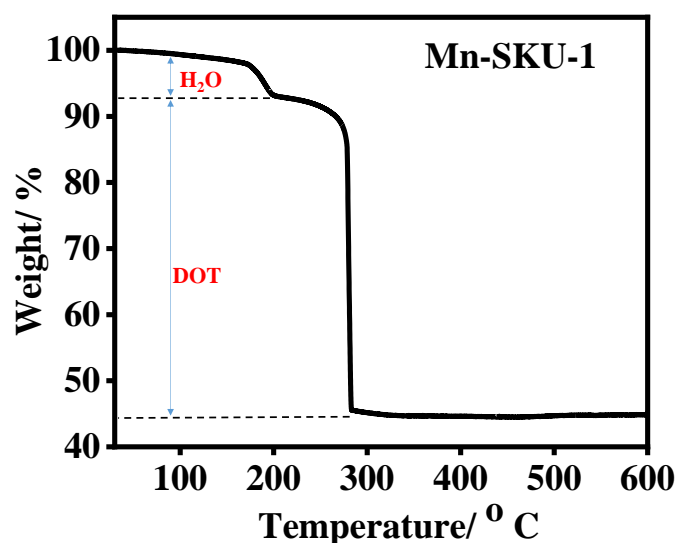
Figure 3.7: TGA curve of Mn-SKU-1

3.2.2. Mn-SKU-2:

3.2.2.1.   Single Crystal X-ray Diffraction:

From the refinement data using the same technique use in earlier case, the crystal system was found to be orthorhombic with *Pcca* space group. In each unit cells, the edge lengths are a= 17.0513, b= 11.6011, c= 19.2754 and the three angles between the edges are α=β=γ=90∘ (*table 3.6*). The asymmetric unit present here contains one Mn(II) center coordinated to four O atoms from two different DOT molecules in equatorial positions and the axial positions are occupied by two N atom from two different 4,4'-BPY molecules (*figure 3.8*). Here the –COO⁻ group is linked to metal center in chelating as well as in bridging fashion (*figure 3.9*). In case of chelating O-Mn-O bonding, the bond length for the coordinated Mn with the O atoms from -COO⁻

groups of DOT molecule ranges from 2.20 Å to 2.31 Å. Whereas, in bridging O-Mn-O bonding mode, the bond length for the coordinated Mn with the O atoms is 2.10 Å. Two N atoms are present in the axial positions which belongs to the 4,4'-BPY moiety and the Mn-N bonds ranges from 2.25 Å to 2.27 Å. A Mn_2CO_4 planar ring is formed here where the O-Mn-O bond angle is 128.65° and Mn…Mn distance is 4.03 Å. We have also determined the SBU for the framework which is given in *figure 3.11*. Here also the SBU is a cubic unit where two Mn atoms forming two distorted octahedral shaped polyhedra are connected DOT and BPY linkers resulting in the whole rigid bipillared cubic shaped SBU. The SBUs are getting extended into a 3D framework forming an interpenetrated framework (*figure 3.10*). A comparison of the simulated XRD pattern and experimental PXRD pattern is given in *figure 3.12* which confirms the phase purity of the bulk material. All the atomic parameters are mentioned in *table 3.6/3.8-3.10.*

Table 3.6: Crystal data of Mn-SKU-2

Compound Name	Mn-SKU-2
Emperical Formula	$C_{18}H_{12}MnN_2O_6$
Formula Weight	407.01
T/K	293(2)
Wavelength / Å	1.54184
Crystal system	Orthorhombic
Space Group	Pcca
a/Å	17.0513(3)
b/Å	11.6011(3)
c/Å	19.2754(3)
α/ °	90
β / °	90
γ / °	90
V ($Å^3$)	3812.94
Z	8
R factor	0.1141
Goodness of Fit	1.14
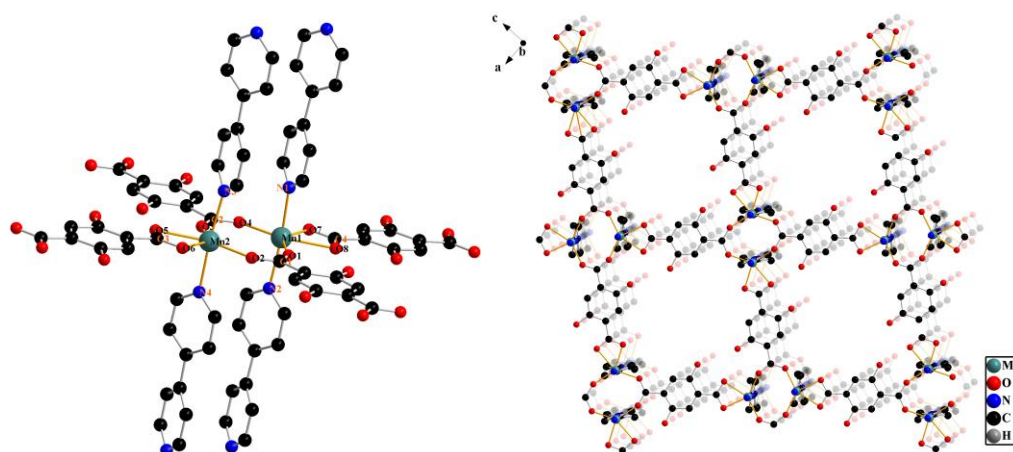
Figure 3.8: Crystal Structure of Mn-SKU-2.
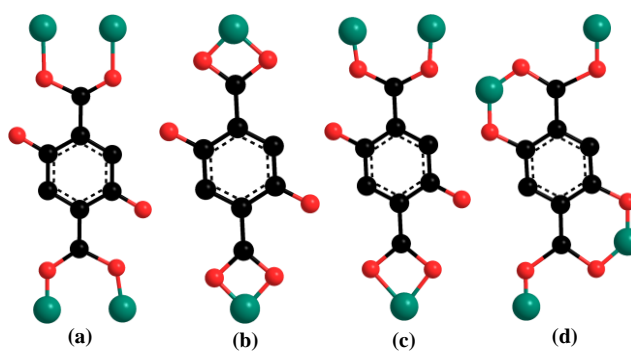
Figure 3.9: Different bridging modes of DOT molecule.
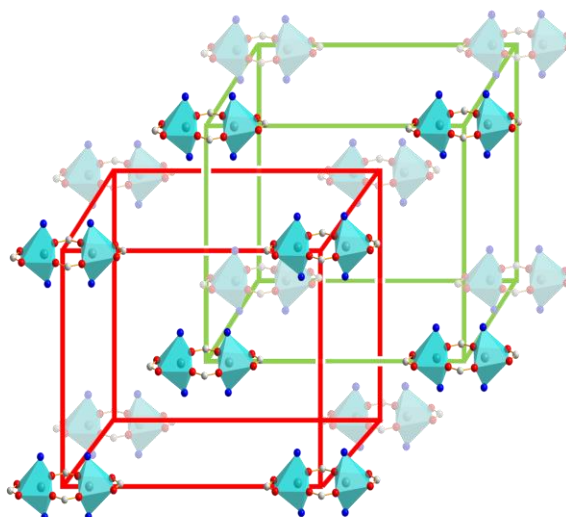
Figure 3.10: 3D interpenetrated network of Mn-SKU-2.
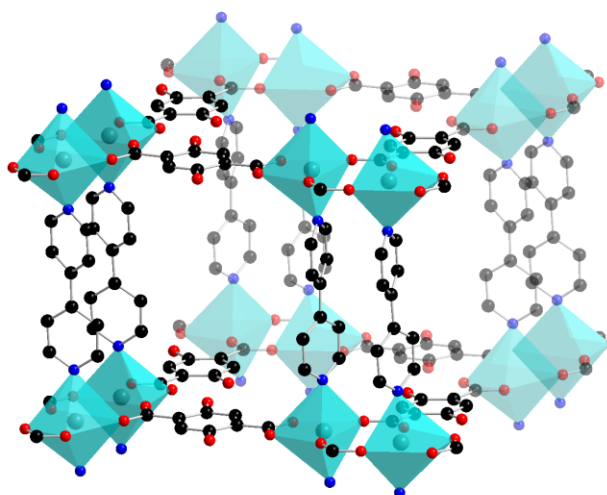
Figure 3.11: SBU of Mn-SKU-2.
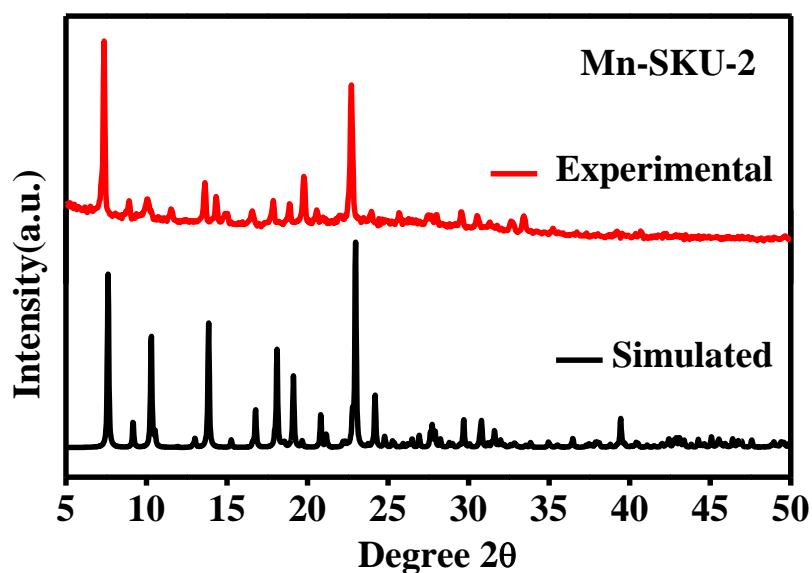
Figure 3.12: XRD patterns of Mn-SKU-2.

Based on the refinement of crystal data, the empirical formula was predicted to be $[C_{18}H_{12}MnN_2O_6]_n$. Further to confirm the prediction of molecular formula, we have performed CHN analysis from which we confirm the molecular formula of the compound is $[C_{18}H_{12}MnN_2O_6]_n$. The calculated value of amount of C and H present and the analyzed value are given below (*table 3.7*):

Table 3.7: Predicted and experimental CHN analysis data.

CHN Analysis	Carbon (C)	Hydrogen (H)	Nitrogen (N)
Predicted	53.09	2.97	6.88
Experimental	52.99	3.31	6.30

Table 3.8: Selected atoms present in Mn-SKU-2.

Sl. No.	Atom	X	Y	Z
1	MN1	0.412331	0.843602	0.179934
2	O4	0.532289	0.838004	0.148891
3	O2	0.634552	0.841208	0.219455
4	O5	0.89281	0.843858	-0.061059
5	O3	0.795003	0.84643	-0.132925
6	N2	0.419306	1.03736	0.186834
7	N1	0.413725	1.64763	0.181993
8	O6	0.869853	0.850338	0.072155
9	C1	0.477506	1.09903	0.157967
10	C2	0.478026	1.21672	0.157001
11	O7	0.554082	0.839675	0.012408
12	C4	0.658429	0.843719	0.098666
13	C6	0.416411	1.27811	0.185816
14	C7	0.604511	0.840665	0.16046
15	C8	0.76445	0.847697	-0.011834
16	C9	0.355556	1.21376	0.215383
17	C10	0.359257	1.09594	0.214826
18	C11	0.414189	1.40707	0.183565
19	C12	0.739414	0.847635	0.110343
20	H12	0.757721	0.849788	0.155773
21	C13	0.792899	0.848406	0.056771
22	C14	0.820248	0.846678	-0.072312
23	C15	0.684956	0.844552	-0.024325
24	C16	0.450691	1.58513	0.135267
25	H16	0.477054	1.62425	0.100201

26	C17	0.630812	0.844351	0.030094
27	C18	0.373374	1.46922	0.231969
28	H18	0.345264	1.43143	0.266496
29	C19	0.374061	1.58777	0.22939
30	H19	0.345356	1.62816	0.262437
31	C20	0.453428	1.46754	0.134161
32	H20	0.48181	1.42926	0.100001
33	H2	0.519083	1.25439	0.134059
34	H5	0.672254	0.858471	-0.071234
35	H1	0.517834	1.04649	0.141075
36	H4	0.319705	1.05031	0.240753
37	H3	0.312574	1.24479	0.243976
38	H6	0.53098	0.831511	0.046036
39	H7	0.887792	0.862986	0.034139
40	MN1	0.412331	1.8436	0.179934
41	MN1	0.587669	0.843602	0.320066
42	MN1	0.912331	0.843602	-0.179934
43	O2	0.365448	0.841208	0.280545
44	O5	0.39281	0.843858	0.061059
45	O3	0.295003	0.84643	0.132925
46	N1	0.413725	0.647635	0.181993

Table 3.9: Selected bond lengths of Mn-SKU-2.

Atom1	Atom2	Length	Atom1	Atom2	Length
MN1	O4	2.1322	O7	H6	0.7644
MN1	N2	2.2549	C4	C7	1.5051
MN1	O2	2.0978	C4	C12	1.3999
MN1	O5	2.3154	C4	C17	1.4032
MN1	O3	2.1965	C6	C9	1.3996
MN1	N1	2.2739	C6	C11	1.4971
O4	C7	1.2519	C8	C13	1.4086
O2	C7	1.2472	C8	C14	1.5048
O2	MN1	2.0978	C8	C15	1.3772

O5	C14	1.2566	C9	C10	1.3684
O5	MN1	2.3154	C9	H3	0.9851
O3	C14	1.2451	C10	H4	0.9924
O3	MN1	2.1965	C11	C18	1.3692
N2	C1	1.344	C11	C20	1.3589
N2	C10	1.3422	C12	H12	0.93
N1	C16	1.3169	C12	C13	1.3777
N1	C19	1.3321	C15	C17	1.3974
N1	MN1	2.2739	C15	H5	0.9437
O6	C13	1.3454	C16	H16	0.93
O6	H7	0.8075	C16	C20	1.3652
C1	C2	1.3654	C18	H18	0.93
C1	H1	0.9749	C18	C19	1.3763
C2	C6	1.3855	C19	H19	0.93
C2	H2	0.9363	C20	H20	0.93
O7	C17	1.3531			

Table 3.10: Selected bond angles of Mn-SKU-2.

Atom1	Atom2	Atom3	Angle	Atom1	Atom2	Atom3	Angle
O4	Mn1	N2	89.79	O2	C7	C4	118.07
O4	Mn1	O2	128.65	C13	C8	C14	120.64
O4	Mn1	O5	81.97	C13	C8	C15	120.21
O4	Mn1	O3	139.33	C14	C8	C15	119.12
O4	Mn1	N1	87.96	C6	C9	C10	119.7
N2	Mn1	O2	88.78	C6	C9	H3	125.77
N2	Mn1	O5	93.71	C10	C9	H3	113.81
N2	Mn1	O3	93.3	N2	C10	C9	122.97
N2	Mn1	N1	174.31	N2	C10	H4	116.79
O2	Mn1	O5	149.33	C9	C10	H4	119.84
O2	Mn1	O3	91.98	C6	C11	C18	121.29
O2	Mn1	N1	88.55	C6	C11	C20	121.58
O5	Mn1	O3	57.37	C18	C11	C20	117.12
O5	Mn1	N1	91.15	C4	C12	H12	118.91

O3	Mn1	N1	91.81	C4	C12	C13	122.19
Mn1	O4	C7	153.25	H12	C12	C13	118.91
C7	O2	Mn1	133.35	O6	C13	C8	122.88
C14	O5	Mn1	88.32	O6	C13	C12	118.72
C14	O3	Mn1	94.14	C8	C13	C12	118.4
Mn1	N2	C1	123.04	O5	C14	O3	120.15
Mn1	N2	C10	119.23	O5	C14	C8	119.28
C1	N2	C10	117.4	O3	C14	C8	120.55
C16	N1	C19	115.15	C8	C15	C17	121.27
C16	N1	Mn1	122.93	C8	C15	H5	112.88
C19	N1	Mn1	121.87	C17	C15	H5	124.6
C13	O6	H7	99.93	N1	C16	H16	117.37
N2	C1	C2	122.87	N1	C16	C20	125.26
N2	C1	H1	109.04	H16	C16	C20	117.37
C2	C1	H1	128.03	O7	C17	C4	124.17
C1	C2	C6	120.24	O7	C17	C15	116.73
C1	C2	H2	118.56	C4	C17	C15	119.04
C6	C2	H2	121.08	C11	C18	H18	120.09
C17	O7	H6	106.83	C11	C18	C19	119.82
C7	C4	C12	118.43	H18	C18	C19	120.09
C7	C4	C17	122.72	N1	C19	C18	123.37
C12	C4	C17	118.84	N1	C19	H19	118.31
C2	C6	C9	116.82	C18	C19	H19	118.31
C2	C6	C11	121.42	C11	C20	C16	119.22
C9	C6	C11	121.74	C11	C20	H20	120.39
O4	C7	O2	124.51	C16	C20	H20	120.39
O4	C7	C4	117.42	O5	Mn1	O3	57.37

3.2.2.2. Infrared Spectrum:

IR spectroscopy data shows the binding pattern of DOT and the presence BPY molecule in the framework. The peaks at 1650 cm^{-1} & 1500 cm^{-1} shifted to 1590 cm^{-1} & 1486 cm^{-1} due to metalation of carboxylic groups and corresponds to O-C-O

asymmetric and O-C-O symmetric stretching respectively. The peak at ~1400 cm^{-1} shifted to 1290 cm^{-1} due to metalation of N and corresponds C-N stretching.[6]
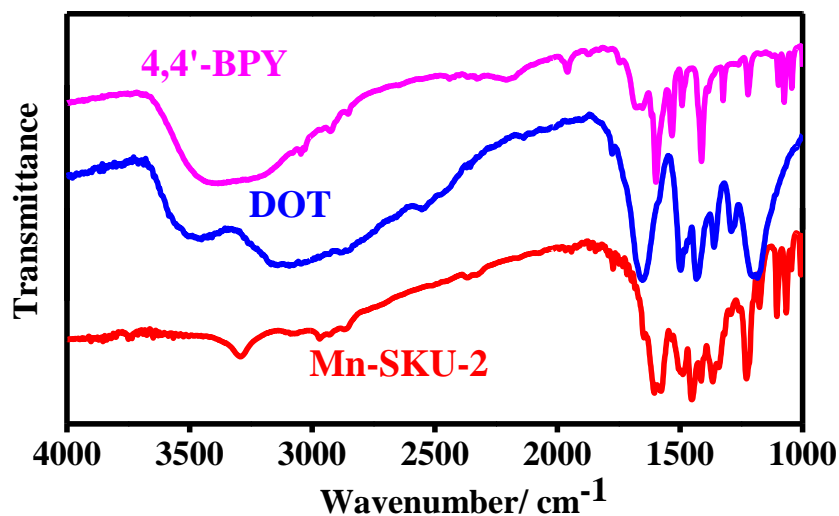
Figure 3.13: FT-IR spectra of Mn-SKU-2.

3.2.2.3. Thermogravimetric Analysis:

TGA analysis was carried out at 30 °C to 600 °C under 60 mL min^{-1} N$_2$ gas flow. The TGA results revealed that the compound is stable up to 300 °C. Weight loss of ~80 % at around 300 °C accounts for the loss of DOT and 4,4'-BPY molecules as well as the collapse of the framework. PXRD was performed for the final product obtained after pyrolysis and comparison of the patterns reveals that the product obtained is α-Mn$_2$O$_3$. The product was stored for further possible analysis.

Figure 3.14: TGA curve of Mn-SKU-2.

3.2.3. Mn-MOF-74:

3.2.3.1. PXRD Pattern:

PXRD was performed to check whether the material is phase pure or not. The obtained pattern gave all major peaks at 2θ= 6.47, 11.55, 21.15, 24.09, 26.88, 30.90.[1,7,8]

Figure 3.15: PXRD pattern of Mn-MOF-74.

3.2.3.2. Infrared Spectrum:

IR spectroscopy data shows the binding pattern of DOT molecule in the framework. The peaks at ~1660 cm^{-1} shifted to ~1520 cm^{-1} due to metalation of carboxylic groups and corresponds to C=O stretching.[6]
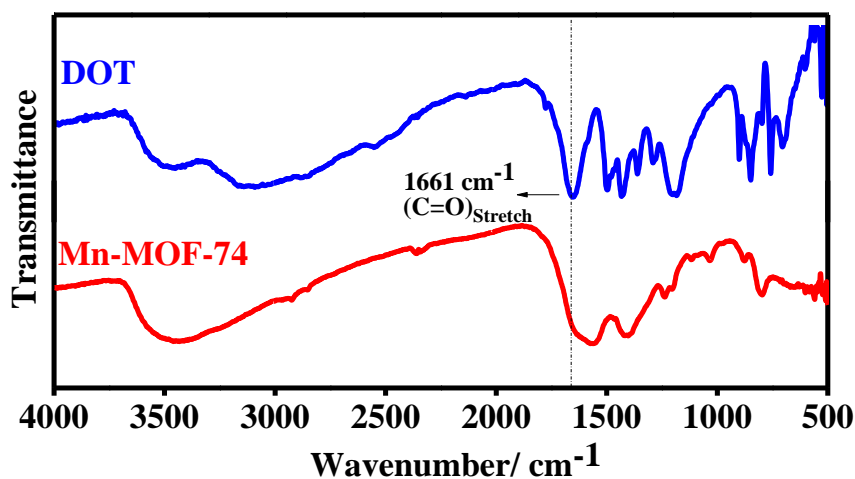
Figure 3.16: FT-IR spectra of Mn-MOF-74.

3.2.3.3. Thermogravimetric Analysis:

TGA analysis was carried out at 30 °C to 600 °C under 60 mL min^{-1} N$_2$ gas flow. The TGA results revealed that the compound is stable up to 300 °C. Overall weight loss of ~63 % at around 300 °C accounts for the loss of DOT molecule as well as the collapse of the framework.
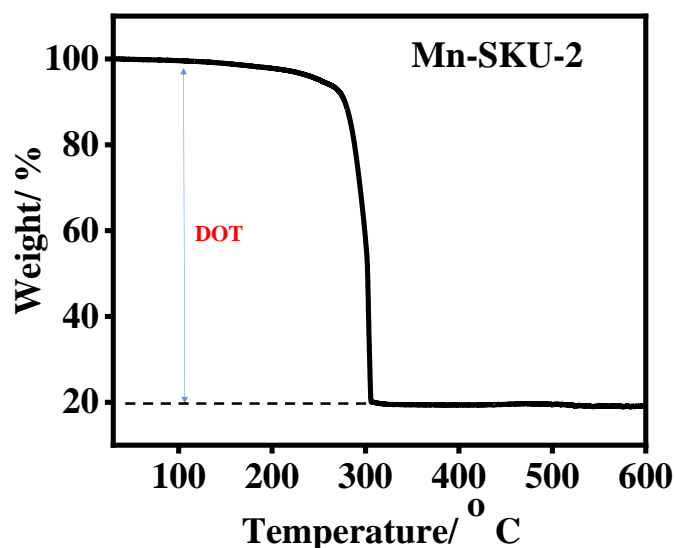

Figure 3.17: TGA curve of Mn-MOF-74.

3.2.4. Mn-BDC:

3.2.4.1. PXRD Pattern:

PXRD was performed to check whether the material is phase pure or not. The obtained pattern gave all major peaks at 2θ= 9.17, 14.01, 18.68, 28.03, 29.34, 33.36.[2,9]

Figure 3.18: PXRD pattern of Mn-BDC.

3.2.4.2.   Infrared Spectrum:

IR spectroscopy data shows the binding pattern of BDC and the presence H_2O molecule in the framework. A broad peak near 3500 cm^{-1} corresponds to characteristic O-H stretching of coordinated H_2O molecule. The peaks at 1689 cm^{-1} & 1486 cm^{-1} shifted to 1570 cm^{-1}& 1394 cm^{-1} due to metalation of carboxylic groups and corresponds to O-C-O asymmetric and O-C-O symmetric stretching respectively.[6]

Figure 3.19: FT-IR spectra of Mn-BDC.

3.2.4.3.   Thermogravimetric Analysis:

TGA analysis was carried out at 30 °C to 600 °C under 60 mL min^{-1} N_2 gas flow. The TGA results revealed that the compound is stable up to ~380 °C. Weight loss of 16 % at around 180-200 °C corresponds to two water molecules present in the framework. Again, overall weight loss of 68 % at around 380 °C accounts for the loss of BDC molecule as well as the collapse of the framework.

Figure 3.20: TGA curve of Mn-BDC.

3.2.5. Mn-TPA-DMF:

3.2.5.1.   PXRD Pattern:

PXRD was performed to check whether the material is phase pure or not. The obtained pattern gave all major peaks at 2θ= 9.49, 14.36, 18.35, 24.90, 28.76, 29.75, 33.7.[3]
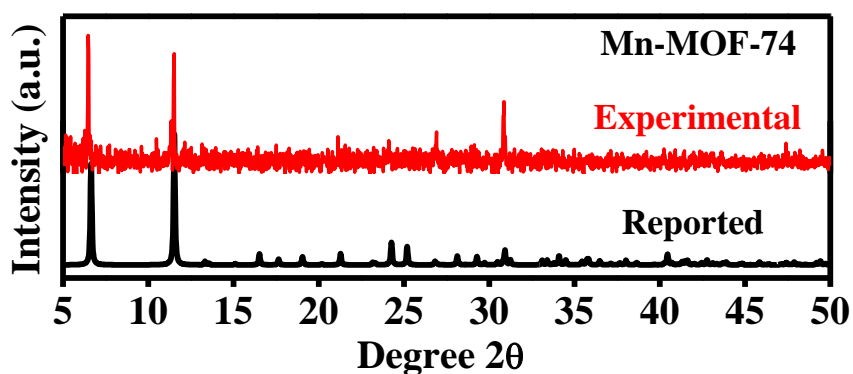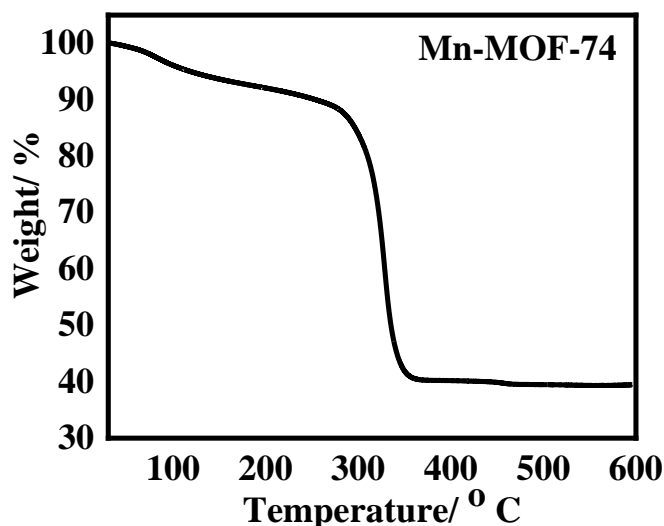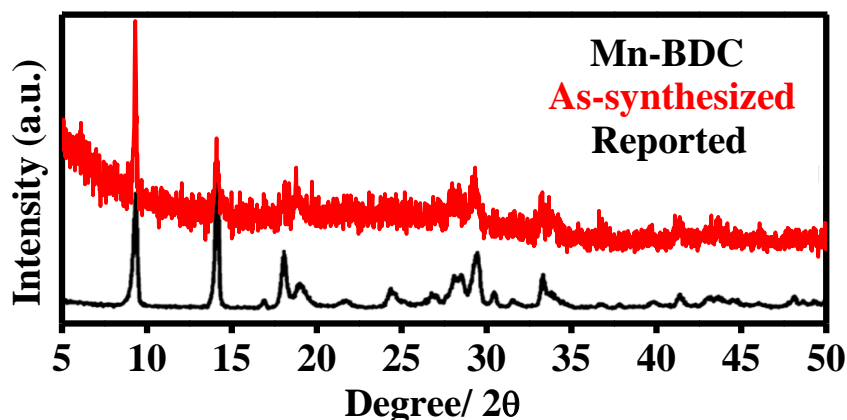

Figure 3.21: PXRD pattern of Mn-TPA-DMF.

3.2.5.2.   Infrared Spectrum:

IR spectroscopy data shows the binding pattern of DOT and the presence of DMF molecule in the framework. The peaks at 1690 cm^{-1} shifted to 1570 cm^{-1} due to metalation of carboxylic groups and corresponds to C=O stretching. Again, peak near 1420 cm^{-1} corresponds C-H bending frequency for DMF molecules.[6]
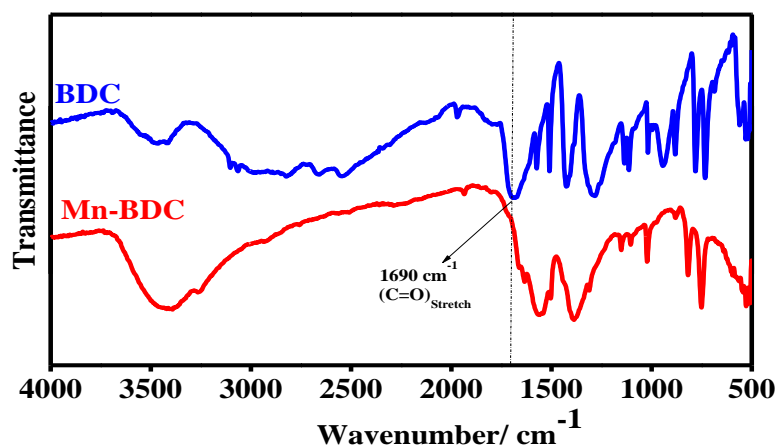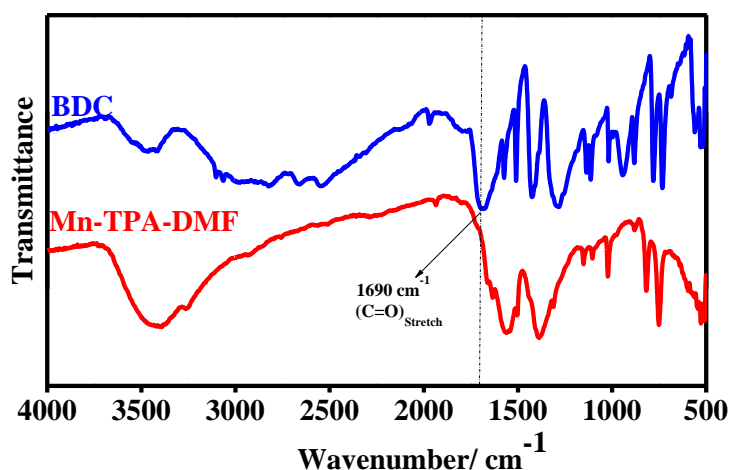

Figure 3.22: FT-IR spectra of Mn-TPA-DMF.

3.2.5.3. Thermogravimetric Analysis:

TGA analysis was carried out at 30 °C to 600 °C under 60 mL min^{-1} N$_2$ gas flow. The TGA results revealed that the compound is stable up to 300 °C. Weight loss of 20 % at around 180-200 °C corresponds to two DMF molecules present in the framework. Again, overall weight loss of 38 % at around 580 °C accounts for the loss of BDC molecule as well as the collapse of the framework.

Figure 3.23: TGA curve of Mn-TPA-DMF.

3.2.6. Mn-BTC:

3.2.6.1. PXRD Pattern:

PXRD was performed to check whether the material is phase pure or not. The obtained pattern gave all major peaks at 2θ= 9.17, 14.01, 18.68, 28.03, 29.34, 33.36.[10,11]

Figure 3.24: PXRD pattern of Mn-BTC.

3.2.6.2.   Infrared Spectrum:

IR spectroscopy data shows the binding pattern of BTC and the presence H_2O molecule in the framework. The peaks at 1719 cm^{-1} shifted to 1586 cm^{-1} due to metalation of carboxylic groups and corresponds C=O stretching respectively. Again, a broad peak near 3500 cm^{-1} corresponds to the O-H stretching frequency of the water molecules.[6]
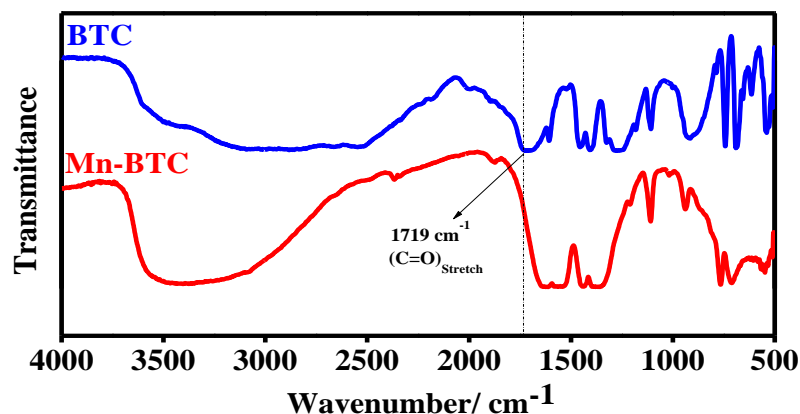
Figure 3.25: FT-IR spectra of Mn-BTC

3.2.6.3.   Thermogravimetric Analysis:

TGA analysis was carried out at 30 °C to 600 °C under 60 mL min^{-1} N_2 gas flow. The TGA results revealed that the compound is stable up to ~400 °C. Weight loss of 12 % at around 150-200 °C corresponds to 6 water molecules present in the framework. Again, overall weight loss of 63 % at around 400 °C accounts for the loss of BTC molecule as well as the collapse of the framework.
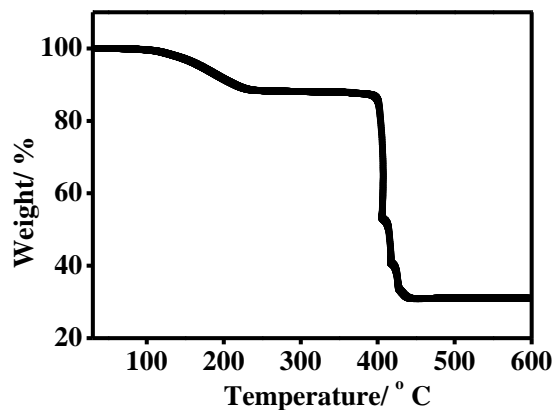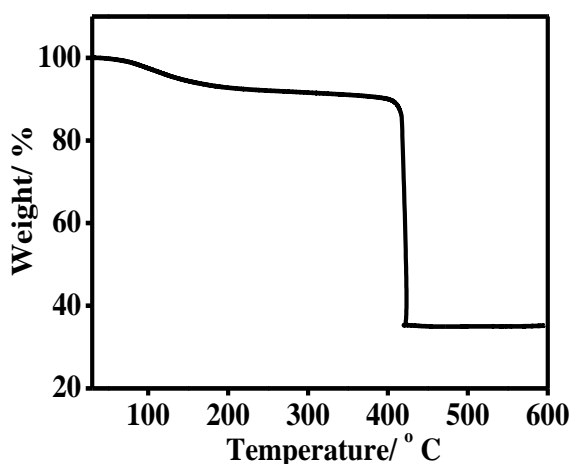

Figure 3.26: TGA curve of Mn-BTC.

3.2.7. Mn-BTEC:

3.2.7.1.   PXRD Pattern:

PXRD was performed to check whether the material is phase pure or not. The obtained pattern gave all major peaks at 2θ= 9.17, 14.01, 18.68, 28.03, 29.34, 33.36.[5]
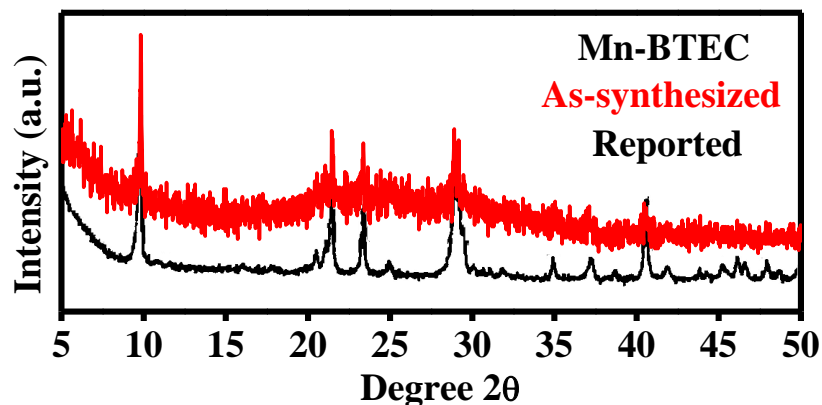
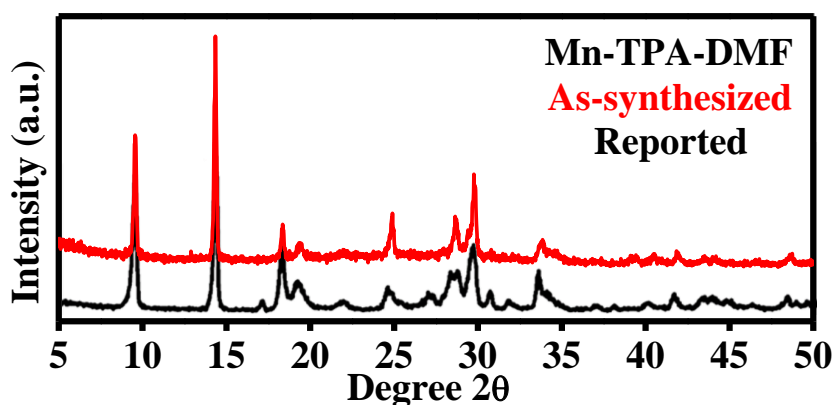**Figure 3.27**: PXRD pattern of Mn-BTEC.

3.2.7.2.   Infrared Spectrum:

IR spectroscopy data shows the binding pattern of DOT and the presence H_2O molecule in the framework. The peaks at 1710 cm^{-1} shifted to 1600 cm^{-1} due to metalation of carboxylic groups and corresponds C=O stretching.[6]
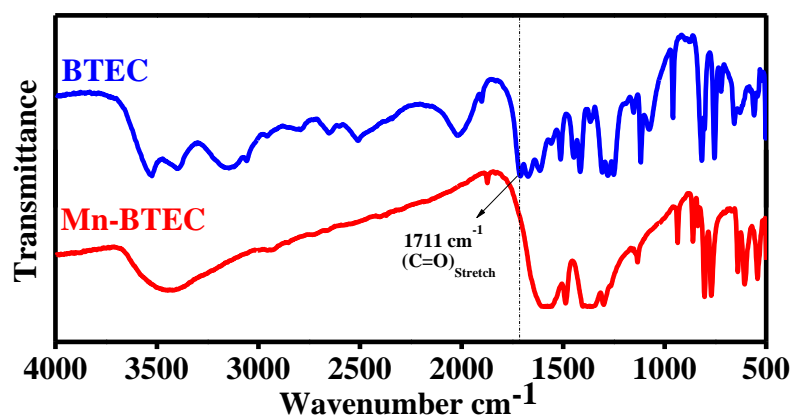
Figure 3.28: FT-IR spectra of Mn-BTEC.

3.2.7.3.   Thermogravimetric Analysis:

The TGA results revealed that the compound is stable up to 360 °C. An overall weight loss of 60 % at around 370 °C accounts for the loss of BTEC molecule as well as the collapse of the framework.
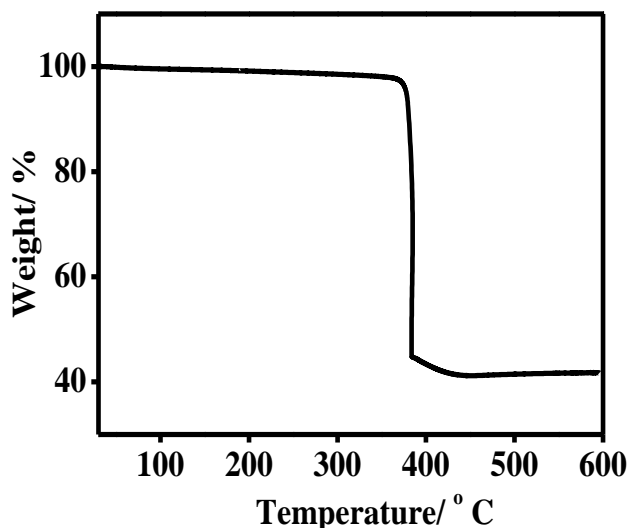
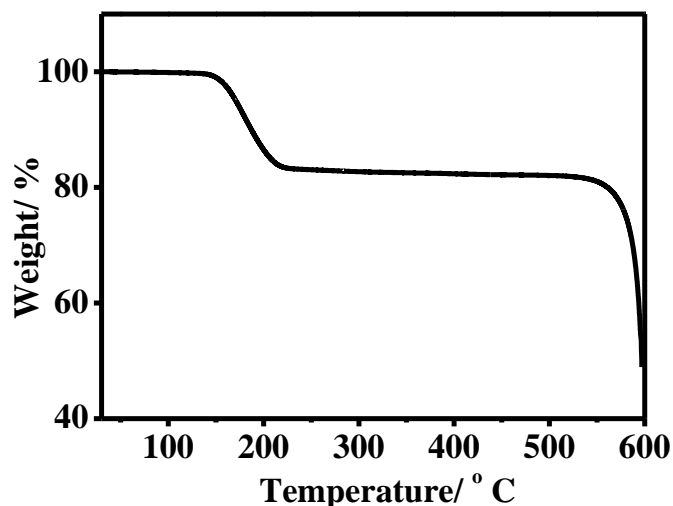**Figure 3.29**: TGA curve of Mn-BTEC

3.2.8.   Mn-Co-BTEC:

3.2.8.1.   PXRD Pattern:

PXRD was performed to check whether the material is phase pure or not. The obtained pattern gave all major peaks at 2θ= 9.17, 14.01, 18.68, 28.03, 29.34, 33.36.[5]
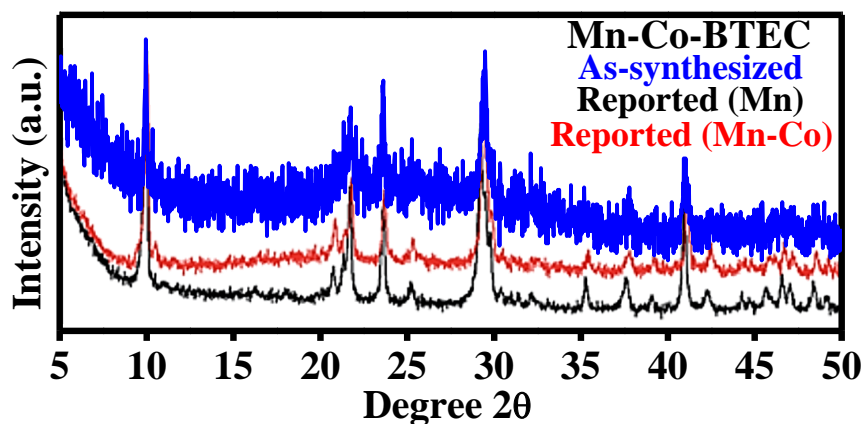
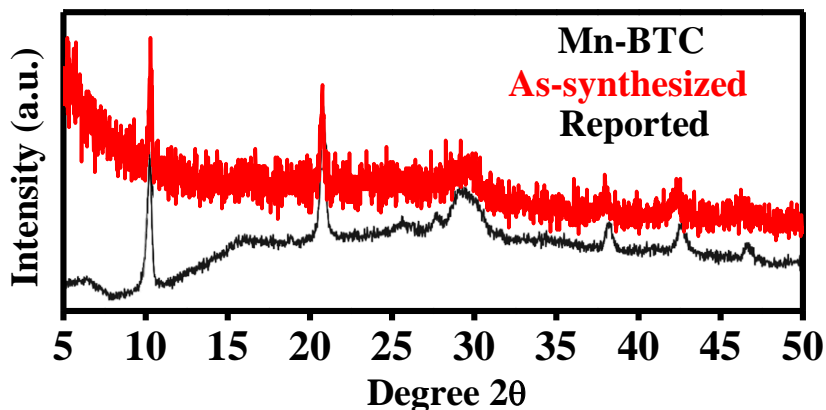**Figure 3.30**: PXRD pattern of Mn-Co-BTEC.

3.2.8.2. Infrared Spectrum:

IR spectroscopy data shows the binding pattern of DOT and the presence H_2O molecule in the framework. The peaks at 1714 cm^{-1} shifted to 1596 cm^{-1} due to metalation of carboxylic groups and corresponds to C=O stretching frequency.[6]
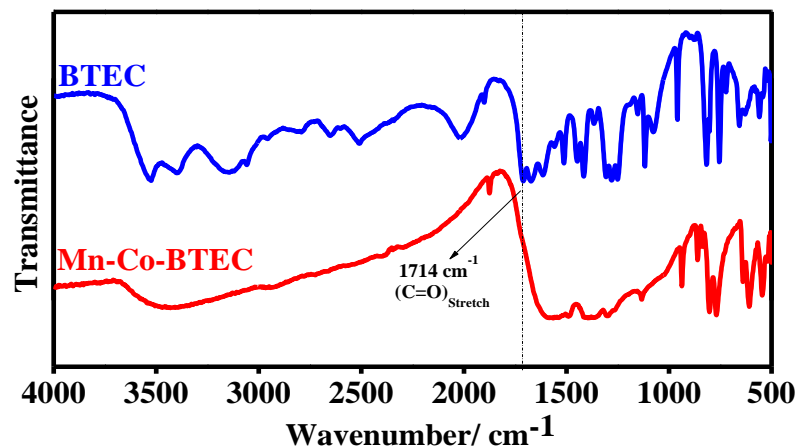
Figure 3.31: FT-IR spectra of Mn-Co-BTEC.

3.2.8.3. Thermogravimetric Analysis:

The TGA results revealed that the compound is stable up to 400 ℃. Weight loss of 6 % at around 100 ℃ corresponds to solvent molecule present in the framework. Again, overall weight loss of 64 % at around 400 ℃ accounts for the loss of BTEC molecule as well as the collapse of the framework.


Figure 3.32: TGA curve of Mn-Co-BTEC.

Reference:

(1)   Zhou, W.; Wu, H.; Yildirim, T. Enhanced H_2 Adsorption in Isostructural Metal−Organic Frameworks with Open Metal Sites: Strong Dependence of the Binding Strength on Metal Ions. *J. Am. Chem. Soc.* **2008**, *130*, 15268–15269.

(2)   Sundriyal, S.; Mishra, S.; Deep, A. Study of Manganese-1,4-Benzenedicarboxylate Metal Organic Framework Electrodes Based Solid State Symmetrical Supercapacitor. *Ener. Proc.* **2019**, *158*, 5817–5824.

(3)   Ladrak, T.; Smulders, S.; Roubeau, O.; Teat, S. J.; Gamez, P.; Reedijk, J. Manganese-Based Metal-Organic Frameworks as Heterogeneous Catalysts for the Cyanosilylation of Acetaldehyde. *Eur. J. Inorg. Chem.* **2010**, *2010*, 3804–3812.

(4)   Fu, Y.; Su, J.; Yang, S.; Li, G.; Liao, F.; Xiong, M.; Lin, J. Syntheses, Structures and Magnetic Properties of Mn(II), Co(II) and Ni(II) Metal–Organic Frameworks Constructed from 1,3,5-Benzenetricarboxylate and Formate Ligands. *Inorganica Chim. Acta* **2010**, *363*, 645–652.

(5)   Li, T.; Li, C.; Hu, X.; Lou, X.; Hu, H.; Pan, L.; Chen, Q.; Shen, M.; Hu, B. Reversible Lithium Storage in Manganese and Cobalt 1,2,4,5-Benzenetetracarboxylate Metal-Organic Framework with High Capacity. *RSC Adv.* **2016**, *6*, 61319–61324.

(6)   Ismail, A. A.; van de Voort, F. R.; Sedman, J. Chapter 4 Fourier Transform Infrared Spectroscopy: Principles and Applications. *Tech. Instrum. Anal. Chem.* **1997**, *18*, 93–139.

(7)   Yuan, K.; Song, T.; Wang, D.; Zou, Y.; Li, J.; Zhang, X.; Tang, Z.; Hu, W. Bimetal–Organic Frameworks for Functionality Optimization: MnFe-MOF-74 as a Stable and Efficient Catalyst for the Epoxidation of Alkenes with H 2 O 2. *Nanoscale* **2018**, *10*, 1591–1597.

(8)   Xiao, T.; Liu, D. The Most Advanced Synthesis and a Wide Range of Applications of MOF-74 and Its Derivatives. *Micro. Meso. Mater.* **2019**, *283*, 88–103.

(9)   Adpakpang, K.; Pratanpornlerd, W.; Ponchai, P.; Tranganphaibul, W.; Thongratkaew, S.; Faungnawakij, K.; Horike, S.; Siritanon, T.; Rujiwatra, A.; Ogawa, M.; Unsaturated Mn(II)-Centered [Mn(BDC)]$_n$ Metal–Organic Framework with Strong Water Binding Ability and Its Potential for Dehydration of an Ethanol/Water Mixture. *Inorg. Chem.* **2018**, *57*, 13075–13078.

(10) Maiti, S.; Pramanik, A.; Mahanty, S. Electrochemical Energy Storage in Mn2O3 Porous Nanobars Derived from Morphology-Conserved Transformation of Benzenetricarboxylate-Bridged Metal-Organic Framework. *Cryst. Eng. Comm.* **2016**, *18*, 450–461.

(11) Wu, Y.; Song, X.; Li, S.; Zhang, J.; Yang, X.; Shen, P.; Gao, L.; Wei, R.; Zhang, J.; Xiao, G. 3D-Monoclinic M–BTC MOF (M = Mn, Co, Ni) as Highly Efficient Catalysts for Chemical Fixation of CO_2 into Cyclic Carbonates. *J. Ind. Eng. Chem.* **2018**, *58*, 296–303.

Chapter IV

Properties

Chapter IV

Properties

In this chapter, we will discuss about the different properties observed in the synthesized coordination polymers. Here we performed sorption isotherms, thermal stability tests, magnetic analysis, post-synthetic modifications and the electrochemistry of CP derived metal oxides.

4.1. Sorption Analysis:

We have performed adsorption-desorption analysis to determine the BET surface are of the molecules, pore size distribution, etc. The BET surface area for Mn-SKU-1 and Mn-SKU-2 are 72 m^2g^{-1} and 34 m^2g^{-1} respectively and the Langmuir surface area are 315 m^2g^{-1} and 145 m^2g^{-1}. The adsorption isotherm graphs are given in *figure 4.1*. The curves obtained corresponds to the presence of type IV(a) isotherm which usually comes for mesoporous materials. The formation of hysteresis loops during degassing typically occurs when pore width exceeds critical width and capillary condensation occurs[1,2].
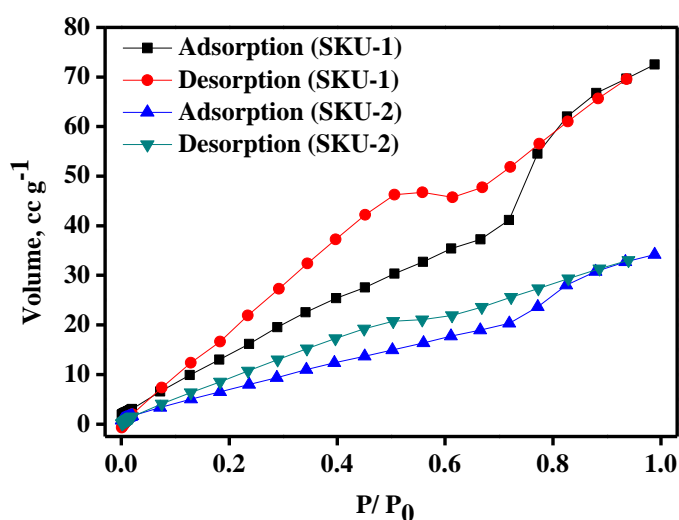
Figure 4.1: Adsorption isotherm of Mn-SKU-1 and Mn-SKU-2.

Properties

The low surface observed were due to small pore size present in Mn-SKU-1 and high interpenetration in Mn-SKU-2 (*figure 4.2(a)-4.2(b)*). BJH pore size distribution graph shows the highest volume occupation at a pore radius of 4.1 nm and 4.2 nm respectively for Mn-SKU-1 and Mn-SKU-2 which comes under the category of mesoporous materials (*figure 4.3(a)-4.3(b)*). The pores available in the Mn-SKU-1 framework with width of 3.76 Å & 7.71 Å (*figure 4.2(a) & figure 3.3(c)*). Again, despite being a rigid cubic framework in Mn-SKU-2, the presence of high degree of interpenetration (*figure 4.2(b)*) prevents the pore filling with the N_2 molecules resulting in low surface area.
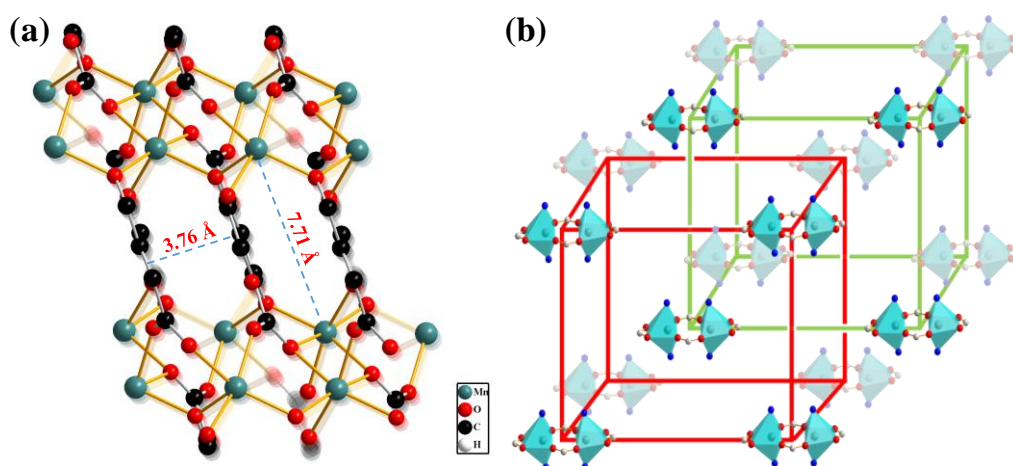
Figure 4.2: (a) Available pores in Mn-SKU-1 & (b) interpenetration in Mn-SKU-2.

Table 4.1: BET surface area of all the synthesized Mn-CPs.

Sl. No	Coordination Polymer	Surface Area ($m^2 g^{-1}$)
1	Mn-MOF-74	145.84
2	Mn-BDC	114.52
3	Mn-TPA-DMF	358.32
4	Mn-BTC	118.83
5	Mn-BTEC	58.87
6	Mn/Co-BTEC	59.44
7	**Mn-SKU-1**	**76.84**
8	**Mn-SKU-2**	**34.38**
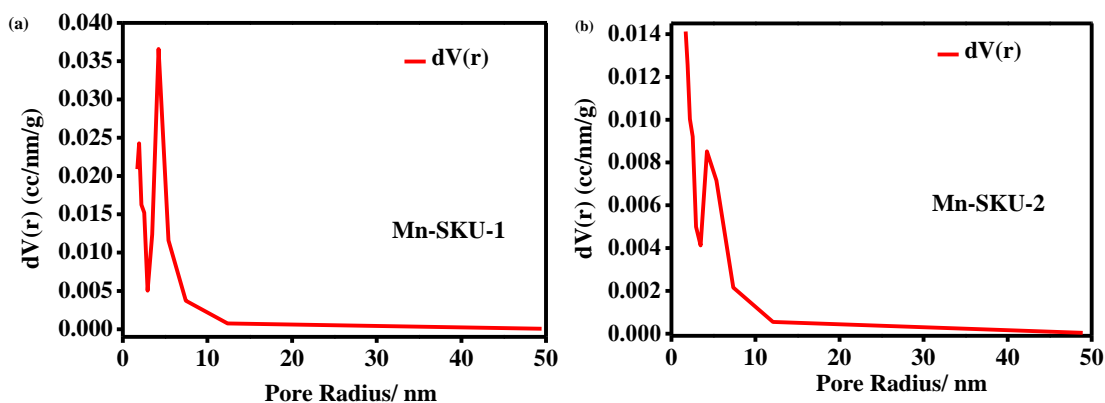
Figure 4.3: BJH pore size distribution of (a) Mn-SKU-1 and (b) Mn-SKU-2.

4.2.   Thermal Stability:

Thermal stability is also a very important point of interest for CPs. Higher thermal stability opens a window for application in different field where high thermal stability is necessary as it helps in protecting the structural integrity when the compounds are treated with elevated heat, vacuum or pressure. Therefore, to check whether the synthesized compounds are stable in high temperature or not, we performed TGA analysis for all the Mn-CPs (*figure 4.4 & 4.5(a)-(b)*).
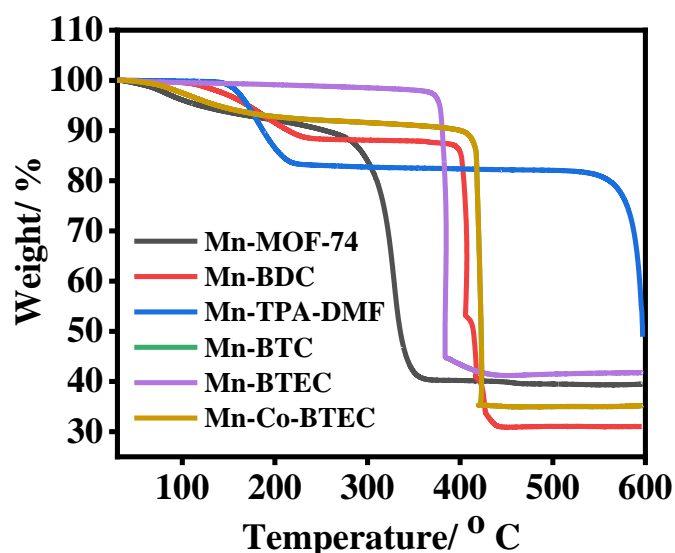
Figure 4.4: TGA graph of all Mn-CPs.

From the TGA data, it's observed that the compounds don't degrade till ~300 °C which clarifies the high bond strength and high framework stability of all the synthesized CPs. In case of Mn-SKU-1, a weight loss near 180-200 °C was observed due to removal of

two coordinated water molecules (*figure 4.5(a)*). Further decomposition of the material takes place at 290 °C collapsing the framework. No weight loss near 180 °C was observed due which can be attributed as absence of any water molecule coordinated to the framework. However, the Mn-SKU-2 framework starts decomposing at ~300 °C (*figure 4.5 (b)*). The thermal stability of both the materials are comparable to the other synthesized CPs and can be concluded to have a robust structure which will facilitate high temperature, pressure and vacuum applications.
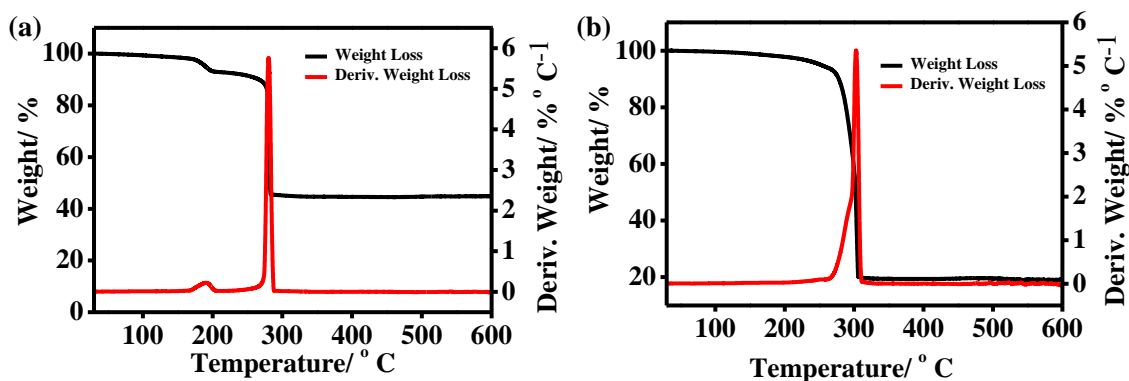
Figure 4.5: TGA graph of (a) Mn-SKU-1 & (b) Mn-SKU-2.

Table 4.2: Table of thermal stabilities of all Mn-CPs.

Sl. No.	Coordination Polymer	Thermal Stability (°C)
1	Mn-MOF-74	290
2	Mn-BDC	400
3	Mn-TPA-DMF	550
4	Mn-BTC	405
5	Mn-BTEC	390
6	Mn/Co-BTEC	410
7	**Mn-SKU-1**	**280**
8	**Mn-SKU-2**	**290**

4.3. Magnetic Analysis:

Temperature dependent magnetic susceptibility measurement were carried out for both the powdered polycrystalline compounds. The magnetization measurements (both FC and ZFC) were carried out under applied magnetic field of 100 Oe and temperature 5

Properties

K. Whereas the field dependent isothermal magnetization was investigated in the range -60 kOe to 60 kOe at temperature 5 K. The single crystal data refers to the presence of Mn(II) centers in both the compounds which are interlinked by DOT and 4,4'-BPY ligands.

Mn-SKU-1: Here the measured $\chi_M T$ value at 300 K is 7.83 emu K mol^{-1} which is nearly equal to the calculated effective moment 7.92 emu K mol^{-1} ($\mu_{eff} = 2.83\sqrt{\chi_M T}$) for a complex consisting of Mn(II) centers.[3] As the temperature is lowered, the $\chi_M T$ value gradually decreases, reaches a minimum value of 1.05 emu K mol^{-1} at 11.42 K. A sudden increase in $\chi_M T$ value was observed with a maximum value of 1.40 emu K mol^{-1} at 8.36 k (*figure 4.6*). On further cooling, the $\chi_M T$ value finally decreases to a lowest value of 1.03 emu K mol^{-1} at 4.20 K.
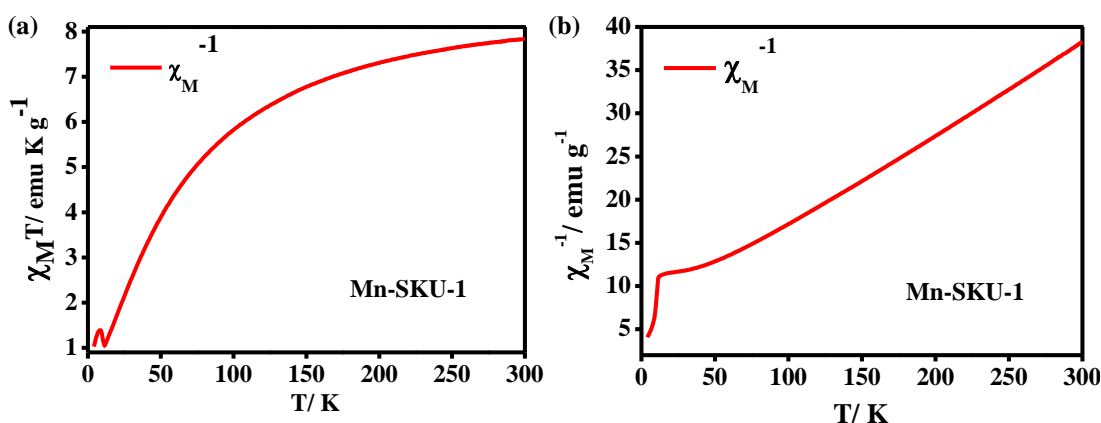
Figure 4.6: (a) $\chi_M T$ *vs.* T & **(b)** χ_M^{-1} *vs.* T curve for Mn-SKU-1.

The unusual magnetic behavior seen in the range of 8-11 K can be referred to the presence of a short range antiferromagnetic ordering which is arising due to canting of spins of interacting metal centers of 2D layers.[4] The plot of χ_M^{-1} *vs.* T curve was fitted with Curie-Weiss Law ($\chi_M = \frac{c}{(T - \theta)}$) and the best-fitting data in the range of 50 K - 300 K gave C= 9.708 emu K mol^{-1} and θ= -67.19 K.[5] The high order negative value of θ also indicates the presence of strong antiferromagnetic interaction (J_1 & J_2) (*figure 4.7*) between neighboring Mn(II) centers.[6,7] The anomaly in the magnetic behavior in low temperature region indicates the contribution of uncompensated residual spin moments

and existence of very weak ferromagnetic ordering. This weak ferromagnetism is referred as spin canting where the antiferromagnetically coupled spins aligns in a distorted manner producing uncompensated residual spin moments.[8]
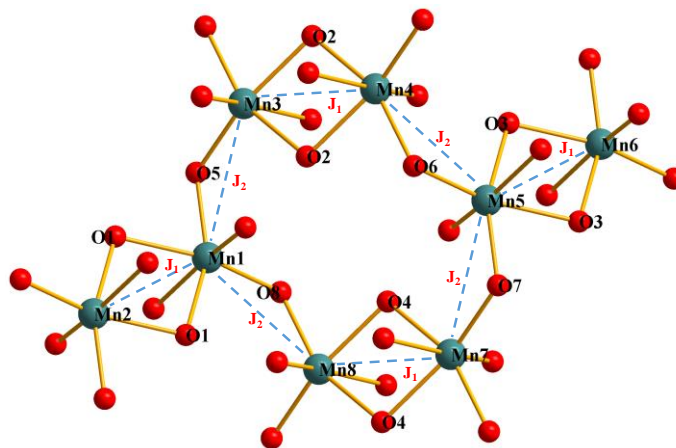
Figure 4.7: Possible magnetic interactions between the metal centers in Mn-SKU-1.

To confirm the presence of spin canting or canted antiferromagnetism, field-dependent isothermal magnetization measurement was performed below 5 K. The M *vs.* H curve showed a linear increase in magnetization from 0 to 70 kOe reaching a maximum effective moment of 0.0029 emu Oe^{-1} g^{-1}. Here the M/H curve maintains a linearity without a saturation point until it reaches the maximum applied magnetic field (*figure 4.8*).
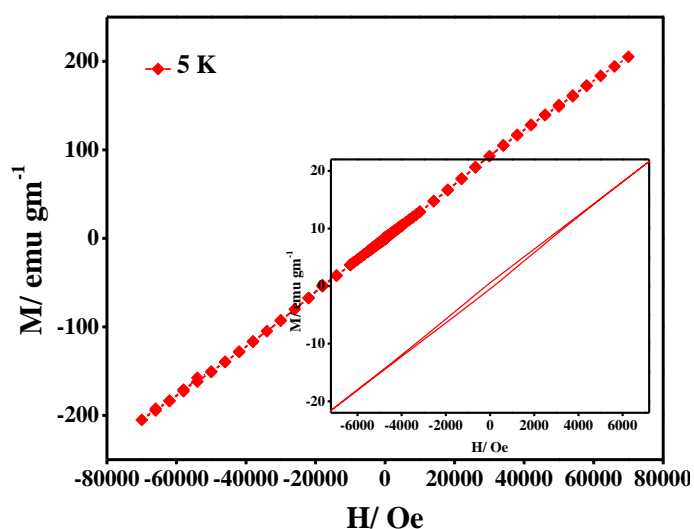
Figure 4.8: Magnetization (M) vs. applied magnetic field (H) curve for Mn-SKU-1

In low applied magnetic field region (0 to ±6 kOe), a distinct hysteresis loop was observed. The loop gives a remanence of 0.55 emu g^{-1} and a coercive field of 183.05 Oe. The Zero Field Cooled (ZFC) and Field Cooled (FC) analysis also supports the presence of spin canted antiferromagnetism (*figure 4.9*). The deviation of FC curve from ZFC curve below 12 K indicates the formation of short-range magnetic ordering.
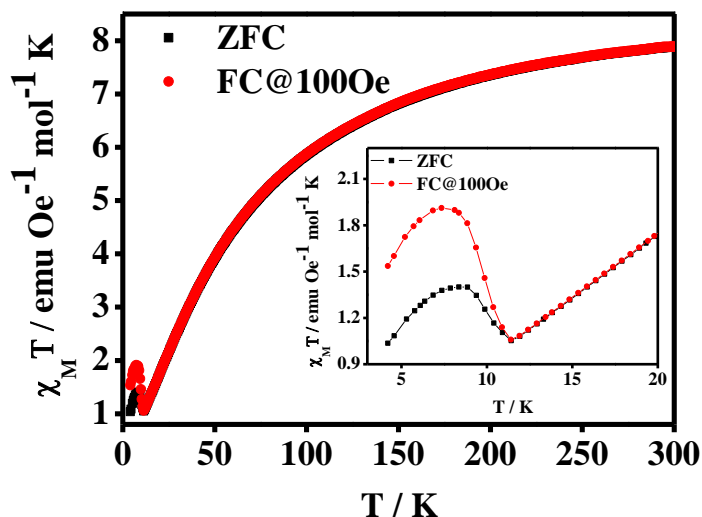
Figure 4.9: ZFC & FC curve for Mn-SKU-1 (Inset: $\chi_M T$ *vs.* T curve between 4-20 K).

From all the experimental evidences given above, it can be concluded that Mn-SKU-1 framework shows a spin canted antiferromagnetic behavior arising where the spins aligns in slightly distorted fashion.

Mn-SKU-2: Here the measured $\chi_M T$ value at 300 K is 6.04 emu K mol^{-1} which is somewhat lower to the calculated effective moment 6.96 emu K mol^{-1} ($\mu_{eff} = 2.83\sqrt{\chi_M T}$) for a complex consisting of Mn(II) centers.[3] As the temperature is lowered, the $\chi_M T$ value linearly decreases and reaches a minimum value of 1.03 emu K mol^{-1} at 4.2 K (*figure 4.10*).
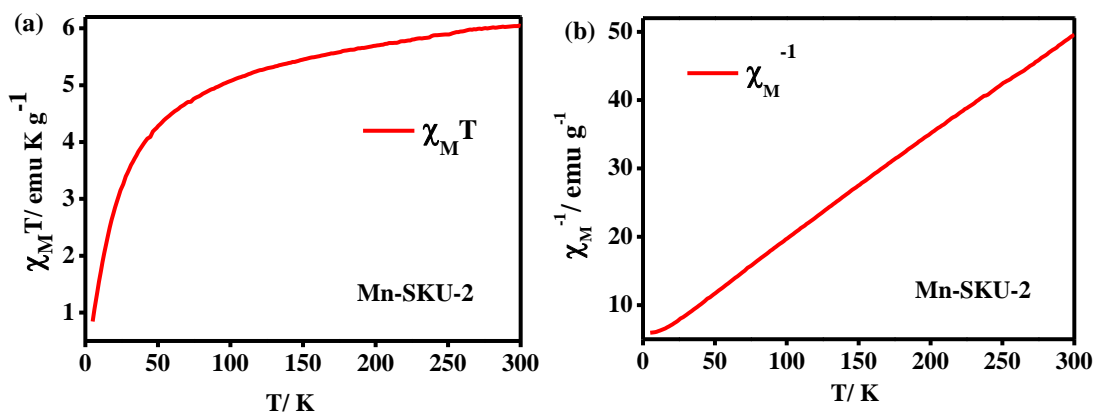
Figure 4.10: (a) $\chi_M T$ vs. T & **(b)** χ_M^{-1} vs. T curve for Mn-SKU-2.

Here also the plot of χ_M^{-1} *vs.* T curve was fitted with Curie-Weiss Law ($\chi_M = \frac{c}{(T - \theta)}$). The best-fitting data in the range of 50 K - 300 K gave C= 6.578 emu K mol^{-1} and θ= -29.06 K. The high order negative value of θ also indicates the presence of antiferromagnetic interaction (J) between neighboring Mn(II) centers (*figure 4.11 (a)-(b)*).
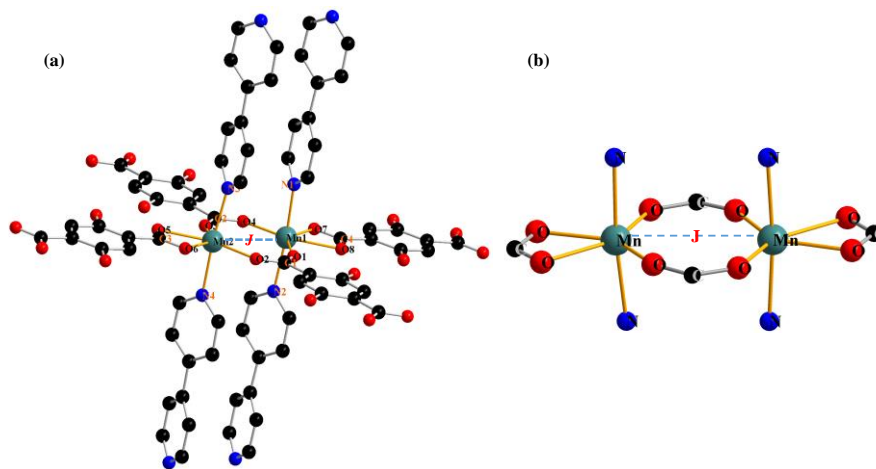
Figure 4.11: (a) & (b) Possible magnetic interactions in between the metal centers in Mn-SKU-2.

We have also performed the field-dependent isothermal magnetization measurement below critical temperature (at 5 K). The M *vs.* H curve showed a linear increase in magnetization from 0 to 70 kOe reaching a maximum effective moment of 6.32 emu K mol^{-1} (*figure 4.12*).
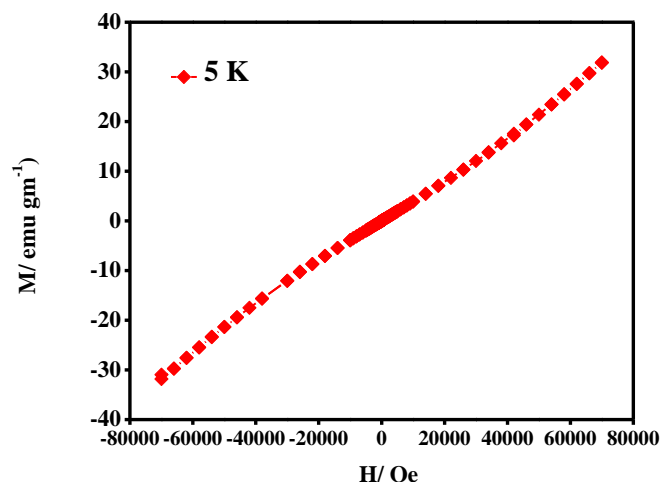
Figure 4.12: Magnetization (M) vs. applied magnetic field (H) curve for Mn-SKU-2.

There is no hysteresis loop observed in this case. The Zero Field Cooled (ZFC) and Field Cooled (FC) also shows a parallel curve which tends to absence of any ferromagnetic character like in Mn-SKU-1. The kind of behavior might be arising due to the inertness of stable Mn(II) centers which are not getting affected by the influence of external magnetic field.

4.4.   Post-synthetic Modification:

From the diverse possibilities of post-synthetic modifications of CPs, we have performed chemical activation of metal centers by exchanging coordinated water molecules with acetonitrile[9–11]. Water molecules acts as an inhibitor in various catalytic reactions and coordinated water molecules are very difficult to remove. Thus, to use our compounds in different catalytic reactions, we tried to exchange the coordinated water with acetonitrile which can easily be removed later. Mn-SKU-1 was refluxed in dry CH_3CN for 48 h in inert atmosphere (*figure 4.13*). The brown coloured compound turned into a green coloured product after reflux.
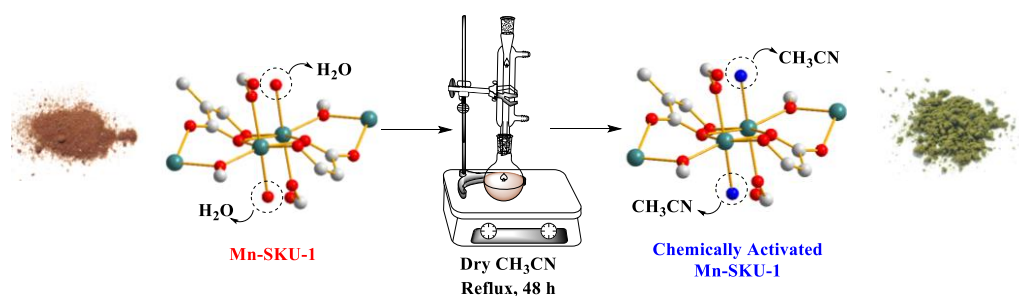
Figure 4.13: Scheme for chemical activation of Mn-SKU-1.

To confirm the exchange of water with acetonitrile, we performed FT-IR and TGA for the same (*figure 4.14 (a) & (b)*). In FT-IR spectra, the peak near 3200-3600 cm^{-1} vanishes and a new peak at 2250 cm^{-1} arises in the case of chemically activated product due to presence of C=N symmetric stretching mode.[12] Again, from the TGA curve, it's clearly observed that the peak for coordinated water near 180-200 °C vanishes which confirms the successful exchange of water with acetonitrile.
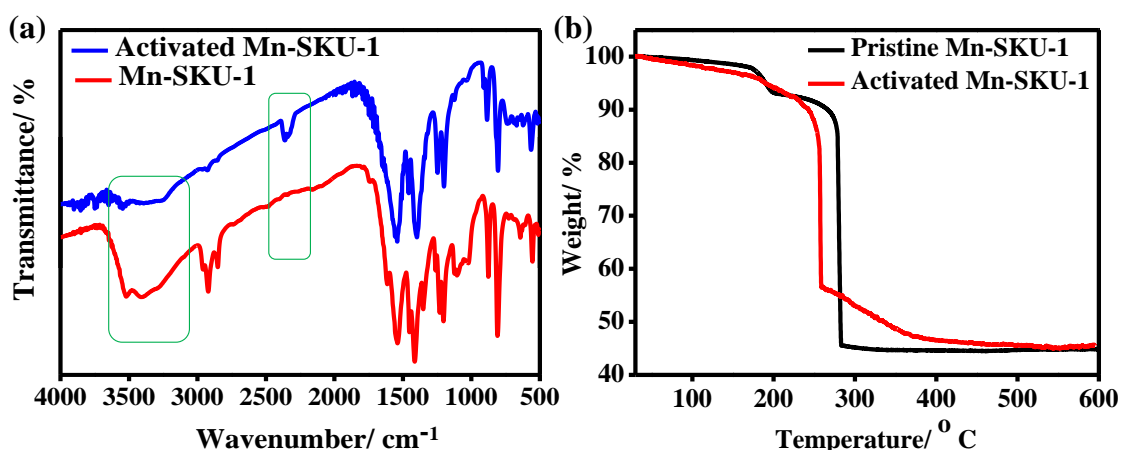
Figure 4.14: (a) FT-IR spectra & (b) TGA graph of chemically activated Mn-SKU-1.

4.5.   CP derived Metal Oxides (MO):

To study the ORR reactivities by transition metal oxides, CP derived metal oxides are the best candidates due to controllable porosity, crystallinity, high surface area of the templates.[13–16] The as-synthesized Mn-CP were pyrolyzed in N_2 environment. The compounds were heated to 600 °C (at rate of 10 °C min^{-1}) and kept at 600 °C for 30 min with N_2 supply (60 mL min^{-1}) (*figure 4.15*). The black coloured product obtained after pyrolysis were stored for further characterization.
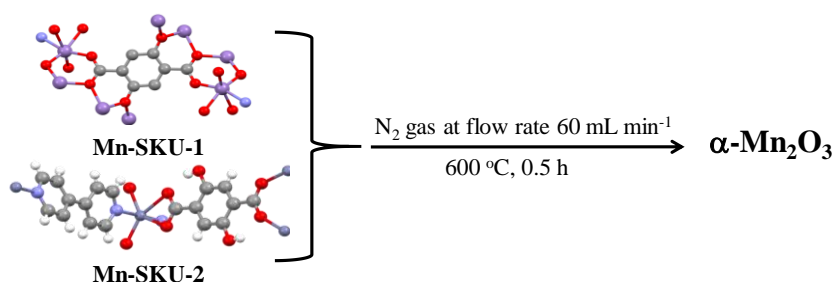
Figure 4.15: Scheme for pyrolysis of Mn-CPs.

The PXRD analysis was performed for the products obtained after pyrolysis. Comparison of the XRD patterns with the reference pattern (JCPDS- 96-810-3498) confirms the formation of α-Mn_2O_3 (*figure 4.16*). All the peaks present in both the samples are matching well with the reference patterns which confirms the full transformation of Mn-CPs into α-Mn_2O_3. [17]
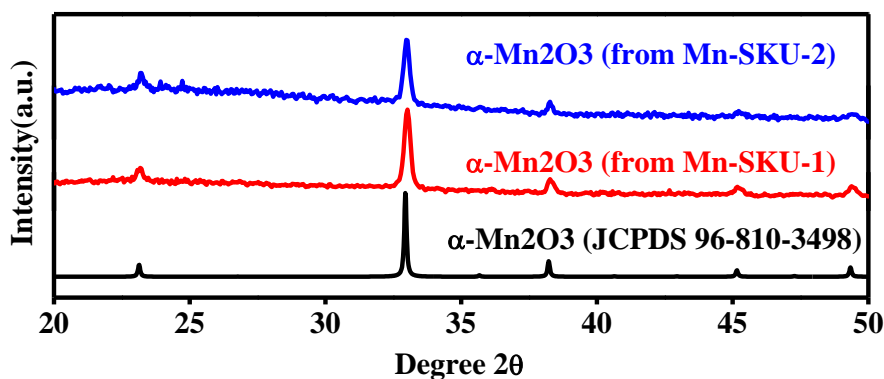
Figure 4.16: Compared PXRD patterns of α-Mn_2O_3 (obtained & reported).

The adsorption isotherm analysis of the α-Mn_2O_3 derived from the as-synthesized Mn-CPs gave BET surface area of 90 m^2g^{-1} and 179 m^2g^{-1} from Mn-SKU-1 and Mn-SKU-2 respectively (*figure 4.17*). The BET surface area obtained in this study for α-Mn_2O_3 derived from Mn-CPs are far higher than the reported of maximum 44 m^2g^{-1}.[18] This might be due to preservation of morphology similar to the morphology of parent CP.[13]
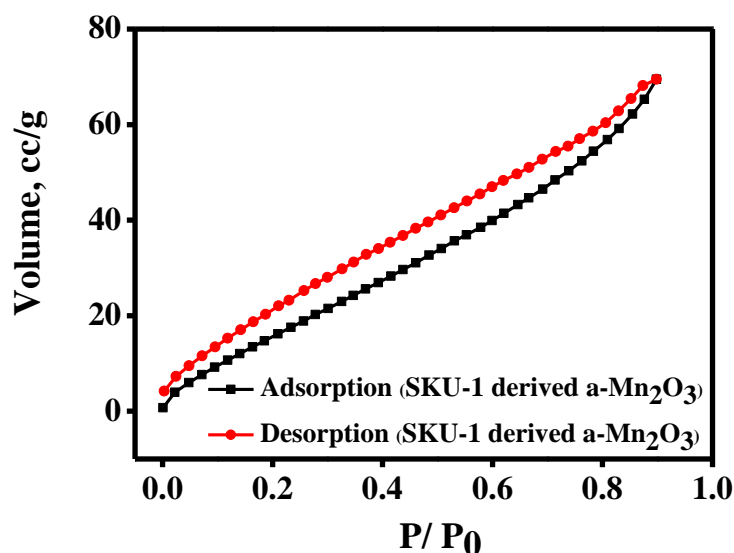
Figure 4.17: Sorption Isotherm for α-Mn_2O_3 derived from Mn-CPs.

Table 4.3: Some previously reported Mn_2O_3 materials and the respective surface area.

Sample	SA (m²/g)	Reference for Mn_2O_3	Parent MOF	Parent MOF SA	Reference for parent MOF
Mn_2O_3	35.15	*Chem. Eur. J.* **2016**, *22*, 9909-9913	-	-	-
Cubic Mn_2O_3	116 (Mn_2O_3/C)	*Mol. Cat.* **2018**, *451*, 153-160	-	-	-
Pure α-Mn_2O_3	23.1	*Cat. Sci. Technol.* **2018**, *8*, 1905-1914	-	-	
α-Mn_2O_3-10R	38.5	*RSC Adv.* **2016**, *6*, 93532–93538	Mn-BTC	24.97	*J. Ind. and Eng. Chem.* **2018**,*58*, 296–303
α-Mn_2O_3	44	*Cryst. Eng. Comm.* **2016**, *18*, 450–461	Mn-BTC	23.8	*ACS Appl. Mat. Inter.* **2015**, *7*, 16357−16363
Octahedral-Mn_2O_3	40.4	*Mat. and Des.* **2016**, *98*, 319–323	Mn-MIL-100	1410	*Cryst. Eng. Comm.* **2013**, *15*, 544–550
α-Mn₂O₃	**90.8**	**This Work**	**Mn-SKU-1**	**76.84**	**This Work**
α-Mn₂O₃	**179**	**This Work**	**Mn-SKU-2**	**34.38**	**This Work**

4.6. Oxygen Reduction Reaction (ORR) using CP derived MOs:

The Oxygen Reduction Reaction activities of the CP derived α-Mn_2O_3 were investigated by performing cyclic voltammetry, LSV and RRDE measurements. Since, from the PXRD data, it's clear that both the CPs produces α-Mn_2O_3, thus further study of ORR activities were performed for α-Mn_2O_3 derived from Mn-SKU-1 only. The working electrodes were first cleaned by polishing using a drop of diamond polish on a microcloth disk glass plate. A slurry of electrocatalyst were prepared by taking the 0.005 g of α-Mn_2O_3 with 0.5 mL ethanol and 0.02 mL 5 wt. % nafion. 0.02 mL of the slurry were then applied to the GC and RRD-GC-electrodes by drop casting method and left for drying. 10 mL of 0.1 M KOH solution was saturated with N_2 and O_2 before performing CV. The CV curve in presence of N_2 gas showed no significant peak (*figure 4.18*). Again, the CV curve after purging O_2 for 30 min gave a significant peak at 0.66 V (*vs.* R.H.E.) with a current density of -0.39 mA cm⁻² and the onset potential of 0.85 V (*vs.* R.H.E.).
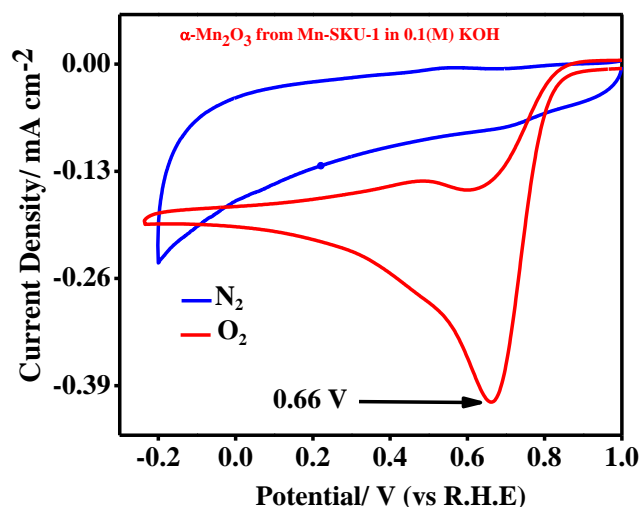
Figure 4.18: CV curves of α-Mn$_2$O$_3$ derived from Mn-SKU-1.

Further to confirm the ORR kinetics, we performed RDE analysis for quantitative determination of ring current as well as the production H$_2$O$_2$. The RRDE was loaded using drop casting method same as above. Again, prior to analysis, 0.1 M KOH was prepared and saturated with N$_2$ and O$_2$. The RDE measurements were taken at different rotations- 400, 625, 900, 1225, 1600, 2025 & 2500 RPM with a scan rate of 50 mV sec^{-1}. The sample shows an excellent onset potential at 0.85 V (*figure 4.19(a)*) which is analogous to the previously reported onset potential for Mn$_2$O$_3$ (0.85), MnO$_2$ (0.80 V), Mn$_3$O$_4$ (0.69 V) and Pt/C (0.87 V).[19–21] The overall transfer of electrons per oxygen molecule were determined by plotting the LSV data in Koutecky-Levich (K-L) plot (*figure 4.19(b)*) and the slopes obtained were manipulated in a simplified K-L equation to get the results.[22,23]

Koutecky-Levich equation:

$$\frac{1}{J} = \frac{1}{0.62nFC_0D^{2/3}v^{-1/6}\omega^{1/2}} + \frac{1}{nFkC_0}$$

where ω is the angular velocity, n is the number of electrons transferred, F is Faraday's constant, C_0 is the concentration of dissolved oxygen (1.2×10^{-6} mol cm^{-3}), D is the diffusion coefficient of oxygen (1.9×10^{-5} cm^2 s^{-1}), v is the kinetic viscosity of solution and k is the apparent electron transfer rate constant.[22,23]

Properties

From the K-L plot, a parallel fitting of all the straight lines at different potential indicates the kinetics of the reaction going in first order throughout the ORR response[24]. The average number of electrons transferred was calculated to be n=3.98 which is in favor of 4 electron transfer mechanism.[25]

$$n = \frac{4I_d}{I_d + {I_r}/{N}}$$

where, I_d = Disk current,

Ir = Ring current

$$O_2 + 4H^+ + 4e^{-1} \rightarrow H_2O$$
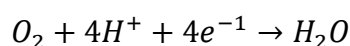
The production of H₂O₂ were measured by performing RRDE measurements within the range of 0 to -0.8 V (*vs.* RHE) and it was found to be 0.98 % which shows the 4 e⁻ transfer process towards the ORR.

$$\%(HO_2)^- = \frac{200I_r/N}{I_d + I_r/N}$$
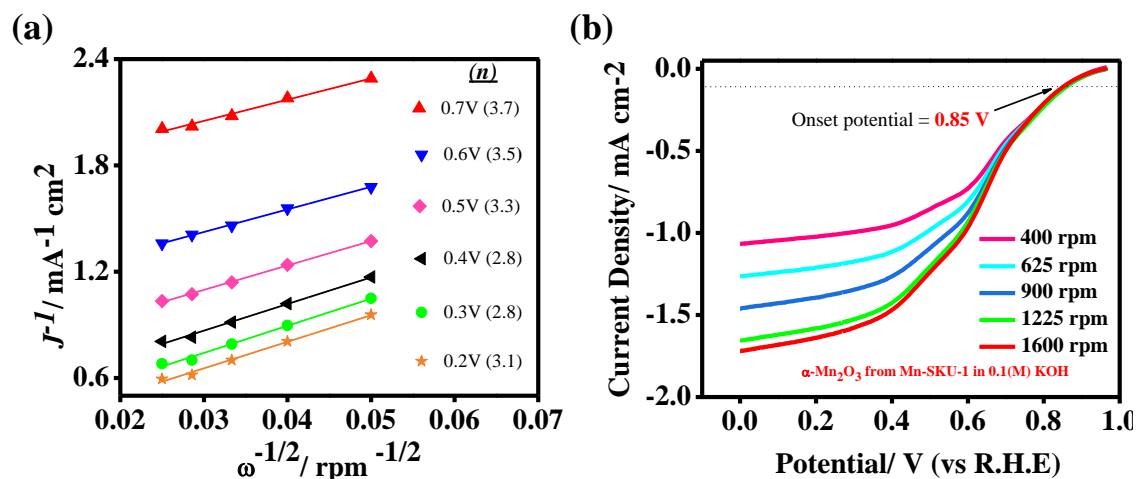
Figure 4.19: (a) LSV curves and (b) K-L plots of α-Mn₂O₃ derived from Mn-SKU-1.

References:

(1) Sing, K. S. W.; Everett, D. H.; Haul, R. A. W.; Moscou, L.; Pierotti, R. A.; Rouquerol, J.; Seimieniewska, T. Reporting Physisorption Data For Gas/Solid Systems with Special Reference to the Determination of Surface Area and Porosity; *Pure and Applied Chemistry* **1985**, *57*, 603-619.

(2) Thommes, M.; Kaneko, K.; Neimark, A. V.; Olivier, J. P.; Rodriguez-Reinoso, F.; Rouquerol, J.; Sing, K. S. W. Physisorption of Gases, with Special Reference to the Evaluation of Surface Area and Pore Size Distribution (IUPAC Technical Report). *Pure Appl. Chem.* **2015**, *87*, 1051–1069.

(3) Hoppe, J. I. Effective Magnetic Moment. *J. Chem. Educ.* **1972**, *49*, 505.

(4) Weng, Z.; Chen, Z.; Liang, F. Glycine-Templated Manganese Sulfate with New Topology and Canted Antiferromagnetism. *Inorg. Chem.* **2009**, *48*, 8703–8708.

(5) Gupta, K.; Dadwal, A.; Rana, S.; Jha, P. K.; Jain, A.; Yusuf, S. M.; Joy, P. A.; Ballav, N. Metamagnetism in Nanosheets of Co II -MOF with T N at 26 K and a Giant Hysteretic Effect at 5 K. *Inorg. Chem.* **2018**, *57*, 15044–15047.

(6) Ashafaq, M.; Khalid, M.; Raizada, M.; Ali, A.; Faizan, M.; Shahid, M.; Ahmad, M.; Butcher, R. J. Crystal Engineering and Magnetostructural Properties of Newly Designed Azide/Acetate-Bridged Mn 12 Coordination Polymers. *Cryst. Growth Des.* **2019**, *19*, 2366–2379.

(7) Wang, Y. Q.; Jia, Q. X.; Wang, K.; Cheng, A. L.; Gao, E. Q. Diverse Manganese(II) Coordination Polymers with Mixed Azide and Zwitterionic Dicarboxylate Ligands: Structure and Magnetic Properties. *Inorg. Chem.* **2010**, *49*, 1551–1560.

(8) Gao, E. Q.; Cheng, A. L.; Xu, Y. X.; He, M. Y.; Yan, C. H. From Low-Dimensional Manganese(II) Azido Motifs to Higher-Dimensional Materials: Structure and Magnetic Properties. *Inorg. Chem.* **2005**, *44*, 8822–8835.

(9) Wang, Z.; Cohen, S. M. Postsynthetic Modification of Metal–Organic

Frameworks. *Chem. Soc. Rev.* **2009**, *38*, 1315–1329.

(10) Yin, Z.; Wan, S.; Yang, J.; Kurmoo, M.; Zeng, M.-H. Recent Advances in Post-Synthetic Modification of Metal–Organic Frameworks: New Types and Tandem Reactions. *Coord. Chem. Rev.* **2019**, *378*, 500–512.

(11) McKellar, S. C.; Graham, A. J.; Allan, D. R.; Mohideen, M. I. H.; Morris, R. E.; Moggach, S. A. The Effect of Pressure on the Post-Synthetic Modification of a Nanoporous Metal–Organic Framework. *Nanoscale* **2014**, *6*, 4163–4173.

(12) Ennis, C.; Auchettl, R.; Ruzi, M.; Robertson, E. G. Infrared Characterisation of Acetonitrile and Propionitrile Aerosols under Titan's Atmospheric Conditions. *Phys. Chem. Chem. Phys.* **2017**, *19*, 2915–2925.

(13) Salunkhe, R. R.; Kaneti, Y. V.; Yamauchi, Y. Metal-Organic Framework-Derived Nanoporous Metal Oxides toward Supercapacitor Applications: Progress and Prospects. *ACS Nano* **2017**, *11*, 5293–5308.

(14) Zheng, F.; Xu, S.; Yin, Z.; Zhang, Y.; Lu, L. Facile Synthesis of MOF-Derived Mn_2O_3 Hollow Microspheres as Anode Materials for Lithium-Ion Batteries. *RSC Adv.* **2016**, *6*, 93532–93538.

(15) Li, Y.; Xu, Y.; Yang, W.; Shen, W.; Xue, H.; Pang, H. MOF-Derived Metal Oxide Composites for Advanced Electrochemical Energy Storage. *Small* **2018**, *14*, 1704435.

(16) Wu, H. Bin; Lou, X. W. Metal-Organic Frameworks and Their Derived Materials for Electrochemical Energy Storage and Conversion: Promises and Challenges. *Sci. Adv.* **2017**, *3*, 1–17.

(17) Ashoka, S.; Chithaiah, P.; Tharamani, C. N.; Chandrappa, G. T. Synthesis and Characterisation of Microstructural α-Mn_2O_3 Materials. *J. Exp. Nanosci.* **2010**, *5*, 285–293.

(18) Maiti, S.; Pramanik, A.; Mahanty, S. Electrochemical Energy Storage in Mn_2O_3 Porous Nanobars Derived from Morphology-Conserved Transformation of Benzenetricarboxylate-Bridged Metal-Organic Framework. *CrystEngComm* **2016**, *18*, 450–461.

(19)   Wang, W.; Geng, J.; Kuai, L.; Li, M.; Geng, B. Porous Mn_2O_3 : A Low-Cost Electrocatalyst for Oxygen Reduction Reaction in Alkaline Media with Comparable Activity to Pt/C. *Chem. - A Eur. J.* **2016**, *22*, 9909–9913.

(20)   Hazarika, K. K.; Goswami, C.; Saikia, H.; Borah, B. J.; Bharali, P. Cubic Mn_2O_3 Nanoparticles on Carbon as Bifunctional Electrocatalyst for Oxygen Reduction and Oxygen Evolution Reactions. *Mol. Catal.* **2018**, *451*, 153–160.

(21)   Jahan, M.; Tominaka, S.; Henzie, J. Phase Pure α-Mn_2O_3 Prisms and Their Bifunctional Electrocatalytic Activity in Oxygen Evolution and Reduction Reactions. *Dalt. Trans.* **2016**, *45*, 18494–18501.

(22)   Liu, R.; Wu, D.; Feng, X.; Müllen, K. Nitrogen-Doped Ordered Mesoporous Graphitic Arrays with High Electrocatalytic Activity for Oxygen Reduction. *Angew. Chemie* **2010**, *122*, 2619–2623.

(23)   Jahan, M.; Bao, Q.; Loh, K. P. Electrocatalytically Active Graphene–Porphyrin MOF Composite for Oxygen Reduction Reaction. *J. Am. Chem. Soc.* **2012**, *134*, 6707–6713.

(24)   Hazarika, K. K.; Goswami, C.; Saikia, H.; Borah, B. J.; Bharali, P. Cubic Mn_2O_3 Nanoparticles on Carbon as Bifunctional Electrocatalyst for Oxygen Reduction and Oxygen Evolution Reactions. *Mol. Catal.* **2018**, *451*, 153–160.

(25)   Wang, W.; Geng, J.; Kuai, L.; Li, M.; Geng, B. Porous Mn_2O_3 : A Low-Cost Electrocatalyst for Oxygen Reduction Reaction in Alkaline Media with Comparable Activity to Pt / C. *Chem. Eur.J.* **2016**, *22*, 9909 –9913.

Chapter V

Conclusion & Future Perspective

Chapter V

Conclusion & Future Perspective

Herein, we successfully synthesized two novel Mn-based CPs and two of them were novel and six of them were previously reported by different research groups. Firstly, we synthesized all the materials and characterized them using SC-XRD, P-XRD, FT-IR and TGA. In addition to this, surface area of all the synthesized materials were measured using gaseous N_2 as adsorbate and the SA for SKU-1 was found to be 72 m^2g^{-1} while for SKU-2 was 34 m^2g^{-1}. Further, we continued to explore the magnetic properties and possible PSM of the CPs and also ORR activities of CP derived metal oxides. The magnetic measurements revealed that both the materials (SKU-1 & SKU-2) possesses antiferromagnetically coupled Mn-centers. However, in SKU-1, an anomaly in the temperature dependent magnetization measurement was observed with a sudden increase in $\chi_M T$ value from 1.04 emu K mol^{-1} to 1.39 emu K mol^{-1} near 12 K. Previous reports suggested that occurrence of this similar behavior can be attributed as an effect of canting of spins present within the antiferromagnetically coupled Mn-centers. In addition to this, deviation in ZFC-FC curves and small hysteresis loop in M/H curve confirms the presence of spin canting. For PSM, we tried to exchange the coordinated H_2O molecules with acetonitrile (CH_3CN) simply by refluxing the compound in inert atmosphere. The successful exchange of the H_2O molecules with CH_3CN was confirmed by FT-IR and TGA analysis. In FT-IR analysis, the H_2O peak vanishes and a peak near 2250 cm^{-1} appears which corresponds to C=N stretching. TGA data also supports this statement where the peak for coordinated H_2O molecules near 180-200 °C disappears. Apart from this, we pyrolyzed our compound in N_2 environment and P-XRD analysis of the resulted products validated them as α-Mn_2O_3. The surface area was observed up to ~179 m^2g^{-1} which the highest for all the synthesized α-Mn_2O_3 till date. ORR activities for the obtained α-Mn_2O_3 were monitored where we observed excellent ORR activities with onset potential of 0.85 V and current density of 0.39 mA g^{-1} which are comparable to the previously reported ORR using α-Mn_2O_3 and in also comparable to state-of-the-art Pt-

electrodes (0.88 V *vs.* R.H.E.). K-L plot suggested the reduction of oxygens are processing through 4 e$^-$ transfer reaction mechanism.

Contemplating the structural integrity, porosity, magnetic behavior and possible generation of PSM products, we conclude that both our materials (SKU-1 & SKU-2) can play crucial role for applications in the field of heterogeneous catalysis, superconductors, magnetism studies, etc. The removal of CH_3CN from post-synthetically modified SKU-1 framework can generate coordinatively unsaturated sited within the structure which can act as coordinating sites during catalysis. The exchange of linkers and metal centers, modification of functional groups are also possible *via* PSM which may open a path for different photoluminescent studies, magnetic and catalytic applications. In case of SKU-2, high level of interpenetration are creating complexities in obtaining high surface are and gas adsorption level. The removal of interpenetrating networks may also be deciphered *via* PSM as well as using bulky linkers or by changing solvent and reaction conditions. Apart from the pristine products, α-Mn_2O_3 obtained from pyrolysis of the CPs can further be studies in the field of supercapacitors, molecular catalysis and magnetic studies.

Bibliography

<u>Chapter I</u>

(1)   Garcia, Y.; Su, B. L. No Inorganic Materials, No Progress. *Eur. J. Inorg. Chem.* **2019**, *2019*, 3123–3125.

(2)   Osadchii, D. Y.; Olivos-Suarez, A. I.; Szécsényi, Á.; Li, G.; Nasalevich, M. A.; Dugulan, I. A.; Crespo, P. S.; Hensen, E. J. M.; Veber, S. L.; Fedin, M. V.; et al. Isolated Fe Sites in Metal Organic Frameworks Catalyze the Direct Conversion of Methane to Methanol. *ACS Catal.* **2018**, *8*, 5542–5548.

(3)   Periono, R. A.; Taube, D. J.; Gamble, S.; Taube, H.; Satoh, T.; Fujii, H.; Vlcek A., J. Platinum Catalysts for the High-Yield Oxidation of Methane to a Methanol Derivative. *Chemtracts* **1999**, *12*, 130–134.

(4)   Kim, R. S.; Surendranath, Y. Electrochemical Reoxidation Enables Continuous Methane-to-Methanol Catalysis with Aqueous Pt Salts. *ACS Cent. Sci.* **2019**, *5*, 1179–1186.

(5)   Periana, R. A.; Bhalla, G.; Tenn, W. J.; Young, K. J. H.; Liu, X. Y.; Mironov, O.; Jones, C. J.; Ziatdinov, V. R. Perspectives on Some Challenges and Approaches for Developing the next Generation of Selective, Low Temperature, Oxidation Catalysts for Alkane Hydroxylation Based on the CH Activation Reaction. *J. Mol. Catal. A Chem.* **2004**, *220*, 7–25.

(6)   Mofarahi, M.; Gholipour, F. Gas Adsorption Separation of CO2/CH4 System Using Zeolite 5A. *Microporous Mesoporous Mater.* **2014**, *200*, 1–10.

(7)   Xue, C. L.; Cheng, W. P.; Hao, W. M.; Ma, J. H.; Li, R. F. CH 4 /N 2 Adsorptive Separation on Zeolite X/AC Composites. *J. Chem.* **2019**, *2019*, 1–9.

(8)   Hauchhum, L.; Mahanta, P. Carbon Dioxide Adsorption on Zeolites and Activated Carbon by Pressure Swing Adsorption in a Fixed Bed. *Int. J. Energy Environ. Eng.* **2014**, *5*, 349–356.

(9)   Arora, Y.; Seth, C.; Khushalani, D. Crafting Inorganic Materials for Use in Energy Capture and Storage. *Langmuir* **2019**, *35*, 9101–9114.

(10)   Ponrouch, A.; Monti, D.; Boschin, A.; Steen, B.; Johansson, P.; Palacín, M. R. Non-Aqueous Electrolytes for Sodium-Ion Batteries. *J. Mater. Chem. A* **2015**, *3*, 22–42.

(11)   Ouahab, L. Coordination Complexes in Conducting and Magnetic Molecular Materials. *Coord. Chem. Rev.* **1998**, *178–180* (PART 2), 1501–1531.

(12)   Tamaki, H.; Matsumoto, N.; Koikawa, M.; Achiwa, N.; Okawa, H.; Zhong, Z. J.;

Kida, S.; Hashimoto, Y. Design of Metal-Complex Magnets. Syntheses and Magnetic Properties of Mixed-Metal Assemblies {NBu4[MCr(Ox)3]}x (NBu4+ = Tetra(n-Butyl)Ammonium Ion; Ox2- = Oxalate Ion; M = Mn2+, Fe2+, Co2+, Ni2+, Cu2+, Zn2+). *J. Am. Chem. Soc.* **1992**, *114*, 6974–6979.

(13) Leong, W. L.; Vittal, J. J. One-Demensional Coordination Polymers: Complexity and Diversity in Structures, Properties, and Applications. *Chem. Rev.* **2011**, *111*, 688–764.

(14) Jin, H.; Li, J.; Iocozzia, J.; Zeng, X.; Wei, P.-C.; Yang, C.; Li, N.; Liu, Z.; He, J. H.; Zhu, T.; et al. Hybrid Organic-Inorganic Thermoelectric Materials and Devices. *Angew. Chemie Int. Ed.* **2019**, *58*, 15206–15226.

(15) Yu, K. J.; Yan, Z.; Han, M.; Rogers, J. A. Inorganic Semiconducting Materials for Flexible and Stretchable Electronics. *npj Flex. Electron.* **2017**, *1*, 1–14.

(16) Kim, T. W.; Yang, Y.; Li, F.; Kwan, W. L. Electrical Memory Devices Based on Inorganic/Organic Nanocomposites. *NPG Asia Mater.* **2012**, *4* , 1–12.

(17) Silva, J. *Inorganic Fertilizer Materials*; **2000**.

(18) Opala, P. A.; Okalebo, J. R.; Othieno, C. O. Effects of Organic and Inorganic Materials on Soil Acidity and Phosphorus Availability in a Soil Incubation Study. *ISRN Agron.* **2012**, *2012*, 1–10.

(19) Yan, Y.; He, T.; Zhao, B.; Qi, K.; Liu, H.; Xia, B. Y. Metal/Covalent-Organic Frameworks-Based Electrocatalysts for Water Splitting. *J. Mater. Chem. A* **2018**, *6*, 15905–15926.

(20) Cardenas-Morcoso, D.; Ifraemov, R.; García-Tecedor, M.; Liberman, I.; Gimenez, S.; Hod, I. A Metal-Organic Framework Converted Catalyst That Boosts Photo-Electrochemical Water Splitting. *J. Mater. Chem. A* **2019**, *7*, 11143–11149.

(21) Yun, S.; Hagfeldt, A.; Ma, T. Pt-Free Counter Electrode for Dye-Sensitized Solar Cells with High Efficiency. *Adv. Mater.* **2014**, *26*, 6210–6237.

(22) Ahmad, S.; Yum, J.-H.; Butt, H.-J.; Nazeeruddin, M. K.; Grätzel, M. Efficient Platinum-Free Counter Electrodes for Dye-Sensitized Solar Cell Applications. *ChemPhysChem* **2010**, *11*, 2814–2819.

(23) Jena, A. K.; Kulkarni, A.; Miyasaka, T. Halide Perovskite Photovoltaics: Background, Status, and Future Prospects. *Chem. Rev.* **2019**, *119* , 3036–3103.

(24) Tai, Q.; Tang, K. C.; Yan, F. Recent Progress of Inorganic Perovskite Solar Cells. *Energy Environ. Sci.* **2019**, *12*, 2375–2405.

(25) Thapa, S.; Bhardwaj, K.; Basel, S.; Pradhan, S.; Eling, C. J.; Adawi, A. M.; Bouillard, J. S. G.; Stasiuk, G. J.; Reiss, P.; Pariyar, A.; et al. Long-Term Ambient Air-Stable

Cubic CsPbBr3 Perovskite Quantum Dots Using Molecular Bromine. *Nanoscale Adv.* **2019**, *1*, 3388–3391.

(26)   Abas, N.; Kalair, A.; Khan, N. Review of Fossil Fuels and Future Energy Technologies. *Futures* **2015**, *69*, 31–49.

(27)   Kåberger, T. Progress of Renewable Electricity Replacing Fossil Fuels. *Glob. Energy Interconnect.* **2018**, *1*, 48–52.

(28)   Son, Y. H.; Bui, P. T. M.; Lee, H. R.; Akhtar, M. S.; Shah, D. K.; Yang, O. B. A Rapid Synthesis of Mesoporous Mn2O3 Nanoparticles for Supercapacitor Applications. *Coatings* **2019**, *9*, 1-11.

(29)   Hazarika, K. K.; Goswami, C.; Saikia, H.; Borah, B. J.; Bharali, P. Cubic Mn_2O_3 Nanoparticles on Carbon as Bifunctional Electrocatalyst for Oxygen Reduction and Oxygen Evolution Reactions. *Mol. Catal.* **2018**, *451*, 153–160.

(30)   Jahan, M.; Tominaka, S.; Henzie, J. Phase Pure α-Mn 2 O 3 Prisms and Their Bifunctional Electrocatalytic Activity in Oxygen Evolution and Reduction Reactions. *Dalt. Trans.* **2016**, *45*, 18494–18501.

(31)   Xia, W.; Mahmood, A.; Liang, Z.; Zou, R.; Guo, S. Earth-Abundant Nanomaterials for Oxygen Reduction. *Angew. Chemie Int. Ed.* **2016**, *55*, 2650–2676.

(32)   Salunkhe, R. R.; Kaneti, Y. V.; Yamauchi, Y. Metal-Organic Framework-Derived Nanoporous Metal Oxides toward Supercapacitor Applications: Progress and Prospects. *ACS Nano* **2017**, *11*, 5293–5308.

(33)   Xie, Z.; Xu, W.; Cui, X.; Wang, Y. Recent Progress in Metal–Organic Frameworks and Their Derived Nanostructures for Energy and Environmental Applications. *ChemSusChem* **2017**, *10*, 1645–1663.

(34)   Mai, H. D.; Rafiq, K.; Yoo, H. Nano Metal-Organic Framework-Derived Inorganic Hybrid Nanomaterials: Synthetic Strategies and Applications. *Chem. - A Eur. J.* **2017**, *23*, 5631–5651.

(35)   Robin, A. Y.; Fromm, K. M. Coordination Polymer Networks with O- and N-Donors: What They Are, Why and How They Are Made. *Coord. Chem. Rev.* **2006**, *250*, 2127–2157.

(36)   Archer, R. D. Preparative Inorganic Reactions. Volume. *J. Am. Chem. Soc.* **1965**, *87*, 1151–1152.

(37)   Chen, X.-M. Assembly Chemistry of Coordination Polymers. In *Modern Inorganic Synthetic Chemistry*; Elsevier, **2011**; 207–225.

(38)   Kitagawa, S.; Kitaura, R.; Noro, S. I. Functional Porous Coordination Polymers. *Angew. Chemie - Int. Ed.* **2004**, *43*, 2334–2375.

(39)   Stock, N.; Biswas, S. Synthesis of Metal-Organic Frameworks (MOFs): Routes to Various MOF Topologies, Morphologies, and Composites. *Chem. Rev.* **2012**, *112*, 933–969.

(40)   Li, N.; Feng, R.; Zhu, J.; Chang, Z.; Bu, X. H. Conformation Versatility of Ligands in Coordination Polymers: From Structural Diversity to Properties and Applications. *Coord. Chem. Rev.* **2018**, *375*, 558–586.

(41)   Jiang, H. L.; Makal, T. A.; Zhou, H. C. Interpenetration Control in Metal-Organic Frameworks for Functional Applications. *Coord. Chem. Rev.* **2013**, *257*, 2232–2249.

(42)   Gong, Y. N.; Zhong, D. C.; Lu, T. B. Interpenetrating Metal-Organic Frameworks. *CrystEngComm* **2016**, *18*, 2596–2606.

(43)   Verma, G.; Butikofer, S.; Kumar, S.; Ma, S. Regulation of the Degree of Interpenetration in Metal–Organic Frameworks. *Top. Curr. Chem.* **2020**, *378*, 1–45.

(44)   Cui, W. G.; Zhang, G. Y.; Hu, T. L.; Bu, X. H. Metal-Organic Framework-Based Heterogeneous Catalysts for the Conversion of C1 Chemistry: CO, CO 2 and CH 4. *Coord. Chem. Rev.* **2019**, *387*, 79–120.

(45)   Zhu, L.; Liu, X. Q.; Jiang, H. L.; Sun, L. B. Metal-Organic Frameworks for Heterogeneous Basic Catalysis. *Chem. Rev.* **2017**, *117*, 8129–8176.

(46)   Raupp, Y. S.; Yildiz, C.; Kleist, W.; Meier, M. A. R. Aerobic Oxidation of α-Pinene Catalyzed by Homogeneous and MOF-Based Mn Catalysts. *Appl. Catal. A Gen.* **2017**, *546*, 1–6.

(47)   Tu, T. N.; Nguyen, M. V.; Nguyen, H. L.; Yuliarto, B.; Cordova, K. E.; Demir, S. Designing Bipyridine-Functionalized Zirconium Metal–Organic Frameworks as a Platform for Clean Energy and Other Emerging Applications. *Coord. Chem. Rev.* **2018**, *364*, 33–50.

(48)   Agarwal, R. A.; Gupta, N. K. CO2 Sorption Behavior of Imidazole, Benzimidazole and Benzoic Acid Based Coordination Polymers. *Coord. Chem. Rev.* **2017**, *332*, 100–121.

(49)   Dincă, M.; Long, J. R. Hydrogen Storage in Microporous Metal-Organic Frameworks with Exposed Metal Sites. *Angew. Chemie - Int. Ed.* **2008**, *47*, 6766–6779.

(50)   Lustig, W. P.; Li, J. Luminescent Metal–Organic Frameworks and Coordination Polymers as Alternative Phosphors for Energy Efficient Lighting Devices. *Coord. Chem. Rev.* **2018**, *373*, 116–147.

(51)   An, H.; Li, M.; Gao, J.; Zhang, Z.; Ma, S.; Chen, Y. Incorporation of Biomolecules in Metal-Organic Frameworks for Advanced Applications. *Coord. Chem. Rev.* **2019**,

384, 90–106.

(52) Lim, E. K.; Kim, T.; Paik, S.; Haam, S.; Huh, Y. M.; Lee, K. Nanomaterials for Theranostics: Recent Advances and Future Challenges. *Chem. Rev.* **2015**, *115*, 327–394.

(53) Horcajada, P.; Chalati, T.; Serre, C.; Gillet, B.; Sebrie, C.; Baati, T.; Eubank, J. F.; Heurtaux, D.; Clayette, P.; Kreuz, C.; et al. Porous Metal-Organic-Framework Nanoscale Carriers as a Potential Platform for Drug Deliveryand Imaging. *Nat. Mater.* **2010**, *9*, 172–178.

(54) He, Y.; Chen, F.; Li, B.; Qian, G.; Zhou, W.; Chen, B. Porous Metal–Organic Frameworks for Fuel Storage. *Coord. Chem. Rev.* **2018**, *373*, 167–198.

(55) Xu, G.; Nie, P.; Dou, H.; Ding, B.; Li, L.; Zhang, X. Exploring Metal Organic Frameworks for Energy Storage in Batteries and Supercapacitors. *Mater. Today* **2017**, *20*, 191–209.

(56) Yue, Q.; Gao, E. Q. Azide and Carboxylate as Simultaneous Coupler for Magnetic Coordination Polymers. *Coord. Chem. Rev.* **2019**, *382*, 1–31.

(57) Son, K.; Kim, J. Y.; Schütz, G.; Kang, S. G.; Moon, H. R.; Oh, H. Coordinated Molecule-Modulated Magnetic Phase with Metamagnetism in Metal-Organic Frameworks. *Inorg. Chem.* **2019**, *58*, 8895–8899.

(58) Jiang, X.; Liu, C. M.; Kou, H. Z. Porous Coordination Polymers Based on {Mn6} Single-Molecule Magnets. *Inorg. Chem.* **2016**, *55*, 5880–5885.

(59) Suárez-García, S.; Arias-Ramos, N.; Frias, C.; Candiota, A. P.; Arús, C.; Lorenzo, J.; Ruiz-Molina, D.; Novio, F. Dual T1/ T2 Nanoscale Coordination Polymers as Novel Contrast Agents for MRI: A Preclinical Study for Brain Tumor. *ACS Appl. Mater. Interfaces* **2018**, *10*, 38819–38832.

(60) Xu, Y.; Li, Q.; Xue, H.; Pang, H. Metal-Organic Frameworks for Direct Electrochemical Applications. *Coord. Chem. Rev.* **2018**, *376*, 292–318.

(61) Lou, X.; Ning, Y.; Li, C.; Shen, M.; Hu, B.; Hu, X.; Hu, B. Exploring the Capacity Limit: A Layered Hexacarboxylate-Based Metal-Organic Framework for Advanced Lithium Storage. *Inorg. Chem.* **2018**, *57*, 3126–3132.

(62) Worrall, S. D.; Bissett, M. A.; Hirunpinyopas, W.; Attfield, M. P.; Dryfe, R. A. W. Facile Fabrication of Metal-Organic Framework HKUST-1-Based Rewritable Data Storage Devices. *J. Mater. Chem. C* **2016**, *4*, 8687–8695.

(63) Huang, Y.; Zhang, J.; Yue, D.; Cui, Y.; Yang, Y.; Li, B.; Qian, G. Solvent-Triggered Reversible Phase Changes in Two Manganese-Based Metal–Organic Frameworks and Associated Sensing Events. *Chem. - A Eur. J.* **2018**, *24*, 13231–13237.

(64)   Wang, M. Q.; Ye, C.; Bao, S. J.; Zhang, Y.; Yu, Y. N.; Xu, M. W. Carbon Nanotubes Implanted Manganese-Based MOFs for Simultaneous Detection of Biomolecules in Body Fluids. *Analyst* **2016**, *141*, 1279–1285.

(65)   Remya, V. R.; Kurian, M. Synthesis and Catalytic Applications of Metal–Organic Frameworks: A Review on Recent Literature. *Int. Nano Lett.* **2019**, *9*, 17–29.

(66)   Feng, S.-H.; Li, G.-H. Hydrothermal and Solvothermal Syntheses. In *Modern Inorganic Synthetic Chemistry, Second Edition*; Elsevier, **2017**; 73–104.

(67)   Loera-Serna, S.; Ortiz, E. Catalytic Applications of Metal-Organic Frameworks. In *Advanced Catalytic Materials - Photocatalysis and Other Current Trends*; Norena, L. E., Wang, J.-A., Eds.; InTech, **2016**; 95–122.

(68)   Klinowski, J.; Almeida Paz, F. A.; Silva, P.; Rocha, J. Microwave-Assisted Synthesis of Metal-Organic Frameworks. *Dalt. Trans.* **2011**, *40*, 321–330.

(69)   Seth, S.; Matzger, A. J. Metal−Organic Frameworks: Examples, Counterexamples, and an Actionable Definition. *Cryst. Growth Des.* **2017**, *17*, 4043–4048.

(70)   Rowsell, J. L. C.; Yaghi, O. M. Metal–Organic Frameworks: A New Class of Porous Materials. *Microporous Mesoporous Mater.* **2004**, *73*, 3–14.

(71)   Biradha, K.; Ramanan, A.; Vittal, J. J. Coordination Polymers Versus Metal−Organic Frameworks. *Cryst. Growth Des.* **2009**, *9*, 2969–2970.

(72)   Sun, H. L.; Gao, S.; Ma, B. Q.; Su, G.; Batten, S. R. Structures and Magnetism of a Series Mn(II) Coordination Polymers Containing Pyrazine-Dioxide Derivatives and Different Anions. *Cryst. Growth Des.* **2005**, *5*, 269–277.

(73)   Rosi, N. L.; Kim, J.; Eddaoudi, M.; Chen, B.; O'Keeffe, M.; Yaghi, O. M. Rod Packings and Metal-Organic Frameworks Constructed from Rod-Shaped Secondary Building Units. *J. Am. Chem. Soc.* **2005**, *127*, 1504–1518.

(74)   Wang, X. Y.; Wang, L.; Wang, Z. M.; Su, G.; Gao, S. Coexistence of Spin-Canting, Metamagnetism, and Spin-Flop in a (4,4) Layered Manganese Azide Polymer. *Chem. Mater.* **2005**, *17*, 6369–6380.

(75)   Tang, Y. Z.; Wang, X. Sen; Zhou, T.; Xiong, R. G. A Novel 2D Manganese(II) Coordination Polymer Exhibiting Ferromagnetic Interaction. *Cryst. Growth Des.* **2006**, *6*, 11–13.

(76)   Hoi, R. M.; Kobayashi, N.; Myunghyun, P. S. Porous Metal-Organic Framework with Coordinatively Unsaturated Mn II Sites:Sorption Properties for Various Gases. *Inorg. Chem.* **2006**, *45*, 8672–8676.

(77)   Yuan, M.; Zhao, F.; Zhang, W.; Wang, Z. M.; Gao, S. Azide-Bridged One-Dimensional MnIII Polymers: Effects of Side Group of Schiff Base Ligands on

Structure and Magnetism. *Inorg. Chem.* **2007**, *46*, 11235–11242.

(78)   Taylor, K. M. L.; Rieter, W. J.; Lin, W. Manganese-Based Nanoscale Metal-Organic Frameworks for Magnetic Resonance Imaging. *J. Am. Chem. Soc.* **2008**, *130*, 14358–14359.

(79)   Horike, S.; Dincă, M.; Tamaki, K.; Long, J. R. Size-Selective Lewis Acid Catalysis in a Microporous Metal-Organic Framework with Exposed Mn2+ Coordination Sites. *J. Am. Chem. Soc.* **2008**, *130*, 5854–5855.

(80)   Zhang, X.; Ge, C.; Yin, J.; Zhao, Y.; He, C. Interpenetrating 2D Manganese(II) Coordination Polymer Supported by 4,4'-Bis(Dimethoxyphosphorylmethyl)-Biphenyl Ligands. *Chinese J. Chem.* **2009**, *27*, 1195–1198.

(81)   Ladrak, T.; Smulders, S.; Roubeau, O.; Teat, S. J.; Gamez, P.; Reedijk, J. Manganese-Based Metal-Organic Frameworks as Heterogeneous Catalysts for the Cyanosilylation of Acetaldehyde. *Eur. J. Inorg. Chem.* **2010**, *2010*, 3804–3812.

(82)   Li, N.; Chen, L.; Lian, F.; Jiang, F.; Hong, M. Manganese(II) Complexes with V-Shaped Sulfonyldibenzoate: The 3D Structures with Interpenetrated Threefold or Tetra-Nuclear Manganese(II) Units. *Inorganica Chim. Acta* **2010**, *363*, 3291–3301.

(83)   Yang, J. W.; Zhang, J.; Yan, Y.; Huang, X. C.; Tong, S. L. A Coordination Polymer of Manganese (III) Porphyrinate with Right-Handed Helicity and Opticity. *Solid State Sci.* **2010**, *12*, 1242–1247.

(84)   Xie, M. H.; Yang, X. L.; Wu, C. De. From 2D to 3D: A Single-Crystal-to-Single-Crystal Photochemical Framework Transformation and Phenylmethanol Oxidation Catalytic Activity. *Chem. - A Eur. J.* **2011**, *17*, 11424–11427.

(85)   Liu, Q.; Yu, L.; Wang, Y.; Ji, Y.; Horvat, J.; Cheng, M. L.; Jia, X.; Wang, G. Manganese-Based Layered Coordination Polymer: Synthesis, Structural Characterization, Magnetic Property, and Electrochemical Performance in Lithium-Ion Batteries. *Inorg. Chem.* **2013**, *52*, 2817–2822.

(86)   Zhao, Y. P.; Yang, H.; Wang, F.; Du, Z. Y. A Microporous Manganese-Based Metal-Organic Framework for Gas Sorption and Separation. *J. Mol. Struct.* **2014**, *1074*, 19–21.

(87)   Lv, Y.; Shi, P.; Shen, W.; Chen, X.; Zhao, G. A Series of Novel Zn(II) and Mn(II) Metal-Organic Frameworks Constructed by 2,4-Bis-Oxyacetate-Benzoic Acid: Syntheses, Structures and Photoluminescence. *Sci. China Chem.* **2015**, *58*, 448–456.

(88)   Zhang, Y.; Lin, B.; Sun, Y.; Zhang, X.; Yang, H.; Wang, J. Carbon Nanotubes@metal–Organic Frameworks as Mn-Based Symmetrical Supercapacitor Electrodes for Enhanced Charge Storage. *RSC Adv.* **2015**, *5*, 58100–58106.

(89)   Li, T.; Li, C.; Hu, X.; Lou, X.; Hu, H.; Pan, L.; Chen, Q.; Shen, M.; Hu, B. Reversible Lithium Storage in Manganese and Cobalt 1,2,4,5-Benzenetetracarboxylate Metal-Organic Framework with High Capacity. *RSC Adv.* **2016**, *6*, 61319–61324.

(90)   Dey, S. K.; Hazra, M.; Thompson, L. K.; Patra, A. Manganese(II) Coordination Polymer Having Pyrazine and μ-Phenolato Bridging: Structure, Magnetism and Biological Studies. *Inorganica Chim. Acta* **2016**, *443*, 224–229.

(91)   Hu, H.; Lou, X.; Li, C.; Hu, X.; Li, T.; Chen, Q.; Shen, M.; Hu, B. A Thermally Activated Manganese 1,4-Benzenedicarboxylate Metal Organic Framework with High Anodic Capability for Li-Ion Batteries. *New J. Chem.* **2016**, *40*, 9746–9752.

(92)   Das, K.; Datta, A.; Beyene, B. B.; Massera, C.; Garribba, E.; Sinha, C.; Akitsu, T.; Tanka, S. A Zig-Zag End-to-End Azido Bridged MnIII 1-D Coordination Polymer: Spectral Elucidation, Magnetism, Redox Study and Biological Activity. *Polyhedron* **2017**, *127*, 315–322.

(93)   Paul, M.; Dastidar, P. Coordination Polymers Derived from Non-Steroidal Anti-Inflammatory Drugs for Cell Imaging and Drug Delivery. *Chem. - A Eur. J.* **2016**, *22*, 988–998.

(94)   Wu, Y.; Song, X.; Li, S.; Zhang, J.; Yang, X.; Shen, P.; Gao, L.; Wei, R.; Zhang, J.; Xiao, G. 3D-Monoclinic M–BTC MOF (M = Mn, Co, Ni) as Highly Efficient Catalysts for Chemical Fixation of CO2 into Cyclic Carbonates. *J. Ind. Eng. Chem.* **2018**, *58*, 296–303.

(95)   Shi, W. J.; Du, L. Y.; Yang, H. Y.; Zhang, K.; Hou, L.; Wang, Y. Y. Ligand Configuration-Induced Manganese(II) Coordination Polymers: Syntheses, Crystal Structures, Sorption, and Magnetic Properties. *Inorg. Chem.* **2017**, *56*, 10090–10098.

(96)   Mahmoudi, G.; Chowdhury, H.; Lofland, S. E.; Ghosh, B. K.; Kirillov, A. M. Two Manganese(II) Coordination Polymers Driven by (Iso)Nicotinoyl-Hydrazone Blocks and Pseudohalide Ancillary Ligands: Syntheses, Structural Features, and Magnetic Properties. *J. Coord. Chem.* **2017**, *70*, 1973–1983.

(97)   Wang, X.; Liu, X.; Rong, H.; Song, Y.; Wen, H.; Liu, Q. Layered Manganese-Based Metal–Organic Framework as a High Capacity Electrode Material for Supercapacitors. *RSC Adv.* **2017**, *7*, 29611–29617.

(98)   Du, Z. Y.; Zhang, L.; Wang, B. Y.; Liu, S. J.; Huang, B.; Liu, C. M.; Zhang, W. X. Two Magnetic Δ-Chain-Based Mn(II) and Co(II) Coordination Polymers with Mixed Carboxylate-Phosphinate and M3-OH- Bridges. *CrystEngComm* **2017**, *19*, 1052–1057.

(99)   Chen, L. D.; Zheng, Y. Q.; Zhu, H. L. Manganese Oxides Derived from Mn(II)-

Based Metal–Organic Framework as Supercapacitor Electrode Materials. *J. Mater. Sci.* **2018**, *53*, 1346–1355.

(100) Ming, M.; Bai, N. A Rare 3D Chloro-Laced Mn(II) Metal-Organic Framework to Show Sensitive Probing Effect to Hg2+. *J. Solid State Chem.* **2017**, *254*, 9–13.

(101) Chen, X.; Peng, Y.; Han, X.; Liu, Y.; Lin, X.; Cui, Y. Sixteen Isostructural Phosphonate Metal-Organic Frameworks with Controlled Lewis Acidity and Chemical Stability for Asymmetric Catalysis. *Nat. Commun.* **2017**, *8*, 1–9.

(102) Pal, S.; Maiti, S.; Nayek, H. P. A Three-Dimensional (3D) Manganese (II) Coordination Polymer: Synthesis, Structure and Catalytic Activities. *Appl. Organomet. Chem.* **2018**, *32*, 1–9.

(103) Adpakpang, K.; Pratanpornlerd, W.; Ponchai, P.; Tranganphaibul, W.; Thongratkaew, S.; Faungnawakij, K.; Horike, S.; Siritanon, T.; Rujiwatra, A.; Ogawa, M.; et al. Unsaturated Mn(II)-Centered [Mn(BDC)]n Metal-Organic Framework with Strong Water Binding Ability and Its Potential for Dehydration of an Ethanol/Water Mixture. *Inorg. Chem.* **2018**, *57*, 13075–13078.

(104) Demakov, P. A.; Sapchenko, S. A.; Samsonenko, D. G.; Dybtsev, D. N.; Fedin, V. P. Coordination Polymers Based on Zinc(Ii) and Manganese(Ii) with 1,4-Cyclohexanedicarboxylic Acid. *Russ. Chem. Bull.* **2018**, *67*, 490–496.

(105) Davarcı, D. Design and Construction of One-Dimensional Coordination Polymers Based on the Dispiro-Dipyridyloxy-Cyclotriphosphazene Ligand. *Polyhedron* **2018**, *146*, 99–107.

(106) Bikas, R.; Farzaneh-Bonab, H.; Noshiranzadeh, N.; Aygün, M.; Emami, M.; Lis, T. Coumarin-Naphthohydrazone Ligand with a Rare Coordination Mode to Form Mn(II) and Co(II) 1-D Coordination Polymers: Synthesis, Characterization, and Crystal Structure. *J. Coord. Chem.* **2018**, *71*, 1127–1146.

(107) Fang, X. D.; Yang, L. B.; Dou, A. N.; Liu, Y. E.; Yao, J.; Xu, Q. Q.; Zhu, A. X. Synthesis, Crystal Structure and Photocatalytic Properties of a Mn (II) Metal-Organic Framework Based on a Thiophene-Functionalized Dicarboxylate Ligand. *Inorg. Chem. Commun.* **2018**, *96*, 124–127.

(108) Kang, H. X.; Fu, Y. Q.; Ju, F. Y.; Li, G. L.; Li, X. L.; Liu, G. Z. Syntheses, Structures, and Magnetic Properties of Two Mn(II) Coordination Polymers Based on 4-Fluorocinnamic Acid and 1,10-Phenanthroline. *Russ. J. Coord. Chem. Khimiya* **2018**, *44*, 340–346.

(109) Spirkl, S.; Grzywa, M.; Volkmer, D. Synthesis and Characterization of a Flexible Metal Organic Framework Generated from MnIII and the 4,4′-Bipyrazolate-Ligand.

Dalt. Trans. **2018**, *47*, 8779–8786.

(110)   Zou, G. D.; Gong, L. K.; Liu, L.; Zhang, Q.; Zhao, X. H. Two Low-Dimensional Transition Metal Coordination Polymers Constructed from Thiophene-2,5-dicarboxylic Acid and N/O-Donor Ligands: Syntheses, Structures and Magnetic Property. *Inorg. Chem. Commun.* **2019**, *99*, 140–144.

(111)   Köse Yaman, P.; Erer, H.; Yeşilel, O. Z. Three Dimensional Manganese(II) Coordination Polymers Constructed from 2,2-Dimethylglutarate and Bis(Pyridyl) Type Ligands. *Polyhedron* **2019**, *171*, 317–322.

(112)   Sundriyal, S.; Mishra, S.; Deep, A. Study of Manganese-1,4-Benzenedicarboxylate Metal Organic Framework Electrodes Based Solid State Symmetrical Supercapacitor. *Energy Procedia* **2019**, *158*, 5817–5824.

(113)   Lan, W.; Hao, X.; Dou, Y.; Zhou, Z.; Yang, L.; Liu, H.; Li, D.; Dong, Y.; Kong, L.; Zhang, D. Various Structural Types of Cyanide-Bridged FeIII-MnIII Bimetallic Coordination Polymers (CPs) and Polynuclear Clusters Based-on a New Mer-Tricyanoiron(III)Building Block: Synthesis, Crystal Structures, and Magnetic Properties. *Polymers (Basel).* **2019**, *11*, 1585.

(114)   Li, X. F.; Wang, X.; Wu, Y. Y.; Zhao, X. W.; Li, H. Y.; Li, Y. M. Four Coordination Polymers Based on 4'-(4-Carboxyphenyl)-2,2':6',2''-Terpyridine: Syntheses, Structures and Properties. *J. Solid State Chem.* **2019**, *269*, 118–124.

(115)   Ge, Y.; Li, G.; Fu, D.; Liu, L.; Wu, B. Manganese(II) and Zinc(II) Coordination Polymers Based on 2-(5-Bromo-Pyridin-3-Yl)-1H-Imidazole-4,5-Dicarboxylic Acid: Synthesis, Structure and Properties. *J. Coord. Chem.* **2019**, *72*, 1820–1832.

(116)   Meng, H. H.; Xia, X. L.; Lin, Z. G.; Song, X. Q. A New One Dimensional Mn(III) Coordination Polymer Constructed by a Salicylamide Imine Multidentate Ligand: Structure, Magnetic and Luminescent Properties. *J. Inorg. Organomet. Polym. Mater.* **2019**, *29*, 1995–2002.

(117)   Meng, L.; Zhao, L.; Guo, G.; Liu, X.; Liang, Z.; Xiu, J.; Zhou, X. Syntheses, Structures, and Characteristics of Three Metal Complexes Constructed Using Hexacarboxylic Acid. *Molecules* **2019**, *24*, 1–12.

(118)   Morales-Morales, N.; Rodríguez-Olivas, M.; Téllez-López, A.; Martínez-Otero, D.; Morales-Luckie, R. A.; Sánchez-Mendieta, V. Syntheses and Crystal Structures of Mn(II), Ni(II) and Cu(II) Coordination Compounds Assembled by Maleato and Dimethyl-2,2′-Bipyridines. *J. Chem. Crystallogr.* **2019**, *49*, 8–20.

(119)   Sharma, N.; Dhankhar, S. S.; Nagaraja, C. M. A Mn(II)-Porphyrin Based Metal-Organic Framework (MOF) for Visible-Light-Assisted Cycloaddition of Carbon

Dioxide with Epoxides. *Microporous Mesoporous Mater.* **2019**, *280*, 372–378.

(120) Xiao, Q. Q.; Liu, D.; Wei, Y. L.; Cui, G. H. Two New Ternary Mn(II) Coordination Polymers by Regulation of Aromatic Carboxylate Ligands: Synthesis, Structures, Photocatalytic and Selective Ion-Sensing Properties. *J. Solid State Chem.* **2019**, *273*, 67–74.

(121) Xu, J.; Yang, Y.; Wang, Y.; Cao, J.; Chen, Z. Enhanced Electrochemical Properties of Manganese-Based Metal Organic Framework Materials for Supercapacitors. *J. Appl. Electrochem.* **2019**, *49*, 1091–1102.

(122) Dutta, B.; Akhtaruzzaman; Sato, H.; Akitsu, T.; Slawin, A. M. Z.; Kar, U.; Sinha, C.; Mir, M. H. Two Acetylenedicarboxylato-Bridged 4-Styrylpyridine Appended 1D Coordination Polymers: Synthesis, Structural Characterization and Variable Temperature Magnetism. *J. Chem. Sci.* **2020**, *132*, 1–6.

Chapter II

(1) Zhao, Y.; Li, K.; Li, J. Solvothermal Synthesis of Multifunctional Coordination Polymers. *Zeitschrift für Naturforsch. B* **2010**, *65*, 976–998.

(2) Demazeau, G. Solvothermal Reactions: An Original Route for the Synthesis of Novel Materials. *J. Mater. Sci.* **2008**, *43*, 2104–2114.

(3) Morey, G. W.; Niggli, P. The Hydrothermal Formation of Silicates, A Review. *J. Am. Chem. Soc.* **1913**, *35*, 1086–1130.

(4) Feng, S.-H.; Li, G.-H. Hydrothermal and Solvothermal Syntheses. In *Modern Inorganic Synthetic Chemistry, Second Edition*; Elsevier, **2017**; 73–104.

(5) Loera-Serna, S.; Ortiz, E. Catalytic Applications of Metal-Organic Frameworks. In *Advanced Catalytic Materials - Photocatalysis and Other Current Trends*; Norena, L. E., Wang, J.-A., Eds.; InTech, **2016**; 95–122.

(6) Laudise, R. A. Hydrothermal Synthesis of Crystals. *Chem. Eng. News Eng. News* **1987**, *65*, 30–43.

(7) Bond, A. D. Single-Crystal X-Ray Diffraction. In *Analytical Techniques in the Pharmaceutical Sciences*; Mullertz, A., Perrie, Y., Rades, T., Eds.; Springer-Verlag New York, **2016**; 315–337.

(8)   To, P. S. *Chapter 7 : Basics of X-Ray Diffraction*; **1999**.

(9)   Dinnebier, R. E.; Billinge, S. J. L. Chapter 1. Principles of Powder Diffraction. In *Powder Diffraction: Theory and Practice*; Dinnebier, R. E., Billinge, S. J. L., Eds.; Royal Society of Chemistry: Cambridge, **2008**, *20*, 1–19.

(10)   Bunaciu, A. A.; Udriştioiu, E. gabriela; Aboul-Enein, H. Y. X-Ray Diffraction: Instrumentation and Applications. *Crit. Rev. Anal. Chem.* **2015**, *45*, 289–299.

(11)   Holder, C. F.; Schaak, R. E. Tutorial on Powder X-Ray Diffraction for Characterizing Nanoscale Materials. *ACS Nano.* **2019**, *13*, 7359–7365.

(12)   Thakral, N. K.; Zanon, R. L.; Kelly, R. C.; Thakral, S. Applications of Powder X-Ray Diffraction in Small Molecule Pharmaceuticals: Achievements and Aspirations. *J. Pharm. Sci.* **2018**, *107*, 2969–2982.

(13)   J. Michael Hollas. *Modern Spectroscopy*; **2004**.

(14)   Nakamoto, K. Theory of Normal Vibrations. *Infrared Raman Spectra Inorg. Coord. Compd.* **2009**, 1–147.

(15)   Ismail, A. A.; van de Voort, F. R.; Sedman, J. Chapter 4 Fourier Transform Infrared Spectroscopy: Principles and Applications. *Tech. Instrum. Anal. Chem.* **1997**, *18*, 93–139.

(16)   Javadzadeh, Y.; Hamedeyaz, S. Floating Drug Delivery Systems for Eradication of Helicobacter Pylori in Treatment of Peptic Ulcer Disease. In *Trends in Helicobacter pylori Infection*; InTech, **2014**, *1*, 13.

(17)   Sharp, J. H.; Manley, T. R. Thermal Analysis. *Proc. Soc. Anal. Chem.* **1971**, *8*, 112.

(18)   Coats, A. W.; Redfern, J. P. Thermogravimetric Analysis. A Review. *Analyst* **1963**, *88*, 906–924.

(19)   Simon, J. *Introduction to Thermal Analysis Techniques and Applications*; Brown, M. E., Ed.; Kluwer Academic Publishers, **2001**, *1*.

(20)   Lowell, S.; Shields, J. E.; Thomas, M. A.; Thommes, M. *Characterization of Porous Solids and Powders: Surface Area, Pore Size and Density*; Professor Brian Scarlett, Ed.; Particle Technology Series; Springer Netherlands: Dordrecht, **2004**,

16.

(21)   Sinha, P.; Datar, A.; Jeong, C.; Deng, X.; Chung, Y. G.; Lin, L.-C. Surface Area Determination of Porous Materials Using the Brunauer–Emmett–Teller (BET) Method: Limitations and Improvements. *J. Phys. Chem. C* **2019**, *123*, 20195–20209.

(22)   Ambroz, F.; Macdonald, T. J.; Martis, V.; Parkin, I. P. Evaluation of the BET Theory for the Characterization of Meso and Microporous MOFs. *Small Methods* **2018**, *2*, 1-17.

(23)   Walton, K. S.; Snurr, R. Q. Applicability of the BET Method for Determining Surface Areas of Microporous Metal-Organic Frameworks. *J. Am. Chem. Soc.* **2007**, *129*, 8552–8556.

(24)   Brunauer, S.; Emmett, P. H.; Teller, E. Adsorption of Gases in Multimolecular Layers. *J. Am. Chem. Soc.* **1938**, *60*, 309–319.

(25)   Dollimore, D.; Spooner, P.; Turner, A. The Bet Method of Analysis of Gas Adsorption Data and Its Relevance to the Calculation of Surface Areas. *Surf. Technol.* **1976**, *4*, 121–160.

(26)   Sing, K. S. W.; Everett, D. H.; Haul, R. A. W.; Moscou, L.; Pierotti, R. A.; Rouquerol, J.; Seimieniewska, T. Reporting Physisorption Data For Gas/Solid Systems with Special Reference to the Determination of Surface Area and Porosity; *Pure & Appl. Chem.* **1985,** 57.

(27)   Thommes, M.; Kaneko, K.; Neimark, A. V.; Olivier, J. P.; Rodriguez-Reinoso, F.; Rouquerol, J.; Sing, K. S. W. Physisorption of Gases, with Special Reference to the Evaluation of Surface Area and Pore Size Distribution (IUPAC Technical Report). *Pure Appl. Chem.* **2015**, *87*, 1051–1069.

(28)   Fagaly, R. L. Superconducting Quantum Interference Device Instruments and Applications. *Rev. Sci. Instrum.* **2006**, *77*, 1–45.

(29)   Clarke, J. Principles and Applications of SQUIDs. *Proc. IEEE* **1989**, *77*, 1208–1223.

(30)   Clarke, J.; Braginski, A. I. *The SQUID Handbook: Fundamentals and Technology of SQUIDS and SQUID Systems*; Wiley-VCH Verlag Gmb & Co. KGaA, **2006**, 1.

(31) Fuller, M.; Goree, W. S.; Goodman, W. L. An Introduction to the Use of SQUID Magnetometers in Biomagnetism. In *Magnetite Biomineralization and Magnetoreception in Organisms*; Plenum Press, New York, **1985**, 103–151.

(32) Buchner, M.; Höfler, K.; Henne, B.; Ney, V.; Ney, A. Tutorial: Basic Principles, Limits of Detection, and Pitfalls of Highly Sensitive SQUID Magnetometry for Nanomagnetism and Spintronics. *J. Appl. Phys.* **2018**, *124* , 1–13.

(33) Chooto, P. Cyclic Voltammetry and Its Applications. In *Voltammetry*; IntechOpen, **2019**, 1–14.

(34) Elgrishi, N.; Rountree, K. J.; McCarthy, B. D.; Rountree, E. S.; Eisenhart, T. T.; Dempsey, J. L. A Practical Beginner's Guide to Cyclic Voltammetry. *J. Chem. Educ.* **2018**, *95*, 197–206.

(35) Jia, Z.; Yin, G.; Zhang, J. Rotating Ring-Disk Electrode Method. In *Rotating Electrode Methods and Oxygen Reduction Electrocatalysts*; Elsevier, **2014**, 199–229.

(36) Dalton, F. Historical Origins of the Rotating Ring-Disk Electrode. *Interface Mag.* **2016**, *25*, 50–59.

(37) Zhou, R.; Zheng, Y.; Jaroniec, M.; Qiao, S. Z. Determination of the Electron Transfer Number for the Oxygen Reduction Reaction: From Theory to Experiment. *ACS Catal.* **2016**, *6*, 4720–4728.

(38) Thompson, M. CHNS Elemental Analysers. *Anal. Methods Comm. Tech. Briefs* **2008**, 29.

Chapter III

(1) Zhou, W.; Wu, H.; Yildirim, T. Enhanced H_2 Adsorption in Isostructural Metal−Organic Frameworks with Open Metal Sites: Strong Dependence of the Binding Strength on Metal Ions. *J. Am. Chem. Soc.* **2008**, *130*, 15268–15269.

(2) Sundriyal, S.; Mishra, S.; Deep, A. Study of Manganese-1,4-Benzenedicarboxylate Metal Organic Framework Electrodes Based Solid State Symmetrical Supercapacitor. *Ener. Proc.* **2019**, *158*, 5817–5824.

(3)   Ladrak, T.; Smulders, S.; Roubeau, O.; Teat, S. J.; Gamez, P.; Reedijk, J. Manganese-Based Metal-Organic Frameworks as Heterogeneous Catalysts for the Cyanosilylation of Acetaldehyde. *Eur. J. Inorg. Chem.* **2010**, *2010*, 3804–3812.

(4)   Fu, Y.; Su, J.; Yang, S.; Li, G.; Liao, F.; Xiong, M.; Lin, J. Syntheses, Structures and Magnetic Properties of Mn(II), Co(II) and Ni(II) Metal–Organic Frameworks Constructed from 1,3,5-Benzenetricarboxylate and Formate Ligands. *Inorganica Chim. Acta* **2010**, *363*, 645–652.

(5)   Li, T.; Li, C.; Hu, X.; Lou, X.; Hu, H.; Pan, L.; Chen, Q.; Shen, M.; Hu, B. Reversible Lithium Storage in Manganese and Cobalt 1,2,4,5-Benzenetetracarboxylate Metal-Organic Framework with High Capacity. *RSC Adv.* **2016**, *6*, 61319–61324.

(6)   Ismail, A. A.; van de Voort, F. R.; Sedman, J. Chapter 4 Fourier Transform Infrared Spectroscopy: Principles and Applications. *Tech. Instrum. Anal. Chem.* **1997**, *18*, 93–139.

(7)   Yuan, K.; Song, T.; Wang, D.; Zou, Y.; Li, J.; Zhang, X.; Tang, Z.; Hu, W. Bimetal–Organic Frameworks for Functionality Optimization: MnFe-MOF-74 as a Stable and Efficient Catalyst for the Epoxidation of Alkenes with H 2 O 2. *Nanoscale* **2018**, *10*, 1591–1597.

(8)   Xiao, T.; Liu, D. The Most Advanced Synthesis and a Wide Range of Applications of MOF-74 and Its Derivatives. *Micro. Meso. Mater.* **2019**, *283*, 88–103.

(9)   Adpakpang, K.; Pratanpornlerd, W.; Ponchai, P.; Tranganphaibul, W.; Thongratkaew, S.; Faungnawakij, K.; Horike, S.; Siritanon, T.; Rujiwatra, A.; Ogawa, M.; et al. Unsaturated Mn(II)-Centered [Mn(BDC)]$_n$ Metal–Organic Framework with Strong Water Binding Ability and Its Potential for Dehydration of an Ethanol/Water Mixture. *Inorg. Chem.* **2018**, *57*, 13075–13078.

(10)   Maiti, S.; Pramanik, A.; Mahanty, S. Electrochemical Energy Storage in Mn2O3 Porous Nanobars Derived from Morphology-Conserved Transformation of Benzenetricarboxylate-Bridged Metal-Organic Framework. *Cryst. Eng. Comm.* **2016**, *18*, 450–461.

(11)   Wu, Y.; Song, X.; Li, S.; Zhang, J.; Yang, X.; Shen, P.; Gao, L.; Wei, R.; Zhang,

J.; Xiao, G. 3D-Monoclinic M–BTC MOF (M = Mn, Co, Ni) as Highly Efficient Catalysts for Chemical Fixation of CO2 into Cyclic Carbonates. *J. Ind. Eng. Chem.* **2018**, *58*, 296–303.

Chapter IV

(1)   Sing, K. S. W.; Everett, D. H.; Haul, R. A. W.; Moscou, L.; Pierotti, R. A.; Rouquerol, J.; Seimieniewska, T. Reporting Physisorption Data For Gas/Solid Systems with Special Reference to the Determination of Surface Area and Porosity; *Pure and Applied Chemistry* **1985**, *57*, 603-619.

(2)   Thommes, M.; Kaneko, K.; Neimark, A. V.; Olivier, J. P.; Rodriguez-Reinoso, F.; Rouquerol, J.; Sing, K. S. W. Physisorption of Gases, with Special Reference to the Evaluation of Surface Area and Pore Size Distribution (IUPAC Technical Report). *Pure Appl. Chem.* **2015**, *87*, 1051–1069.

(3)   Hoppe, J. I. Effective Magnetic Moment. *J. Chem. Educ.* **1972**, *49*, 505.

(4)   Weng, Z.; Chen, Z.; Liang, F. Glycine-Templated Manganese Sulfate with New Topology and Canted Antiferromagnetism. *Inorg. Chem.* **2009**, *48*, 8703–8708.

(5)   Gupta, K.; Dadwal, A.; Rana, S.; Jha, P. K.; Jain, A.; Yusuf, S. M.; Joy, P. A.; Ballav, N. Metamagnetism in Nanosheets of Co II -MOF with T N at 26 K and a Giant Hysteretic Effect at 5 K. *Inorg. Chem.* **2018**, *57*, 15044–15047.

(6)   Ashafaq, M.; Khalid, M.; Raizada, M.; Ali, A.; Faizan, M.; Shahid, M.; Ahmad, M.; Butcher, R. J. Crystal Engineering and Magnetostructural Properties of Newly Designed Azide/Acetate-Bridged Mn 12 Coordination Polymers. *Cryst. Growth Des.* **2019**, *19*, 2366–2379.

(7)   Wang, Y. Q.; Jia, Q. X.; Wang, K.; Cheng, A. L.; Gao, E. Q. Diverse Manganese(II) Coordination Polymers with Mixed Azide and Zwitterionic Dicarboxylate Ligands: Structure and Magnetic Properties. *Inorg. Chem.* **2010**, *49*, 1551–1560.

(8)   Gao, E. Q.; Cheng, A. L.; Xu, Y. X.; He, M. Y.; Yan, C. H. From Low-Dimensional Manganese(II) Azido Motifs to Higher-Dimensional Materials:

Structure and Magnetic Properties. *Inorg. Chem.* **2005**, *44*, 8822–8835.

(9) Wang, Z.; Cohen, S. M. Postsynthetic Modification of Metal–Organic Frameworks. *Chem. Soc. Rev.* **2009**, *38*, 1315–1329.

(10) Yin, Z.; Wan, S.; Yang, J.; Kurmoo, M.; Zeng, M.-H. Recent Advances in Post-Synthetic Modification of Metal–Organic Frameworks: New Types and Tandem Reactions. *Coord. Chem. Rev.* **2019**, *378*, 500–512.

(11) McKellar, S. C.; Graham, A. J.; Allan, D. R.; Mohideen, M. I. H.; Morris, R. E.; Moggach, S. A. The Effect of Pressure on the Post-Synthetic Modification of a Nanoporous Metal–Organic Framework. *Nanoscale* **2014**, *6*, 4163–4173.

(12) Ennis, C.; Auchettl, R.; Ruzi, M.; Robertson, E. G. Infrared Characterisation of Acetonitrile and Propionitrile Aerosols under Titan's Atmospheric Conditions. *Phys. Chem. Chem. Phys.* **2017**, *19*, 2915–2925.

(13) Salunkhe, R. R.; Kaneti, Y. V.; Yamauchi, Y. Metal-Organic Framework-Derived Nanoporous Metal Oxides toward Supercapacitor Applications: Progress and Prospects. *ACS Nano* **2017**, *11*, 5293–5308.

(14) Zheng, F.; Xu, S.; Yin, Z.; Zhang, Y.; Lu, L. Facile Synthesis of MOF-Derived Mn2O3 Hollow Microspheres as Anode Materials for Lithium-Ion Batteries. *RSC Adv.* **2016**, *6*, 93532–93538.

(15) Li, Y.; Xu, Y.; Yang, W.; Shen, W.; Xue, H.; Pang, H. MOF-Derived Metal Oxide Composites for Advanced Electrochemical Energy Storage. *Small* **2018**, *14*, 1704435.

(16) Wu, H. Bin; Lou, X. W. Metal-Organic Frameworks and Their Derived Materials for Electrochemical Energy Storage and Conversion: Promises and Challenges. *Sci. Adv.* **2017**, *3*, 1–17.

(17) Ashoka, S.; Chithaiah, P.; Tharamani, C. N.; Chandrappa, G. T. Synthesis and Characterisation of Microstructural α-Mn 2 O 3 Materials. *J. Exp. Nanosci.* **2010**, *5*, 285–293.

(18) Maiti, S.; Pramanik, A.; Mahanty, S. Electrochemical Energy Storage in Mn2O3 Porous Nanobars Derived from Morphology-Conserved Transformation of Benzenetricarboxylate-Bridged Metal-Organic Framework. *CrystEngComm*

2016, *18*, 450–461.

(19)   Wang, W.; Geng, J.; Kuai, L.; Li, M.; Geng, B. Porous Mn 2 O 3 : A Low-Cost Electrocatalyst for Oxygen Reduction Reaction in Alkaline Media with Comparable Activity to Pt/C. *Chem. - A Eur. J.* **2016**, *22*, 9909–9913.

(20)   Hazarika, K. K.; Goswami, C.; Saikia, H.; Borah, B. J.; Bharali, P. Cubic Mn 2 O 3 Nanoparticles on Carbon as Bifunctional Electrocatalyst for Oxygen Reduction and Oxygen Evolution Reactions. *Mol. Catal.* **2018**, *451*, 153–160.

(21)   Jahan, M.; Tominaka, S.; Henzie, J. Phase Pure α-Mn 2 O 3 Prisms and Their Bifunctional Electrocatalytic Activity in Oxygen Evolution and Reduction Reactions. *Dalt. Trans.* **2016**, *45*, 18494–18501.

(22)   Liu, R.; Wu, D.; Feng, X.; Müllen, K. Nitrogen-Doped Ordered Mesoporous Graphitic Arrays with High Electrocatalytic Activity for Oxygen Reduction. *Angew. Chemie* **2010**, *122*, 2619–2623.

(23)   Jahan, M.; Bao, Q.; Loh, K. P. Electrocatalytically Active Graphene–Porphyrin MOF Composite for Oxygen Reduction Reaction. *J. Am. Chem. Soc.* **2012**, *134*, 6707–6713.

(24)   Hazarika, K. K.; Goswami, C.; Saikia, H.; Borah, B. J.; Bharali, P. Cubic Mn 2 O 3 Nanoparticles on Carbon as Bifunctional Electrocatalyst for Oxygen Reduction and Oxygen Evolution Reactions. *Mol. Catal.* **2018**, *451*, 153–160.

(25)   Wang, W.; Geng, J.; Kuai, L.; Li, M.; Geng, B. Porous Mn 2 O 3 : A Low-Cost Electrocatalyst for Oxygen Reduction Reaction in Alkaline Media with Comparable Activity to Pt / C. *Chem. Eur.J.* **2016**, *22*, 9909 –9913.

APPENDIX-I

List of Publication(s)

✓ **Publication Related to This Thesis:**

   1. "Mn(II)- Coordination Polymer Derived α-Mn_2O_3 For Oxygen Reduction Processes"

   "*Manuscript to be communicated*"

✓ **Publication(s) in Other Areas:**

   1. "Capacitive and Sensing Responses of Biomass Derived Silver Decorated Graphene, *Scientific Reports* **2019**, *9,* 19725"

   2. "The Switchable Catalytic Property of Metal Organic Framework: Towards Multimodal Catalysis"

   "*Manuscript to be communicated*"

APPENDIX-II

List of Mn-based CPs

Sl. No.	Coordination Polymer	Ligan(s) used	Reference
1	[{Mn(Him)$_4$(H$_2$O)$_2$}{Mn(BTEC)(Him)$_2$(H$_2$O)$_2$}.4H$_2$O]$_n$	1,2,4,5-benzenetetracarboxylate (BTEC); Imidazole (Him)	*Inorg. Chim. Acta* **2003**, *351*, 242-250
2	[{2-MeH$_2$im}$_2${Mn(BTEC)(H$_2$O)$_4$}.5H$_2$O]$_n$	1,2,4,5-benzenetetracarboxylate (BTEC); 2-methylimidazolium (2-MeH$_2$im)	*Inorg. Chim. Acta* **2003**, *351*, 242-250
3	[{Mn(4-MeHim)$_6$}-{Mn(BTEC)(H$_2$O)$_4$}.H$_2$O]$_n$	1,2,4,5-benzenetetracarboxylate (BTEC); 4-methylimidazole (4-MeHim)	*Inorg. Chim. Acta* **2003**, *351*, 242-250
4	[{Mn$_2$(BTEC)(HBzim)$_4$(H$_2$O)$_6$}.2H$_2$O]$_n$	1,2,4,5-benzenetetracarboxylate (BTEC); Benzimidazole (Hbzim)	*Inorg. Chim. Acta* **2003**, *351*, 242-250
5	[{Mn(NCS)$_2$(2,5-dmpdo)$_{1.5}$(H$_2$O)$_2$}.0.5(2,5-dmpdo).H$_2$O]$_n$	2,5-dimethylpyrazine-dioxide (2,5-dmpdo)	*Crys. Grow. & Des.* **2005**, *5*, 269-277
6	[Mn(N$_3$)$_2$(2,5-dmpdo)(H$_2$O)$_2$]$_n$	2,5-dimethylpyrazine-dioxide (2,5-dmpdo)	*Crys. Grow. & Des.* **2005**, *5*, 269-277
7	[Mn(dca)$_2$(2,5-dmpdo)]$_n$	2,5-dimethylpyrazine-dioxide (2,5-dmpdo)	*Crys. Grow. & Des.* **2005**, *5*, 269-277
8	[{Mn(dca)$_2$(2,3-dmpdo)}.H$_2$O]$_n$	2,3-dimethylpyrazine-dioxide (2,3-dmpdo)	*Crys. Grow. & Des.* **2005**, *5*, 269-277
9	[Mn$_3$(BDC)$_3$(DEF)$_2$]$_n$	1,4-benzenedicarboxylic acid (H$_2$BDC)	*J. Am. Chem. Soc.* **2005**, *127*, 1504-1518
10	[Mn(N$_3$)$_2$(btr)$_2$]$_n$	4,4′-bi-1,2,4-triazole (btr)	*Chem. Mater.* **2005**, *17*, 6369-6380
11	[Mn(N$_3$)$_2$-(bte)]n	1,2-bis(1,2,4-triazol-1-yl)ethane (bte)	*Eur. J. Inorg. Chem.* **2005**, 3277–3286
12	[Mn(N$_3$)$_2$(bim)]n	1,2-bis(imidazol-1-yl)ethane (bim)	*Eur. J. Inorg. Chem.* **2005**, 3277–3286
13	[Mn(N$_3$)$_2$(bpee)]n	trans-1,2-bis(4-pyridyl)ethylene (bpee)	*Inorg. Chem.* **2005**, *44*, 1786−1793

14	[{Mn(N$_3$)(dpyo)Cl-(H$_2$O)$_2$}(H$_2$O)]$_n$	4,4′-dipyridyl N,N′-dioxide (dpyo)	*Inorg. Chem.* **2005,** *44,* 1786−1793
15	[{Mn(L1)(N$_3$)$_2$}$_n$.nH$_2$O]$_n$	---	*Inorg. Chem.* **2005,** *44,* 8822−8835
16	[Mn(L$_2$)(N$_3$)$_2$]$_n$	---	*Inorg. Chem.* **2005,** *44,* 8822−8835
17	[Mn(L$_3$)(N$_3$)$_2$]$_n$	---	*Inorg. Chem.* **2005,** *44,* 8822−8835
18	[Mn(N$_3$)$_2$(L$_4$)(CH$_3$OH)]$_n$	---	*Inorg. Chem.* **2005,** *44,* 8822−8835
19	[Mn{(R,S)-BDCD}(H$_2$O)]$_n$	Rac-(R,S)-2,2′-bipyridine-3,3′-dicarboxylic acid 1,1′-dioxide [(R,S)-H2BDCD]	*Crys. Grow. & Des.* **2006**, *6,*11-13
20	[Mn(NDC)(DEF)]$_n$	2,6-naphthalenedicarboxylic acid (H$_2$NDC)	*Inorg. Chem.* **2006**, *45,* 8672−8676
21	[Mn^{III}(L)(μ1,3-N$_3$)]$_n$	L= 5-Fsalen {salen = N,N′-bis(salicylidene)-1,2-diaminoethane)}	*Inorg. Chem.* **2007,** *46,* 11235−11242
22	[Mn^{III}(salophen)(N$_3$)]$_n$	salophen) N,N′-bis(salicylidene)-ophenylenediamine	*Inorg. Chem.* **2007,** *46,* 11235−11242
23	[Mn$_3${(Mn$_4$Cl)$_3$(BTT)$_8$(CH$_3$OH)$_{10}$}$_2$]$_n$	1,3,5-benzenetristetrazol-5-yl (H$_3$BTT)	*J. Am. Chem. Soc.* **2008**, *130,* 5854–5855
24	[(RbI)$_{0.43}$(Mn^{II}){(Fe^{III})(CN)$_6$}$_{0.81}$·3H$_2$O]$_n$	----	*J. Am. Chem. Soc.* **2008**, *130,* 12639–12641
25	[{Mn$_4$O(O$_2$CMe)$_8$(py)}2MeCN]$_n$	Pyridine (py)	*Inorg. Chim. Act.* **2008**, *361,* 4100–4106
26	[{Mn$_3$O(O$_2$CPh)$_7$(4,4'-bpy)}$_3$H$_2$O]$_n$	4,4'-bipyridine (4,4'-bpy)	*Inorg. Chim. Act.* **2008**, *361,* 4100–4106
27	[{(Mn^{III})$_3$O(Brppz)$_3$-(MeOH)$_3$(N$_3$)}.2MeOH]$_n$	3-(5-bromo-2-phenolate)-pyrazolate (Brppz)	*Chem. Commun.,* **2008**, 368–370
28	[{Mn(BDC-Cl$_4$)(py)$_2$(H$_2$O)$_2$}(py)$_2$]$_n$	2,3,5,6-tetrachloro-1,4-benzenedicarboxylic acid (H$_2$BDC-Cl$_4$); Pyridine (py)	*Crys. Grow. & Des.* **2008**, 8, 3437–3445
29	[{Mn(BDCCl$_4$)(MeOH)$_3$}(MeOH)]$_n$	2,3,5,6-tetrachloro-1,4-benzenedicarboxylic acid (H$_2$BDC-Cl$_4$); Pyridine (py)	*Crys. Grow. & Des.* **2008**, 8, 3437–3445
30	[{Mn(BDC-Cl$_4$)(dioxane)(H$_2$O)$_2$](dioxane)]$_n$	2,3,5,6-tetrachloro-1,4-benzenedicarboxylic acid (H$_2$BDC-Cl$_4$)	*Crys. Grow. & Des.* **2008**, 8, 3437–3445
31	[Mn$_5$(BDC-Cl$_4$)$_5$(DMF)$_5$]$_n$	2,3,5,6-tetrachloro-1,4-benzenedicarboxylic acid (H$_2$BDC-Cl$_4$)	*Crys. Grow. & Des.* **2008**, 8, 3437–3445

32	[Mn(L)(MeOH)(H$_2$O)]$_n$	1-(2-hydroxybenzamido)-2-((2-hydroxy-3-methoxybenzylidene)amino)ethane (H$_3$L)	*Crys. Grow. & Des.* **2008**, *8*, 3908–3910
33	[Mn(L)(H$_2$O)]$_n$	1-(2-hydroxybenzamido)-2-((2-hydroxy-3-methoxybenzylidene)amino)ethane (H$_3$L)	*Crys. Grow. & Des.* **2008**, *8*, 3908–3910
34	[Mn$_{17}$(l4-J)$_8$(N$_3$)$_5$(O$_2$CMe)$_4$(pd)$_{10}$(py)$_6$]$_n$	1,3-propanediol (pdH$_2$)	*Poly.* **2009**, *28*, 1814–1817
35	[Mn$_{17}$(l4-J)$_8$(N$_3$)$_5$(O$_2$CMe)$_4$(mpd)$_{10}$(py)$_8$]$_n$	2-methyl-1,3-propanediol (mpdH$_2$)	*Poly.* **2009**, *28*, 1814–1817
36	[{(CH$_3$)$_2$NH$_2$}M(HCOO)$_3$]$_n$	-----	*J. Am. Chem. Soc.* **2009**, *131*, 13625–13627
37	{[Ru(salen)(CN)$_2$]{M$_n$(L)}]$_n$	L= N,N′-(1-methylethylene)bis(2-hydroxynaphthalene-1-carbaldehydeneiminate) dianion	*Inorg. Chem.* **2009**, *48*, 816-818
38	[Mn(bdpbp)$_2$(NO$_3$)$_2$]$_n$	4,4'-bis(dimethoxyphosphorylmethyl)biphenyl (bdpbp)	*Chin. J. Chem.* **2009**, *27*, 1195—1198
39	[Mn$_3$(atpa)$_3$(dmf)$_2$]$_n$	2-aminoterephthalic acid (H$_2$atpa)	*Eur. J. Inorg. Chem.* **2010**, 3804–3812
40	[Mn$_2$(tpa)$_2$(dmf)2]$_n$	Terephthalic acid (H$_2$tpa)	*Eur. J. Inorg. Chem.* **2010**, 3804–3812
41	[Mn$_3$(atpa)$_2$(Hatpa)$_2$]$_n$	2-aminoterephthalic acid (H$_2$atpa)	*Eur. J. Inorg. Chem.* **2010**, 3804–3812
42	[Mn$_3$(tpa)$_3$-(def)$_2$]$_n$	Terephthalic acid (H$_2$tpa)	*Eur. J. Inorg. Chem.* **2010**, 3804–3812
43	[{Mn(sdba)(phen)$_2$(H$_2$O)}$_n$3nH$_2$O]$_n$	4,4'-dicarboxybiphenyl sulfone (H$_2$sdba); 1,10-phenanthroline (phen)	*Inorg. Chim. Acta* **2010**, *363*, 3291–3301
44	[Mn$_2$(sdba)$_2$(lH$_2$O)(py)$_4$]$_n$	4,4'-dicarboxybiphenyl sulfone (H$_2$sdba); 2,2'-bipyridine (2,2'-bpy)	*Inorg. Chim. Acta* **2010**, *363*, 3291–3301
45	[Mn$_3$(sdba)$_2$(Hsdba)$_2$(2,2'-bipy)$_2$]$_n$	4,4'-dicarboxybiphenyl sulfone (H$_2$sdba);	*Inorg. Chim. Acta* **2010**, *363*, 3291–3301
46	[{Mn$_4$(sdba)$_4$(4-mepy)$_2$(H$_2$O)$_4$}$_n$2nH$_2$O]$_n$	4,4'-dicarboxybiphenyl sulfone (H$_2$sdba); 4-picoline (4-mepy)	*Inorg. Chim. Acta* **2010**, *363*, 3291–3301

47	[{Mn$_4$(sdba)$_4$(bpp)$_4$(l-H2O)2}$_n$0.5nH$_2$O]$_n$	4,4'-dicarboxybiphenyl sulfone (H$_2$sdba); 1,3-bi(pyridine-4-yl)propane (bpp)	*Inorg. Chim. Acta* **2010**, *363*, 3291–3301
48	[{Mn$_4$(BT)$_2$(BPP)$_6$(H$_2$O)$_6$}4H$_2$O]$_n$	1,2,4,5-benzenetetracarboxylic acid (H$_4$BT); 1,3-bis(4-pyridyl) propane (BPP)	*Polyhedron* **2010**, *29*, 3125–3131
49	[{Mn$_6$O$_2$(O$_2$CMe)$_{10}$(H$_2$O)$_4$}·2.5H$_2$O]$_n$	----	*Bioin. Chem. App.* **2010**, *2010*, 1-7
50	[Mn$_3$(dctrz)$_2$(H$_2$O)$_8$]$_n$	1-H-1,2,4-triazole-3,5-dicarboxylic acid (H$_3$dctrz)	*Dalton Trans.*, **2010**, *39*, 5877–5884
51	[{Mn$_{15}$(atz)$_{18}$(μ3-OH)$_4$(μ3-SO$_4$)$_4$}$_n$.9nH$_2$O]$_n$	5-aminotetrazolate (atz)	*Crys. Grow. & Des.* **2010**, *10*, 3429–3435
52	[{Mn$_8$(atz)$_4$(μ-OH)$_4$-(μ4-SO$_4$)$_4$(H$_2$O)$_4$}$_n$.nH$_2$O]$_n$	5-aminotetrazolate (atz)	*Crys. Grow. & Des.* **2010**, *10*, 3429–3435
53	[{(CH$_3$)$_2$NH$_2$][Mn$_3$(BTC)(HCOO)$_4$(H$_2$O)}H$_2$O]$_n$	1,3,5-benzenetricarboxylic acid (H$_3$BTC)	*Inorg. Chim. Acta* **2010**, *363*, 645–652
54	[Mn(Bript)(2,2'-bipy)]$_n$	4-bromoisophthalic acid (H$_2$Bript); 2,2'-bipyridine (2,2'-bpy)	*Syn. React. Inor., Met.-Org. Nano-Metal Chem.* **2010**, *40*, 855-860
55	[{Mn(Bript)(phen)(H$_2$O)}(H$_2$O)]$_n$	4-bromoisophthalic acid (H$_2$Bript); 1,10-phenanthroline (phen)	*Syn. React. Inor., Met.-Org. Nano-Metal Chem.* **2010**, *40*, 855-860
56	[{Mn(L)(N$_3$)}ClO$_4$ 3 0.5H$_2$O]$_n$	L= 1,3-bis(4-carboxylato-1-pyridinium)propane	*Inorg. Chem.* **2010**, *49*, 1551–1560
57	[{Mn$_2$(L)$_2$(N$_3$)$_2$}{Mn(N$_3$)4(H$_2$O)$_2$} 3 2H$_2$O]$_n$	L= 1,3-bis(4-carboxylato-1-pyridinium)propane	*Inorg. Chem.* **2010**, *49*, 1551–1560
58	[{Mn$_2$(L)$_2$(N$_3$)$_2$(H$_2$O)2}Br(N$_3$) 3 2H$_2$O]$_n$	L= 1,3-bis(4-carboxylato-1-pyridinium)propane	*Inorg. Chem.* **2010**, *49*, 1551–1560
59	[Mn$_4$ (L)$_2$(N$_3$)$_8$]$_n$	L= 1,3-bis(4-carboxylato-1-pyridinium)propane	*Inorg. Chem.* **2010**, *49*, 1551–1560
60	[MnTHPP.H$_2$O.(DMF)$_2$]$_n$	5,10,15,20-tetra(4-hydroxyphenyl) porphyrin	*Sol. Stat. Scien.* **2010**, *12*, 1242-1247
61	[Mn$_5$(btac)$_4$(μ3-OH)$_2$(EtOH)$_2$·DMF·3 EtOH·3H$_2$O]$_n$	Benzotriazole-5-carboxylate (btac)	*Inorg. Chem.* **2012**, *51*, 674−679
62	[Mn$_2$(tfBDC)$_2$(DMF)$_2$(EtOH)]$_n$	Tetrafluoroterephthalate (tfBDC$_2$)	*Cryst. Growth Des.* **2011**, *11*, 5053–5063
63	[{Me$_4$N}$_3${Mn(L)}{Nb$_6$Cl12(CN)$_6$}}$_3$MeCNH$_2$O]$_n$	L = acacen^{2-} = N,N'-bis(acetylacetone)-1,2-ethylenediimine	*J. Chem. Cryst.* **2011**, *41*, 73–76

64	[{Mn$_2$(4,4-opybz)$_2$(N$_3$)$_2$(H$_2$O)$_2$}·H$_2$O]$_n$	4-(4-pyridyl)benzoic acid N-oxide (4,4-Hopybz)	*Dalton Trans.* **2012**, *41*, 2026–2033
65	[{Mn$_4$(4,4-opybz)$_5$(N$_3$)(H$_2$O)$_8$}(N$_3$)$_2$·2H$_2$O]$_n$	4-(4-pyridyl)benzoic acid N-oxide (4,4-Hopybz)	*Dalton Trans.* **2012**, *41*, 2026–2033
66	[Mn$_2$(tbip)$_2$(bix)]$_n$	5-tert-butyl isophthalic acid (H2tbip); 1,4-bis(imidazol-1-ylmethyl)benzene (bix)	*Inorg. Chem.* **2012**, *51*, 9431−9442
67	[Mn$_3$(tbip)$_3$(bix)$_2$]$_n$	5-tert-butyl isophthalic acid (H2tbip); 1,4-bis(imidazol-1-ylmethyl)benzene (bix)	*Inorg. Chem.* **2012**, *51*, 9431−9442
68	[{Mn$_3$(tbip)$_2$-(Htbip)$_2$(bib)$_2$}·4H$_2$O]$_n$	5-tert-butyl isophthalic acid (H$_2$tbip); 1,4-bis(imidazol)butane (bib)	*Inorg. Chem.* **2012**, *51*, 9431−9442
69	[Mn$_4$(tbip)$_4$(bbp)$_2$(H$_2$O)$_2$]$_n$	5-tert-butyl isophthalic acid (H$_2$tbip); 1,3-bis(benzimidazol)propane (bbp)	*Inorg. Chem.* **2012**, *51*, 9431−9442
70	[{Mn$_4$(tbip)$_4$(bip)}·2H$_2$O]$_n$	5-tert-butyl isophthalic acid (H$_2$tbip); 1,3-bis-(imidazol)propane) (bip)	*Inorg. Chem.* **2012**, *51*, 9431−9442
71	[Mn$_2$(L1)$_{4/3}$(L$_2$)$_2$]$_n$	L1 = 4′-(4-pyridyl)-4,2′:6′,4″-terpyridine; H$_2$L$_2$ = (4-phenyl)-2,6-bis(4-carboxyphenyl)pyridine	*Cryst. Growth Des.* **2012**, *12*, 5426−5431
72	[Mn(H$_2$O)$_2$(O$_2$NC$_9$H$_3$O$_6$)$_2$(C$_{17}$H$_{17}$N$_4$)$_2$]$_n$	5-nitro-1,2,3-benzenecarboxylic acid (h$_3$nbtc)	*Z. Kristallogr. NCS*, **2012**, *227*, 574-576
73	[Mn$_3$(IP)(4,4'-obb)$_3$]$_n$	4,4'-Oxybisbenzoic acid (4,4'-obb), 1H-imidazo[4,5-f][1,10]-phenanthroline (IP)	*Advan. Mater. Res.* **2012**, *528*, 206-209
74	[Mn$_3$(L)(bipy)$_2$]$_n$	hexa[4-(carboxyphenyl)oxamethyl]-3-oxapentane (H6L); 2,2′-bipyridine (bipy)	*Cryst. Eng. Comm.*, **2013**, *15*, 8320-8329
75	[Mn$_3$(L)(dib)]$_n$	hexa[4-(carboxyphenyl)oxamethyl]-3-oxapentane (H6L); 1,4-bis-(1-imidazolyl)benzene (dib)	*Cryst. Eng. Comm.*, **2013**, *15*, 8320-8329
76	[Mn$_3$(L)(dib)(H$_2$O)$_2$]$_n$	hexa[4-(carboxyphenyl)oxamethyl]-3-oxapentane (H$_6$L); 1,4-bis-(1-imidazolyl)benzene (dib)	*Cryst. Eng. Comm.*, **2013**, *15*, 8320-8329
77	[Mn$_6$(L)$_2$(bibp)1.5(H$_2$O)$_5$]$_n$	hexa[4-(carboxyphenyl)oxamethyl]-3-oxapentane (H$_6$L); 4,4′-	*Cryst. Eng. Comm.*, **2013**, *15*, 8320-8329

78	[{Zn$_2$(MnOH–TCPP)-(DPNI)}·0.5DMF·EtOH·5.5H$_2$O]$_n$	bis(1-imidazolyl)biphenyl (bibp) TCPP=tetrakis(4-carboxyphenyl)porphyrin; DPNI=N,N'-di(4-pyridyl)-1,4,5,8-naphthalenetetracarboxydiimide)	*Chem. A Euro. J.* **2013**, *19*, 14316-14321
79	[{MnL$_2$(NCS)$_2$}·(H$_2$O)$_4$]$_n$	L = bis(pyridin-3-ylmethylene)biphenyl-2,2'-dicarbohydrazide	*Z. Naturforsch.*, **2013**, 68, 351–356
80	[{Mn(3-aba)$_2$(4,4-bpy)}$_n$·n(4,4-bpy)]$_n$	3-aminobenzoic acid anion (3-aba−); 4,4'-bipyridine (4,4'-bpy)	*Synth. & React. Inorg. Met-Org. & Nano-Met. Chem.*, **2014**, *44*, 492–497
81	[Mn(pyphen)(L)]$_n$	L = 3-carboxy-1-(4'-(2''-carboxy)biphenylmethyl)-2-oxidopyridinium ; pyrazino[2,3- f][1,10]phenanthroline) (pyphen)	*Z. Naturforsch.* **2013**, *68b*, 155 – 160
82	[C$_{58}$H$_{60}$MnN$_4$O$_8$. C$_{54}$H$_{46}$N$_4$O$_4$. 4 (CH$_4$O)]$_n$	5,15-dimesityl-10,20-bis(4-phenylaceticacid)porphyrin	*Z. Kristallogr.* **2013**, *228*, 335–342
83	[C$_{56}$H$_{50}$MnN$_4$O$_5$. 0.5(C$_{54}$H$_{46}$N$_4$O$_4$). 3.5(C$_2$H$_6$O)]$_n$	5,15-dimesityl-10,20-bis(4-phenylaceticacid)porphyrin	*Z. Kristallogr.* **2013**, *228*, 335–342
84	[Mn(3,5-PDC)(H$_2$O)•(glycol)]$_n$	pyridine-3,5-dicarboxylic acid (3,5-PDC)	*Inorg. Chem. Comm.* **2013**, *38*, 115–118
85	[Mn(dca)$_2$(dmdpy)]$_n$	dicyanamide (dca); 5,5'-dimethyl-2,2'-dipyridine (dmdpy)	*Polyhedron* **2013**, *50*, 16–21
86	[Mn-(tfbdc)(4,4'-bpy)(H$_2$O)$_2$]$_n$	2,3,5,6-tetrafluoroterephthalic acid(H2tfbdc); 4,4'-bipyridine(4,4'-bpy)	*Inorg. Chem.* **2013**, *52*, 2817−2822
87	[{Mn$_3$(btcit)$_2$(H$_2$O)$_2$(DMF)$_2$}.2DMF]$_n$	4,4',4''-[1,3,5-benzenetriyltris(carbonylimino)]trisbenzoic acid (H3btcit); 1,4-bis(imidazol-1-yl)benzene (bib)	*Cryst. Eng. Comm.*, **2013**, *15*, 1613-1617
88	[{Mn$_3$(btcit)$_2$(bib)$_2$}.2DMF]$_n$	4,4',4''-[1,3,5-benzenetriyltris(carbonylimino)]trisbenzoic acid (H3btcit); 1,4-bis(imidazol-1-yl)benzene (bib)	*Cryst. Eng. Comm.*, **2013**, *15*, 1613-1617
89	[{Mn(tmtz)$_{0.5}$(OH-bdc)(H$_2$O)$_2$].2.75H$_2$O]$_n$	1,4-bis(1,2,4-triazol-1-ylmethyl)-2,3,5,6-tetramethylbenzene (tmtz);	*Cryst. Eng. Comm.*, **2013**, *15*, 3630–3639

90	[Mn(tmtz)1.5(1,3-bdc)]$_n$	5-hydroxy-1,3-benzenedicarboxylate (OH-bdc) 1,4-bis(1,2,4-triazol-1-ylmethyl)-2,3,5,6-tetramethylbenzene (tmtz); 1,3-benzenedicarboxylate (1,3-bdc)	*Cryst. Eng. Comm.*, **2013**, *15*, 3630–3639
91	[Mn(tmtz)(1,4-bdc)]$_n$	1,4-bis(1,2,4-triazol-1-ylmethyl)-2,3,5,6-tetramethylbenzene (tmtz); 1,4-benzenedicarboxylate (1,4-bdc)	*Cryst. Eng. Comm.*, **2013**, *15*, 3630–3639
92	[{emi}{Mn(btc)}]$_n$	Benzene-1,3,5-tricarboxylic acid (H3btc); [emi]X (emi = 1-ethyl-3-methylimidazolium; X = Cl−, Br−, I−)	*Cryst. Growth Des.* **2013**, *13*, 1260−1266
93	[{pmi}{Mn(btc)}]$_n$ (Cl/Br)	Benzene-1,3,5-tricarboxylic acid (H3btc); [pmi]X (pmi = 1-propyl-3-methylimidazolium, and X = Cl−, Br−)	*Cryst. Growth Des.* **2013**, *13*, 1260−1266
94	[{pmi}{Mn(btc)}]$_n$ (I)	Benzene-1,3,5-tricarboxylic acid (H3btc); [pmi]X (pmi = 1-propyl-3-methylimidazolium, and X = I−)	*Cryst. Growth Des.* **2013**, *13*, 1260−1266
95	[Mn$_4$(L)$_2$(iB)$_6$]$_n$	2-hydroxy-5-methoxy-3-nitrobenzaldehyde (HL) and isobutyrate (iB−)	*Cryst. Growth Des.* **2013**, *13*, 4138−4144
96	[{Mn(1,2-BDC-F$_4$)(H$_2$O)$_3$}(EtOH)]$_n$	3,4,5,6-tetrafluoro-benzene-1,2-dicarboxylic acid (1,2-H$_2$BDC-F4)	*Z. Naturforsch.* **2013**, *68b*, 277 – 283
97	[Mn(1,2-BDC-F$_4$)(H$_2$O)$_2$(DMF)]$_n$	3,4,5,6-tetrafluoro-benzene-1,2-dicarboxylic acid (1,2-H$_2$BDC-F4)	*Z. Naturforsch.* **2013**, *68b*, 277 – 283
98	[Mn(MeO-m-BDC)(DMF)]$_n$	5-methoxybenzene-1,3-dicarboxylic acid (MeO-m-H$_2$BDC)	*Acta Cryst.* **2013**. *C69*, 1-3
99	[Mn$_2$(Adi)$_2$(DMA)]$_n$	Adipate anion (Adi); N,N′-dimethylacetamide (DMA)	*J. Sol. Stat. Chem.* **2013**, *204*, 197–204
100	[Mn$_2$(Adi)$_2$(DMF)]$_n$	Adipate anion (Adi); N,N′-dimethylformamide(DMF)	*J. Sol. Stat. Chem.* **2013**, *204*, 197–204
101	[Mn$_4$(Adi)$_4$(DMF)$_2$]$_n$	Adipate anion (Adi); N,N′-dimethylformamide(DMF)	*J. Sol. Stat. Chem.* **2013**, *204*, 197–204
102	[MnCl$_2$(BIPS)$_2$·2CH$_3$OH·2H$_2$O]$_n$	Me$_2$Si(p-C$_6$H$_4$-imdazol-1-yl)$_2$ (BIPS)	*App. Mech. Mat.* **2013**, *275-277*, 2367-2370

103	[{Mn$_3$(HCOO)$_6$} DMF]$_n$	Formic Acid; N,N-dimethylformamide (DMF)	*J. Mol. Struc.* **2014**, *1074*, 19–21
104	[{Mn$_2$(dtdn)$_2$(bpp)(H$_2$O)$_3$}·4H$_2$O]$_n$	6,6-dithiodinicotinic acid (H2dtdn); 1,3-bis(4-pyridyl)propane (bpp)	*Synth. & React. Inorg. Met-Org. & Nano-Met. Chem.* **2014**, *44*, 1023–1028
105	[Mn(3,3'-bpdc)]$_n$	3,3'-bipyridine-2,2'dicarboxylate monohydrate (3,30-bpdcH$_2$O)	*Inorg. Chim. Acta.* **2015**, *436*, 214–219
106	[MnL]$_n$	2-hydroxy-N-(2-(((3-hydroxynaphthalen-2-yl)methylene)amino)ethyl) benzamide (H$_3$L)	*Inorg. Chim. Acta* **2015**, *434*, 252-257
107	[Mn$_3$(BOABA)$_2$(phen)$_2$]$_n$	2,4-bis-oxyacetate-benzoic acid (H$_3$BOABA)	*Sci. China Chem.* **2015**, *58*, 448-456
108	[Mn$_2$(BOABA)(OH)]·(H$_2$O)$_2$]$_n$	2,4-bis-oxyacetate-benzoic acid (H$_3$BOABA)	*Sci. China Chem.* **2015**, *58*, 448-456
109	[{(CH$_3$)$_4$N}{Mn$_2$(NCNCN)$_5$}]$_n$	N(CN)$^{2-}$	*Acta Cryst.* **2015**, *C71*, 850–855
110	[{(C$_4$H$_9$)(C$_6$H$_5$)$_3$P}$_2${Mn(NCNCN)$_4$}]$_n$	N(CN)$^{2-}$	*Acta Cryst.* **2015**, *C71*, 850–855
111	[Mn-BTC]$_n$	1,2,4,5-benzenetetracarboxylic acid (BTC)	*RSC Adv.,* **2016**, *6*, 61319–61324
112	[Mn$_{1.7}$Co$_{0.3}$-BTC]$_n$	1,2,4,5-benzenetetracarboxylic acid (BTC)	*RSC Adv.,* **2016**, *6*, 61319–61324
113	[{Mn(L)(pyz)}ClO$_4$2(H$_2$O)]$_n$	Schiff Base HL (4-aminoantipyrine+salicylaldehyde); Pyrazine (pyz)	*Inorg. Chim. Acta* **2016**, *443*, 224–229
114	[{Mn(azbpy)$_2$(NO$_2$-bdc)}$_2$]$_n$	4,4′-azobispyridine (azbpy); 5-nitro-1,3-benzenedicarboxylate (NO$_2$-bdc$_2$−)	*Cryst. Growth Des.* **2016**, *16*, 4793−4804
115	[Mn$_3$(BTTB)$_2$(H$_2$O)$_4$](H$_2$O)$_2$]$_n$	4,4,4-(benzene-1,3,5-triyl-tris(oxy))tribenzoic acid (H$_3$BTTB)	*Z. Anorg. Allg. Chem.* **2016**, *642*, 778–784
116	[Mn$_3$(BTTB)$_2$(DMF)$_2$](DMF)$_2$]$_n$	4,4,4-(benzene-1,3,5-triyl-tris(oxy))tribenzoic acid (H$_3$BTTB)	*Z. Anorg. Allg. Chem.* **2016**, *642*, 778–784
117	[{C$_6$H$_4$(O)CHN(CH$_2$)$_2$NCH(O)C$_6$H$_4$}Mn(N$_3$)]$_n$	C$_6$H$_4$(OH)CH=N-CH$_2$CH$_2$-N=CH(OH)C$_6$H$_4$ (H$_2$L)	*Polyhedron* **2017**, *127,* 315-322
118	[Mn(SO$_4$)(C$_{18}$H$_{18}$N$_6$)(C$_2$H$_6$O$_2$)]$_n$	1,3,5-tris[(1H-imidazol-1-yl)methyl]benzene	*Acta Cryst.* **2016**, *C72*, 895–900
119	[Mn$_3$(NDC)$_3$(DMA)$_4$]$_n$	2,6 napthalenedicarboxylic acid (NDC), N, N-dimethylacetamide (DMA)	*RSC Adv.* **2016**, *6*, 86468-86476

120	[{Mn(L)(H$_2$O)$_2$}·2Nap]$_n$	1,2-bis(4-pyridyl)ethylene (L); Naproxen (Nap)	*Chem. Eur. J.* **2016**, *22*, 988 – 998
121	[{Mn(L)(Ibu)$_2$(H$_2$O)$_2$}]$_n$	1,2-bis(4-pyridyl)ethylene (L); Ibuprofen (ibu)	*Chem. Eur. J.* **2016**, *22*, 988 – 998
122	[{Mn(L)(Flr)$_2$(H$_2$O)$_2$}]$_n$	1,2-bis(4-pyridyl)ethylene (L); Flurbiprofen (Flr)	*Chem. Eur. J.* **2016**, *22*, 988 – 998
123	[{Mn(L)(Ind)$_2$(H$_2$O)$_2$}·H$_2$O]$_n$	1,2-bis(4-pyridyl)ethylene (L); Indometacin (ind)	*Chem. Eur. J.* **2016**, *22*, 988 – 998
124	[{Mn$_2$(L)$_2$(m-Flu)$_4$(H$_2$O)}·L]$_n$	1,2-bis(4-pyridyl)ethylene (L); Flufenamic acid (flu)	*Chem. Eur. J.* **2016**, *22*, 988 – 998
125	[{Mn$_2$(L)$_2$(mTol)$_4$(H$_2$O)$_2$}]$_n$	1,2-bis(4-pyridyl)ethylene (L); Tolfenamic acid (tol)	*Chem. Eur. J.* **2016**, *22*, 988 – 998
126	[{Mn$_2$(L)$_2$(m-Mef)$_4$(H$_2$O)$_2$}]$_n$	1,2-bis(4-pyridyl)ethylene (L); Mefenamic acid (mef)	*Chem. Eur. J.* **2016**, *22*, 988 – 998
127	[Mn^{III}(F$_5$CPp)–Mn^{II}]$_n$	5-(pentafluorophenyl)-10,15,20-tri(4-carboxyphenyl)porphyrin dianion (F5CPp)	*Catal. Lett.* **2016**, *146*, 1087–1098
128	[Mn^{III}(F$_5$CPp)–Co^{II}]$_n$	5-(pentafluorophenyl)-10,15,20-tri(4-carboxyphenyl)porphyrin dianion (F5CPp)	*Catal. Lett.* **2016**, *146*, 1087–1098
129	[Mn^{III}(F$_5$CPp)–Ni^{II}]$_n$	5-(pentafluorophenyl)-10,15,20-tri(4-carboxyphenyl)porphyrin dianion (F5CPp)	*Catal. Lett.* **2016**, *146*, 1087–1098
130	[Mn^{III}(F$_{10}$CPp)–Mn^{II}]$_n$	5,15-bis(pentafluorophenyl)-10,20-bis(4-carboxyphenyl)porphyrin dianion (F10CPp)	*Catal. Lett.* **2016**, *146*, 1087–1098
131	[Mn^{III}(F$_{10}$CPp)–Co$_{II}$]$_n$	5,15-bis(pentafluorophenyl)-10,20-bis(4-carboxyphenyl)porphyrin dianion (F10CPp)	*Catal. Lett.* **2016**, *146*, 1087–1098
132	[Mn^{III}(F$_{10}$CPp)–Ni^{II}]$_n$	5,15-bis(pentafluorophenyl)-10,20-bis(4-carboxyphenyl)porphyrin dianion (F10CPp)	*Catal. Lett.* **2016**, *146*, 1087–1098
133	[{(CH$_3$)$_2$NH$_2$}$_3${Mn$_5$(btc)$_4$(Ac)(H$_2$O)$_4$}·5H$_2$O]$_n$	1,3,5-benzenetricarboxylic acid (H$_3$btc); Acetic acid (Hac)	*J. Coord. Chem.* **2016**, *69*, 11-13, 1792-1801
134	[Mn(N$_3$)(tzbp)]$_n$	1H-tetrazol-5-yl)-2,2′-bipyridine (Htzbp)	*Dalton Trans.,* **2016**, *45*, 3388-3397
135	[{Mn$_2$L(1,1'-phen)$_2$}DMF 0.5H$_2$O]$_n$	Bis-(3,5-dicarboxyphenyl) terephthalamide (H4L)	*Polyhedron* **2016**, *105*, 49–55

136	[Mn(1,1'-phen)(SO$_4$)(H$_2$O)$_2$]$_n$	1,10-phen	*Polyhedron* **2016**, *105*, 49–55
137	[{Mn(L)}{Ni(CN)$_4$}.2H$_2$O]$_n$	L = 2,6-bis[1-(2-(N-methylamino)ethylimino)ethyl]pyridine; K$_2$[Ni(CN)$_4$]	*Acta Chim. Slov.* **2017**, *64*, 215–220
138	[Mn(L)][Pd(CN)$_4$]$_n$	L = 2,6-bis[1-(2-(N-methylamino)ethylimino)ethyl]pyridine; K$_2$[Pd(CN)$_4$]	*Acta Chim. Slov.* **2017**, *64*, 215–220
139	[Mn(L)][Pt(CN)$_4$]$_n$	L = 2,6-bis[1-(2-(N-methylamino)ethylimino)ethyl]pyridine; K2[Pt(CN)$_4$]	*Acta Chim. Slov.* **2017**, *64*, 215–220
140	[{Mn$_3$(pzbtz)$_2$(Cl)$_2$(H$_2$O)$_2$}·4H$_2$O]$_n$	5'-(pyrazin-2-yl)-2H,4'H-3,3'-bi(1,2,4-triazole) (H$_2$pzbtz),	*Inorg. Chem.* **2017**, *56*, 10090−10098
141	[{Mn$_2$(pzbtz)(SO$_4$)(H$_2$O)$_3$}·3H$_2$O]$_n$	5'-(pyrazin-2-yl)-2H,4'H-3,3'-bi(1,2,4-triazole) (H$_2$pzbtz),	*Inorg. Chem.* **2017**, *56*, 10090−10098
142	[{Mn$_3$(pzbtz)$_3$(H$_2$O)$_3$}·1.5DMA·2H$_2$O]$_n$	5'-(pyrazin-2-yl)-2H,4'H-3,3'-bi(1,2,4-triazole) (H$_2$pzbtz),	*Inorg. Chem.* **2017**, *56*, 10090−10098
143	[Mn$_2$(μ-L$_1$)$_2$(μ-N$_3$)$_2$]$_n$	2-acetylpyridine isonicotinoylhydrazone (HL1)	*J. Coord. Chem.* **2017**, *70*, 12, 1973–1983
144	[Mn(μ-HL$_2$)(SCN)$_2$]$_n$	2-acetylpyridinenicotinoylhydrazone (HL2)	*J. Coord. Chem.* **2017**, *70*, 12, 1973–1983
145	([Mn(tfbdc)(4,4'-bpy)(H$_2$O)$_2$]$_n$	2,3,5,6-tetrafluoroterephthalic acid (H2tfbdc); 4,4'-bipyridine (4,4'-bpy)	*RSC Adv.*, **2017**, *7*, 29611–29617
146	[Mn$_5$(H$_2$L)·16H$_2$O]$_n$	Phytate (L12−)	*ChemPlusChem*, **2017**, *82*, 721-731
147	[(H$_2$terpy)$_2$[Mn(H$_6$L)(terpy)(H$_2$O)]·17H$_2$O]$_n$	Phytate (L12−); Terpyridine (terpy)	*ChemPlusChem*, **2017**, *82*, 721-731
148	[{Mn^{II}(NO$_3$)$_2$(OH$_2$)$_2$(azopy)$_2$}·2MeCN]$_n$	4,4′-azobisIJpyridine (azopy)	*CrystEngComm*, **2017**, *19*, 994–1000
149	[poly-{MnII(azopy)$_2$(CNAgCN)4}]$_n$	4,4′-azobisIJpyridine (azopy)	*CrystEngComm*, **2017**, *19*, 994–1000
150	[poly-[{Mn^{II}$_2$(pda)(Hpda)$_2$(azopy)$_2$(OH$_2$)$_2$}·2MeCN]$_n$	4,4′-azobisIJpyridine (azopy); 1,4-phenylenediacetic acid (pdaH$_2$)	*CrystEngComm*, **2017**, *19*, 994–1000
151	[Mn$_3$(L)$_2$(OH)$_2$]$_n$	2-carboxyethylIJphenyl)phosphinic acid (H$_2$L)	*CrystEngComm*, **2017**, *19*, 1052–1057
152	[Mn$_3$(MA)(H$_2$O)$_2$(ipa)$_3$]$_n$	Isophthalic acid (ipa); Melamine (MA)	*J. Mater. Sci.* **2018**, *53*, 1346–1355

153	$[\{(Ni^{II}LMn^{II})_2(\mu1,1,3-N_3)_2\}(\mu1,3-N_3)_2]_n$	Schiff base H_2L (3-methoxysalicylaldehyde+1,3-diaminopropane)	*Dalton Trans.*, **2018**,*47*, 836-844
154	$[\{Mn(L-Cl)(DMA)\}(H_2O)]_n$	2,2'-dichloro-4,4'-azodibenzoic acid (H_2L-Cl)	*J. Sol. Stat. Chem.* **2017**, *254*, 9–13
155	$[Mn(L-CH_3)(DMA)]_n$	2,2'-dimethyl-4,4'-azodibenzoic acid (H_2L-CH_3)	*J. Sol. Stat. Chem.* **2017**, *254*, 9–13
156	$[\{Mn(II)(MBAB)(H_2O)_2\}]_n$	Maloyl-bis-2-aminobenzothiazole (MBAB)	*J. Chin. Adv. Mat. Soc.*, **2017**, *5*, 118-132
157	$[\{MnL(DMF)(H_2O)3.33\}]_n$	Benzimidazolone diacetic acid (H_2L)	*R.Soc. open sci.* **2017**, *4*, 171064
158	$[M_3L_2(solvent)_2]_n$	(S or R)-3,3′-di-tert-butyl-5,5′-dicarboxyphenyl-6,6′-dimethylbiphenyl-2,2′-diylhydrogen phosphate (H_3L)	*Nat Commun* **2017**, *8*, 2171 (1-9)
159	$[\{Mn_{1.5}(TCPB)(H_2O)(\mu2–OH_2)\}\cdot H_2O]_n$	1,3,5–tris(4–carbonylphenyloxy)benzene(H_3TCPB)	*Cryst. Growth Des.* **2017**, *17*, 11, 5887-5897
160	$[Mn_{1.5}(TCPB)(bib)_{0.5}(DMF)]_n$	1,3,5–tris(4–carbonylphenyloxy)benzene(H_3TCPB); 1,4–bis(imidazol–1–yl)benzene	*Cryst. Growth Des.* **2017**, *17*, 11, 5887-5897
161	$[\{Mn_2(L)(H_2O)_2\}\cdot H_2O]_n$	pyridine-3,5-dicarbox(3,5-dicarboxylatoanilide) (H_4L)	*Z. Naturforsch.* **2017**, *72*, 937-940
162	$[Mn_6(Ipa)_6(ad)\cdot 6H_2O]_n$	Isophthalate (Ipa); Adenine (ad)	*Appl Organometal Chem.* **2018**, *e4447*, 1-9
163	$[Mn_3(chdc)_3-(NMP)_2(DMF)_2]_n$	Trans-1,4-cyclohexanedicarboxylate (chdc2–), N-methylpyrrolidone (NMP); N,N-dimethylformamide (DMF)	*Russ. Chem. Bull., Int. Ed.* **2018**, *67*, 490—496
164	$[\{Mn(L)(Cl)_2(H_2O)\}\cdot(CH_3)_2CO)]_n$	Dispiro-dipyridyloxy-cyclotriphosphazene (L)	*Polyhedron* **2018**, *146*, 99-107
165	$[\{Mn(H_2L)(NO_3)_2(CH_3OH)\}\cdot CH_3OH]_n$	(E)-3-hydroxy-N'-(1-(2-oxo-2H-chromen-3-yl)ethylidene)-2-naphthohydrazide (H_2L)	*J. Coord. Chem.* **2018**, *71*, 1127–1146
166	$[Mn(HL)(NO_3)(CH_3OH)]_n$	(E)-3-hydroxy-N'-(1-(2-oxo-2H-chromen-3-yl)ethylidene)-2-naphthohydrazide (H_2L)	*J. Coord. Chem.* **2018**, *71*, 1127–1146
167	$[Mn(DMTDC)(DMF)]_n$	3,4-dimethylthieno[2,3-b]thiophene-2,5-dicarboxylic acid (H_2DMTDC)	*Inorg. Chem. Comm.* **2018**, *96*, 124–127

168	$[(C_5H_8N_3)_2\{Mn_2(C_2O_4)_3\}\cdot 3H_2O]_n$	Oxalic Acid; 2,6-diaminopyridine	*J. Chem. Sci.* **2018**, *130*, 1-9
169	$[\{Mn_3(Pfca)_6(Phen)_2\}\cdot 2DMF]_n$	4-fluorocinnamic acid (Hpfca), 1,10-phenanthroline (phen)	*Russ. J. Coord. Chem.* **2018**, *44*, 340–346
170	$[Mn(Pfca)_2(Phen)(H_2O)]_n$	4-fluorocinnamic acid (Hpfca), 1,10-phenanthroline (phen)	*Russ. J. Coord. Chem.* **2018**, *44*, 340–346
171	$[\{Mn_2(TCPP).2H_2O\}.DMF]_n$	5,10,15,20-tetrakis(4-benzoate)porphyrin (TCPP)	*Chem. Euro. J.* **2018**, *24*, 16662-16669
172	$[\{Mn(BPZ)(OH)\}\cdot DMAc]_n$	4,4'-Bipyrazolate (BPZ)	*Dalton Trans.*, **2018**, *47*, 8779-8786
173	$[Mn(TDC)(5,5'-dmbpy)(H_2O)]_n$	Thiophene-2,5-dicarboxylic acid (H2TDC)	*Inorg. Chem. Comm.* **2019**, *99*, 140–144
174	$[Mn(adc)(4-phpy)_2(H_2O)_2]n$	Acetylenedicarboxylic acid (H2adc); 4-phenylpyridine (4-phpy)	*New J. Chem.*, **2019**, *43*, 5167-5172
175	$[Mn_2(l4-dmg)-(l4-dmg)(l-bipy)]_n$	2,2-dimethylglutaric acid (H2dmg); 4,4'-bipyridine (bipy)	*Polyhedron* **2019**, *171*, 317–322
176	$[Mn_2(l4-dmg)(l4-dmg)(l-dpeten)]_n$	2,2-dimethylglutaric acid (H2dmg); 1,2-di(4-pyridyl)ethylene (dpeten)	*Polyhedron* **2019**, *171*, 317–322
177	$[\{Mn_2(Pyala)_2(Dca)_2(H_2O)\}_n\cdot 2H_2O]_n$	N-(2-pyridylmethyl)-L-alanine (Pyala) and Dicyanamide anion (Dca)	*Eur. J. Chem.* **2019**, *10*, 267-272
178	$[\{Mn^{II}_2Mn^{III}_{10}Na_2(\mu6-O)_2(N_3)_{10}(NO_3)(H_2O)_4(thme)_8\}\cdot 3-(Et_3NH)]_n$	1,1,1-tris (hydroxymethyl)ethane (H3thme)	*Cryst. Growth Des.* **2019**, *19*, 2366−2379
179	$[\{Mn^{II}_3Mn^{III}_9Na_7(\mu2-O)_2(\mu6-O)_2(O)_5-(CH_3O)(CH_3CO_2)_{11}(thmp)_8\}\cdot 4(O)]_n$	1,1,1-tris (hydroxymethyl)propane (H3thmp)	*Cryst. Growth Des.* **2019**, *19*, 2366−2379
180	$[MnL]_n$	L = 2-hydroxy-N-[2-[[(2-aminophenyl)methylene]amino]-2-methylpropyl]-benzamide	*Dalton Trans.*, **2019**, *48*, 8617-8622
181	$[\{\{Fe(qxcq)(CN)3\}\{Mn(L_1)(H_2O)\}\}\{Mn(L_1)(H_2O)(CH_3OH)\}(ClO_4)\cdot 1.5MeOH\cdot 0.5H_2O]_n$	L₁ = N,N'-bis(3-methoxy-5-bromosalicylideneiminate	*Polymers* **2019**, *11*, 1-15
182	$[\{\{Fe(qxcq)(CN)_3\}\{Mn(L_2)\}\}_2\cdot 0.5H_2O]_n$	L₂ = N,N'-ethylene-bis(3-ethoxysalicylideneiminate	*Polymers* **2019**, *11*, 1-15
183	$[\{Fe(qxcq)(CN)_3\}\{Mn(L_3)\}]_n$	L3 = bis(acetylacetonato)ethylenediimine	*Polymers* **2019**, *11*, 1-15

184	[{Fe(qxcq)(CN)$_3$}{M$_n$(L$_4$)}·1.5MeOH·0.5CH3CN·0.25H$_2$O]$_n$	L4 = N,N'-(1,1,2,2-tetramethylethylene)bis(salicylideneiminate	*Polymers* **2019**, *11*, 1-15
185	[Mn$_2$Cl$_2$(cptpy)$_2$(phdat)H$_2$O]$_n$	4'-(4-carboxyphenyl)-2,2':6',2''-terpyridine (Hcptpy), 2,4-diamino-6-phenyltriazine (phdat)	*J. Sol. Stat. Chem.* **2019**, *269*, 118–124
186	[Mn(HL)(C$_2$H$_5$OH)]$_n$	2-(5-bromo-pyridin-3-yl)-1H-imidazole-4,5-dicarboxylic acid (H$_3$L)	*J. Coord. Chem.* **2019**, *72*, 1820–1832
187	[MnL]$_n$	1-(2-hydroxy-benzamido)-2-(2-hydroxy-5-nitrobenzylideneamino)-ethane (H$_3$L)	*J. Inorg. Organomet. Polym.* **2019**, *29*, 1995–2002
188	[{Mn$_{1.5}$(H$_3$L)(bibp)$_{0.5}$(H$_2$O)$_2$}·3H$_2$O]$_n$	1,4-bis((4-imidazol-1-yl)benzyl)piperazine (bibp)	*Molecules* **2019**, *24*, 1-12
189	[Mn(H$_2$O)(mal)(5dmb)·H$_2$O]$_n$	maleato (mal); 5,5′-dimethyl-2,2′-bipyridine (5dmb)	*J. Chem. Crystallogr.* **2019**, *49*, 8–20
190	[{Mn(TCPP)0.5(H$_2$O)$_2$}.2H$_2$O]$_n$	5,10,15,20-tetrakis(4-benzoate)porphyrin (TCPP)	*Micro. Meso. Mat.* **2019**, *280*, 372–378
191	[Mn(NDC)(L)(H$_2$O)]$_n$	L= 1,4-bis(5,6-dimethylbenzimidazole)butane; 1,4-naphthalene dicarboxylic acid (1,4-H$_2$NDC)	*J. Sol. Stat. Chem.* **2019**, *273*, 67–74
192	[{Mn$_2$(HBTC)$_2$(L)$_2$(H$_2$O)$_2$}·2H$_2$O]$_n$	L= 1,4-bis(5,6-dimethylbenzimidazole)butane; 1,3,5-benzenetricarboxylic acid (H3btc)	*J. Sol. Stat. Chem.* **2019**, *273*, 67–74
193	[M(adc)(4-spy)$_2$(H$_2$O)$_2$]$_n$	Acetylenedicarboxylic acid (H2adc); 4-styrylpyridine (4-spy)	*J. Chem. Sci.* **2020**, *132*, 1-6

----X----